

DEVELOPMENT OF LASER DESORPTION IONIZATION ON A  
QUADRUPOLE ION TRAP MASS SPECTROMETER

By

RAFAEL ROBERTO VARGAS

A DISSERTATION PRESENTED TO THE GRADUATE SCHOOL  
OF THE UNIVERSITY OF FLORIDA IN PARTIAL FULFILLMENT  
OF THE REQUIREMENTS FOR THE DEGREE OF  
DOCTOR OF PHILOSOPHY

UNIVERSITY OF FLORIDA

1993

To my family

## ACKNOWLEDGEMENTS

I give my sincerest thanks to Professor Richard A. Yost for all the things I learned in and out of the laboratory. He set an example of excellence in research and communication which I will always remember when I pursue my goals. I especially would like to thank Rick for the opportunity to learn and teach in the electronics lab--a valuable experience for all future analytical chemists. Also, I appreciate the opportunities and encouragement he gave me to participate in many scientific meetings.

Thanks go to Dr. Jodie Johnson for many helpful hints and for seeing my best results not only analytically, but with excitement as well. He reminded me that research should be fun during times when I temporarily had forgotten. Thanks go to my committee members, Drs. James Winefordner, Vaneica Young, John Eyler, and Buna Wilder, for performing their duties with the utmost attention. Thanks go to Mike Lee and Ira Rosenberg for participating in my research with helpful suggestions and providing the very important funding from Bristol-Myers Squibb. On the subject of funding, I also extend my appreciation for the NASA joint project that got me started on quadrupole ion traps and gave me the opportunity to learn. Thanks go to the support staff whose skills I used greatly in my years at the

department. In particular I would like to mention Jeanne Karably for quickly preparing my TRs no matter how much I managed to complicate them.

Special thanks go to Nate Yates whose programming and electronics knowledge helped me to interface the laser to the trap, and to Matt Booth for not only setting up ion injection, but also making it work well.

All the friend and family support I have received over the past several years and the assurance that there is another world out there beyond the ivory research lab were given to me by some very good friends, Tony Annacchino, Uli Bernier, Jon Jones, Henry Lin, and Donna Robie. To my very special family and their unabated support, Nancy, Janice, and Steve, I thank them all. Finally, I wish to acknowledge my wonderful parents, whose love and support are beyond measure. Someone once said, "If you want to be successful, then choose your parents carefully." I believe I chose the best.

## TABLE OF CONTENTS

	<u>Page</u>
ACKNOWLEDGEMENTS . . . . .	iii
LIST OF FIGURES . . . . .	viii
ABSTRACT . . . . .	xiv
 CHAPTER	
1 INTRODUCTION . . . . .	1
Project and Goals . . . . .	1
Previous Work . . . . .	2
Purpose of Using the Quadrupole Ion Trap . . . . .	4
Quadrupole Ion Trap Mass Spectrometry . . . . .	7
History . . . . .	7
How the Ion Trap Works . . . . .	8
Performing MS/MS on the Ion Trap . . . . .	10
LDI and MALDI Combined with MS . . . . .	11
Matrix-assisted LDI . . . . .	14
How MALDI Works . . . . .	15
Comparison to Other Desorption Methods . . . . .	18
Recent Advances in LDI/Quadrupole Ion Trap MS . . . . .	19
Overview of Dissertation . . . . .	20
 2 INSTRUMENTAL AND EXPERIMENTAL DESCRIPTION . . . . .	 22
Instrumental Description . . . . .	22
Ion Trap Mass Spectrometer . . . . .	22
Ion Trap Theory . . . . .	23
Nitrogen Laser and Interface . . . . .	26
Experimental Setup . . . . .	31
Scan functions and Timing . . . . .	31
Trapping Radiofrequency Phase Synchronization Circuit . . . . .	33

	Sample Preparation . . . . .	38
3	FUNDAMENTAL STUDIES OF LASER DESORPTION IONIZATION/QUADRUPOLE ION TRAP MASS SPECTROMETRY USING AN INTERNAL CONFIGURATION . . . . .	42
	Effect of Radiofrequency Phase Angle on Trapping Efficiency .	43
	Effect of Radiofrequency Amplitude on Trapping Efficiency . .	48
	Effect of Buffer Gas Pressure on Trapping Efficiency . . . . .	55
	Conclusions . . . . .	61
4	LASER DESORPTION IONIZATION/QUADRUPOLE ION TRAP MASS SPECTROMETRY USING AN INTERNAL SOURCE CONFIGURATION . . . . .	66
	Laser Desorption Ionization . . . . .	66
	MS/MS of Trimethylphenylammonium Bromide . . . . .	66
	Positive and Negative Ion Spectra . . . . .	71
	Matrix Compounds . . . . .	73
	Matrix-Assisted Laser Desorption Ionization . . . . .	79
	MALDI of Spiperone . . . . .	83
	MALDI Signal Lifetimes . . . . .	87
	Laser Irradiance . . . . .	89
	Matrix Preparation . . . . .	94
	Lowest Sample Amount . . . . .	97
	MALDI/MS/MS of Spiperone . . . . .	99
	MALDI of Leucine Enkephalin . . . . .	110
	Spiperone in Matrigel . . . . .	114
	LDI of Spiperone in Matrigel . . . . .	115
	MALDI of Spiperone in Matrigel . . . . .	117
	Conclusions . . . . .	122
5	LASER DESORPTION IONIZATION/QUADRUPOLE ION TRAP MASS SPECTROMETRY USING AN EXTERNAL SOURCE CONFIGURATION . . . . .	124
	Laser Beam/Ion Axis Placement . . . . .	126
	Instrumental Description . . . . .	128
	Laser Desorption Ionization . . . . .	132
	Low Mass Cutoff . . . . .	133
	Laser Irradiance . . . . .	137
	MS <sup>3</sup> of Trimethylphenylammonium Bromide . . . . .	137
	Matrix-Assisted Laser Desorption Ionization . . . . .	140

	MALDI of Spiperone .....	142
	MALDI of Spiperone in Matrigel .....	145
	Conclusions .....	150
6	CONCLUSIONS .....	152
	Summary .....	152
	Suggestions for Future Studies .....	155
APPENDICES		
A	ELECTRONIC CIRCUIT CALIBRATION DATA FOR THE TRAPPING RADIOFREQUENCY PHASE ANGLE EXPERIMENT .....	158
B	FORTH KEY SEQUENCE PROGRAMS FOR COMPUTER ASSISTED RECORDING OF RADIOFREQUENCY PHASE ANGLE DATA AND RADIOFREQUENCY AMPLITUDE DATA .....	160
	REFERENCES .....	166
	BIOGRAPHICAL SKETCH .....	170

## LIST OF FIGURES

<u>Figure</u>	<u>Page</u>
1-1. Schematic of quadrupole ion trap mass spectrometer showing which electrodes the various voltages are applied and the configuration of the filament and detector . . . . .	9
1-2. Illustrative comparison of LDI and MALDI sample composition and ionization products . . . . .	16
2-1. Plot of stability diagram defined by iso- $\beta$ lines. Ions which have $a_z$ , $q_z$ coordinates within the bound region have stable trajectories . . . . .	27
2-2. Schematic of laser desorption ionization/quadrupole ion trap mass spectrometer . . . . .	28
2-3. Schematic of laser/quadrupole ion trap showing the introduction of the laser beam and sample probe tip . . . . .	30
2-4. Drawing of rf scan function showing sequence of important events . . .	32
2-5. Diagram of the rf phase synchronization circuit. The variable resistor ( $R_v$ ) is adjusted for different rf phase angle settings during the laser pulse . . . . .	34
2-6. Timing plot for rf phase synchronization experiment. See text for trace descriptions . . . . .	36
2-7. Plot of rf phase angle versus variable resistor position settings used for rf phase angle study . . . . .	37
2-8. Structures and molecular weights of UV absorbing matrix compounds used for MALDI experiments: a) sinapinic acid, b) 2,5-dihydroxybenzoic acid, c) 2,4-dinitroaniline, d) coumarin-120, and e) nicotinic acid . . . . .	39



2-9.	UV absorption spectrum of the matrix compound sinapinic acid. Molar absorptivity at 337 nm is $14391 \text{ M}^{-1} \text{ cm}^{-1}$ . . . . .	40
3-1.	Laser desorption ionization mass spectrum of graphite. Average of 10 scans (1 microscan each scan) . . . . .	46
3-2.	$\text{C}_3^+$ intensity and trapping rf amplitude versus rf phase angle; a) Run 1, b) Run 2. Error bars designate standard error of the mean. Average of 10 scans (1 microscan each scan) . . . . .	47
3-3.	$\text{C}_4^+$ intensity and trapping rf amplitude versus rf phase angle; a) Run 1, b) Run 2. Error bars designate standard error of the mean. Average of 10 scans (1 microscan each scan) . . . . .	48
3-4.	$\text{C}_5^+$ intensity and trapping rf amplitude versus rf phase angle; a) Run 1, b) Run 2. Error bars designate standard error of the mean. Average of 10 scans (1 microscan each scan) . . . . .	49
3-5.	$^{56}\text{Fe}^+$ intensity versus low mass cutoff. 1 scan each data point (10 microscans each scan) . . . . .	51
3-6.	$^{56}\text{Fe}^+$ intensity versus $q_z$ for $m/z$ 56. 1 scan each data point (10 microscans each scan) . . . . .	52
3-7.	Copper isotope ion intensities versus $q_z$ ; a) $^{63}\text{Cu}^+$ intensity vs. $q_z$ for $m/z$ 63, b) $^{65}\text{Cu}^+$ intensity vs. $q_z$ for $m/z$ 65. 1 scan each data point (5 microscans each data scan) . . . . .	54
3-8.	$^{56}\text{Fe}^+$ intensity versus He buffer gas pressure. Error bars designate standard error of the mean. 50 scans each data point (1 microscan each scan) . . . . .	56
3-9.	$^{56}\text{Fe}^+$ intensity versus Ar buffer gas pressure. Error bars designate standard error of the mean. 50 scans each data point (1 microscan each scan) . . . . .	57
3-10.	Copper isotope ion intensities versus helium buffer gas pressure: a) $^{63}\text{Cu}^+$ intensity vs. He pressure, b) $^{65}\text{Cu}^+$ intensities vs. He pressure. Error bars designate standard error of the mean. 50 scans each data point (1 microscan each scan) . . . . .	59
3-11.	$^{63}\text{Cu}^+ / ^{65}\text{Cu}^+$ isotope ratio versus He buffer gas pressure. 50 scans each data point (1 microscan each scan) . . . . .	60

3-12.	Copper isotope ion intensities versus argon buffer gas pressure: a) $^{63}\text{Cu}^+$ intensity vs. Ar pressure, b) $^{65}\text{Cu}^+$ intensities vs. Ar pressure. Error bars designate standard error of the mean. 50 scans each data point (1 microscan each scan) . . . . .	62
3-13.	$^{63}\text{Cu}^+ / ^{65}\text{Cu}^+$ isotope ratio versus Ar buffer gas pressure . . . . .	63
4-1.	Laser desorption ionization mass spectra of trimethylphenylammonium bromide, a) full mass scan, b) single ion isolation of the m/z 121 fragment ion . . . . .	67
4-2.	LDI/MS/MS of 121 <sup>+</sup> ion of trimethylphenylammonium bromide . . . . .	68
4-3.	LDI/MS of sodium ions, a) positive (average of 5 scans, 20 microscans each scan), b) negative ion spectra. Several peaks are shifted to the right due to space charging (a) or calibration error (b) . . . . .	72
4-4.	LDI/MS of 2,5-dihydroxybenzoic acid . . . . .	75
4-5.	LDI/MS of 2,4-dinitroaniline . . . . .	76
4-6.	Mass chromatograms for LDI/MS of 2,4-dinitroaniline . . . . .	77
4-7.	LDI mass spectrum of sinapinic acid, a) full mass scan, b) isolation of molecular ion at m/z 224 . . . . .	80
4-8.	Daughter mass spectrum of sinapinic acid molecular ions produced by laser desorption ionization . . . . .	81
4-9.	Laser desorption ionization mass spectrum of spiperone (MW 395) . . . . .	84
4-10.	Matrix-assisted laser desorption ionization mass spectrum of spiperone using nicotinic acid matrix (0.5% TFA) in methanol . . . . .	85
4-11.	(M+H) <sup>+</sup> signal of spiperone versus scan for MALDI using an acidified nicotinic acid matrix and LDI . . . . .	88
4-12.	(M+H) <sup>+</sup> and 165 <sup>+</sup> fragment ion of spiperone versus scan . . . . .	90
4-13.	MALDI mass spectrum of spiperone using 2,5-dihydroxybenzoic acid with 0.1% TFA, a) laser irradiance = $6.4 \times 10^6 \text{ W/cm}^2$ , b) laser irradiance = $5.1 \times 10^6 \text{ W/cm}^2$ . . . . .	93

4-14.	MALDI mass spectrum of spiperone using 2,5-dihydroxybenzoic acid matrix in 70:30 acetonitrile:water and 0.1% trifluoroacetic acid (low mass cutoff = 150 u) . . . . .	96
4-15.	MALDI/MS of 74 ng of spiperone (4 $\mu$ L of 47 $\mu$ M methanol solution) mixed with 4 $\mu$ L of 48 mM DHB matrix solution . . . . .	98
4-16.	MALDI/MS/MS daughter spectrum of protonated spiperone, m/z 396 (average of 10 scans) . . . . .	101
4-17.	MALDI/MS/MS daughter spectrum of m/z 165 fragment ion of spiperone (average of 10 scans) . . . . .	104
4-18.	Electron ionization of spiperone off the solids probe on the ion trap mass spectrometer (10 microscans). Low mass cutoff during trapping was 40 u and ionization time was 2 ms . . . . .	105
4-19.	Methane chemical ionization of spiperone off the solids probe on the ion trap mass spectrometer (10 microscans). Reaction time was 25 ms . . . . .	107
4-20.	Intensity versus scan plot of protonated spiperone (m/z 396) using methane chemical ionization of spiperone off the solids probe (10 microscans). Reaction time was 25 ms. Manifold temperature was 100 degrees celsius. Initial solids probe temperature was 70 degrees celsius and the temperature ramp was 120 degrees/minute, but the maximum ion signal (at scan #132 and retention time 4:57) was obtained after the reaching the final probe temperature . . . . .	108
4-21.	MALDI mass spectrum leucine enkephalin, an example of a compound which cannot be thermally desorbed . . . . .	111
4-22.	MALDI mass spectrum of leucine enkephalin showing the appearance of adduct ions . . . . .	113
4-23.	LDI/MS of 5 $\mu$ L of spiperone in Matrigel mixture (100 ppm). No UV matrix compounds or TFA were added. The low mass cutoff is 40 u during trapping and storage. The mass spectrum is a single microscan . . . . .	116
4-24.	MALDI/MS of spiperone in Matrigel (average of 20 scans) . . . . .	118

4-25.	MALDI/MS of spiperone in Matrigel with isolation of $(M+H)^+$ of spiperone using DHB matrix solution (0.1% TFA) and low mass cutoff = 150 u. Mass spectrum shows effects of delayed ejection of ions or neutrals into the ion trap analyzer volume . . . . .	120
5-1.	Drawing of laser beam and sample probe tip placement for the external source. . . . .	127
5-2.	Schematic of external source configuration for laser desorption ionization/quadrupole ion trap mass spectrometer . . . . .	129
5-3.	Schematic of laser desorption external ionization ion trap showing the configuration of components for delayed laser triggering and resonant excitation . . . . .	131
5-4.	LDI/MS mass spectrum of trimethylphenylammonium bromide. Low mass cutoff is 10 u. Average of scans #5 through #20 . . . . .	135
5-5.	Plot of trimethylphenylammonium bromide ion intensities versus low mass cutoff for trapping and storage. Each data point is an average of the ion intensity from scan #5 through #20 . . . . .	136
5-6.	Plot of trimethylphenylammonium bromide $120^+/121^+$ ion intensity ratio versus low mass cutoff for trapping and storage. Each data point is an average of the ion intensity from scan #5 through #20 . . . . .	138
5-7.	Plot of trimethylphenylammonium bromide ion intensities versus laser energy % transmission. Each data point is an average of the ion intensity from scan #5 through #20 . . . . .	139
5-8.	LDI mass spectra of trimethylphenylammonium bromide: a) MS/MS of molecular ion at $m/z$ 136, b) MS/MS/MS of molecular ion ( $136^+ \rightarrow 121^+ \rightarrow$ fragments) . . . . .	141
5-9.	MALDI mass spectrum of spiperone using external configuration. Average of 10 microscans. 1 $\mu$ L of 47 $\mu$ M spiperone in methanol sample mixed with 1 $\mu$ L of 520 mM DHB matrix solution . . . . .	143
5-10.	Ion intensity of protonated spiperone, $m/z$ 396, from MALDI/MS versus scan for external source configuration . . . . .	144

5-11. MALDI/MS/MS daughter spectrum of protonated spiperone, m/z 396, using external source configuration. Average of 10 microscans. 1 $\mu$ L of 47 $\mu$ M spiperone in methanol sample mixed with 1 $\mu$ L of 520 mM DHB matrix solution. Resonant excitation frequency is 113 kHz and amplitude is 6 V (p-p) . . . . .	146
5-12. MALDI/MS of spiperone in Matrigel membrane. Average of 10 microscans. 2 $\mu$ L of 0.5 mg/mL of spiperone in Matrigel sample mixed with 2 $\mu$ L of 520 mM DHB matrix solution . . . . .	148
5-13. Ion intensity of protonated spiperone from MALDI/MS of spiperone in Matrigel membrane versus scan for external source configuration. 2 $\mu$ L of 0.5 mg/mL of spiperone in Matrigel sample mixed with 2 $\mu$ L of 520 mM DHB matrix solution . . . . .	149

Abstract of Dissertation Presented to the Graduate School  
of the University of Florida in Partial Fulfillment of the  
Requirements for the Degree of Doctor of Philosophy

DEVELOPMENT AND APPLICATION OF LASER DESORPTION  
IONIZATION ON A QUADRUPOLE ION TRAP MASS SPECTROMETER

By

Rafael Roberto Vargas

December 1993

Chairperson: Richard A. Yost  
Major Department: Chemistry

The purpose of this research is to develop and characterize laser desorption ionization (LDI) on a quadrupole ion trap mass spectrometer to evaluate the potential for development of the first true molecular microprobe. A nitrogen laser was used to desorb and ionize solid samples, with the ions analyzed using tandem mass spectrometry (MS/MS). The ultimate goal of this method is to determine drugs in biological tissues and to obtain spatial information about drugs in the cellular matrix. This method would not only be able to detect molecular ions produced by laser desorption ionization, but also to determine the structure of the molecular ion of interest by performing MS/MS. A quadrupole ion trap mass spectrometer is utilized because of its sensitivity and selectivity, and its capability to obtain complete MS and MS/MS spectra from a pulsed source of ions.

In an internal ionization configuration, the laser beam is directed into the ion trap to focus upon the sample surface positioned flush with the ring electrode surface. In an external configuration, the laser beam is directed into an external ionization source with injection of the ions into the trap. LDI on the ion trap has been achieved and tandem mass spectrometry has been performed on laser-desorbed ions. Matrix-assisted laser desorption ionization (MALDI) has been evaluated to improve determination of spiperone and other thermally labile, nonvolatile compounds. Spiperone is a drug used in this research as a model of the drug compounds to which this method could be applied. Spiperone in Matrigel membrane, an extracellular matrix used as a tissue model, has been detected. Results were obtained which provide a better understanding of the laser-desorbed ion trapping process to increase the sensitivity of the method. For example, the trapping efficiency was found to be dependent on the radiofrequency phase angle during the laser pulse. The effects of buffer gas pressure and radiofrequency amplitude on trapping efficiency were also discussed. The results obtained demonstrated the potential of LDI/quadrupole ion trap mass spectrometry for achieving a highly sensitive and selective imaging technique for drugs in biological matrices.

## CHAPTER 1 INTRODUCTION

### Project and Goals

The ability to analyze specific drug compounds located in biological tissues provides pharmacological researchers with very useful information about the physiological and metabolic action of those compounds. With the use of a microprobe method, the specific site of reactivity or drug location could be determined in various regions of the cellular matrix (e.g., intracellular or extracellular). Microprobe methods currently available, such as laser microprobe/time-of-flight mass spectrometry, however, do not provide the selectivity to determine a wide range of drug compounds. Lack of selectivity can lead to erroneous identification of compounds, particularly in a complex matrix. The purpose of this research is to develop and characterize laser desorption ionization on a quadrupole ion trap mass spectrometer in order to evaluate the potential for development of the first true molecular microprobe. This method would not only detect molecular ions produced by laser desorption ionization, but also determine the structure of the molecular ion of interest by performing multiple stages of mass spectrometry. A quadrupole ion trap mass spectrometer is used because of its



sensitivity and selectivity, and its capability to obtain complete MS and MS/MS spectra from a pulsed source of ions.

In this research, laser desorption ionization has been achieved on the ion trap and tandem mass spectrometry of laser-desorbed ions has been performed. Matrix-assisted laser desorption ionization has been utilized on the ion trap to improve detection and determination of spiperone and other thermally labile, nonvolatile compounds. Spiperone is an antipsychotic drug that is used in this research as an example of the drug compounds to which this method can be applied. Spiperone in Matrigel membrane, an extracellular matrix used in this work as a tissue model, has been detected. Experiments to better understand the process of trapping laser-desorbed ions have been performed so that the sensitivity of the method may be increased. For example, a radiofrequency phase angle effect on the trapping efficiency of laser-desorbed ions was studied, an experiment that required the development of phase angle/laser trigger synchronization electronics. The effects of buffer gas pressure and radiofrequency amplitude on the trapping efficiency of laser-desorbed ions have also been shown.

### Previous Work

This research arose from the successful results previously obtained by Bob Perchalski performing laser desorption on a triple quadrupole mass spectrometer.<sup>1,2</sup> The researchers attempted to take advantage of long lived neutral production from a laser desorption method combined with chemical ionization (CI) so that the triple

quadrupole could be mass scanned across resultant the ion pulse. A triple quadrupole was used because of its ability to perform MS/MS and to perform rapid mass scans. In that work, a pulsed dye laser was interfaced with a Finnigan TSQ45 triple quadrupole mass spectrometer. Samples were mounted on electron microscope grids attached to stainless steel solids probe extensions. The surface angles were 45° or 90° for laser incidence and the ion pulse generation angles were 135° (along the quadrupole axis) or 90° (perpendicular to quadrupole axis), respectively. The method involved a mass scan over several seconds after a single laser event. With the long-lived ion production from CI of laser-desorbed neutrals, the quadrupole mass analyzer could be scanned across a selected mass range.

The results included MS/MS of phenytoin for successive laser shots. Peaks in the ion current versus time represented each laser pulse and the mass spectra obtained were found to be similar to those obtained from direct probe CI. In another study, the instrument was employed to monitor parent ion/daughter ion pairs for each of nine drugs in an antiepileptic drug mixture. The most impressive results were the detection of phenytoin in mouse liver tissue at low levels of concentration by obtaining complete daughter spectra of the laser-desorbed  $(M+H)^+$  ions.

In this research, it was apparent that obtaining complete MS or MS/MS spectra of ions produced by the laser event, and therefore with lifetimes of less than 1 ms, was beyond the ability of the instrument due to the length of the mass scan. However, the beam type instrument could analyze the ions produced by chemical ionization of laser-desorbed neutral molecules for up to one minute after a single

laser pulse. The research showed the potential of MS/MS for multicomponent, site-specific, molecular analysis by laser desorption MS/MS, but clearly demonstrated the value of an MS/MS instrument capable of analyzing the narrow pulse of laser-desorbed ions.

### Purpose of Using the Quadrupole Ion Trap

One of the most sensitive and selective mass spectrometers is the quadrupole ion trap mass spectrometer.<sup>3</sup> Originally utilized to study volatile organic species, the ion trap has been used recently to analyze various samples with the addition of various desorption and spray techniques. Nearly all of the recently developed desorption and/or ionization methods have been combined with the ion trap<sup>4</sup> because of the widely recognized potential of the instrument. Jodie Johnson in our group demonstrated that the ion trap has higher collision-induced dissociation efficiencies (typically 80-90%) for MS/MS than the triple quadrupole mass spectrometer (typically 50-60%).<sup>3</sup> In the same report, quantitative studies revealed that the ion trap could obtain complete daughter spectra on low picogram amounts of analyte, one hundred times lower than the amounts required for comparable spectra on the triple quadrupole.

While several researchers have demonstrated tandem mass spectrometry using dual time-of-flight stages of mass analysis,<sup>5,6</sup> this capability is not widely available as yet and has not been applied to laser sampling methods. Time-of-flight mass spectrometry (TOF MS), however, has been used for laser microprobe analysis. In

the 1970s, laser microprobes were developed with highly focused beams ( $< 1\ \mu\text{m}$  spot size) which could be aimed at a selected location on a sample surface.<sup>7</sup> Initially, these instruments were used only for elemental analysis and mapping surfaces for elemental concentration. Several years later, the first methods to produce molecular ions from laser desorption appeared and were applied to laser microprobe instruments. Materials that were studied with this technique included polymers, metals, biological materials, and semiconductors.<sup>8</sup> For biological materials such as rabbit liver tissue, the localization of aluminum in cells was performed using this method.<sup>9</sup> These laser microprobes, however, incorporate only a single stage of time-of-flight mass spectrometry and thus cannot perform tandem mass spectrometry.

Laser microprobe Fourier-transform mass spectrometry (FTMS) instrumentation is available commercially (e.g., EXTREL Laser Probe<sup>TM</sup> MS). These instruments provide accurate mass measurement and high resolution. Molecular weight and structural information on biomolecules and polymers have been obtained using these instruments.<sup>10</sup> Multiple stages of analysis can be performed with dual cells or stored waveform inverse Fourier-transform excitation, and picomole detection limits have been obtained for biomolecules.<sup>11</sup> Laser microscopy for trace level analyses, however, has not been utilized with this method.

Multiple stages of mass analysis ( $\text{MS}^n$ , where  $n \leq 13$ ) have been demonstrated on the quadrupole ion trap.<sup>4</sup> The ion trap is also much simpler and more compact than other tandem mass spectrometry instruments such as sector, hybrid sector/quadrupole, triple quadrupole, or FTMS instruments. Smaller instrument size,

as well as less stringent vacuum requirements, is also characteristic of the ion trap not shared by the Fourier-transform instruments. In terms of figures of merit, the best results obtained for limits of detection for the ion trap are in the attomole ( $10^{-18}$  mole) region.<sup>4</sup> The best linear dynamic range reported equaled over six orders of magnitude.<sup>12</sup> As are these figures of merit, analytical utility is an important quality of an instrument. With the addition of very different ionization methods, the ion trap has been used to study a wide range of samples from volatile organic molecules to involatile inorganic and biological molecules. In particular, when analyzing biological molecules, ionization methods including electrospray ionization and atmospheric glow discharge ionization have been performed successfully on the ion trap and can provide analytical information complementary to the information obtained using laser desorption ionization.<sup>13</sup>

The future of the quadrupole ion trap holds much promise as well. Recent research has demonstrated dramatic increases in the mass range; ions of masses up to 70,000 u have been detected.<sup>14,15</sup> High mass resolution has been performed by others as well.<sup>16,17</sup> These advances in ion trap technology have greatly increased the ion trap's ability to analyze large molecules.<sup>18,19</sup>

Ongoing research also suggests that the future of the quadrupole ion trap will include a wider range of analytical applications, improved resolution, combination of the trap with other separation methods, the automation of the acquisition of MS/MS data, and the study of different trap geometries as well as nondestructive means of ion detection.<sup>20</sup> Also in our group at the University of Florida, the ion

trap has also been studied for use as analyzer for an expert system to monitor enclosed environments autonomously; suggesting an instrument completely free of operator input and control.

## Quadrupole Ion Trap Mass Spectrometry

### History

In 1956, Wolfgang Paul first described a device using only electric fields for containing gaseous ions.<sup>20</sup> By the time Paul and Hans Dehmelt were awarded half the Nobel Prize in physics in 1989, the quadrupole ion trap had successfully made a place for itself in the analytical sciences. The commercial introduction of the trap was in 1983 as the Finnigan MAT Ion Trap Detector; over the past decade it has become a standard instrument for mass spectrometry.<sup>4</sup>

Certain advances in ion trap technology were required for the instrument to become an analytically useful tool in chemistry. These advances include the addition of a light buffer gas,<sup>21</sup> alternative scan functions such as parent scans to increase analytical usefulness,<sup>22</sup> positive and negative chemical ionization,<sup>23</sup> ion isolation and tandem mass spectrometry.<sup>20</sup> The ability to combine the ion trap with chromatography has proven to be the most useful of all applications, and currently the ion trap is most widely used in the form of a benchtop gas chromatography/MS system.

## How the Ion Trap Works

The quadrupole ion trap is made up of three cylindrically symmetric electrodes, two endcap electrodes with a ring electrode between them. The inner surfaces of these electrodes are hyperbolic. In the common method used here, the two endcaps are grounded while the trapping radiofrequency (rf) potential, also known as the drive potential, is applied to the ring electrode, as shown in Figure 1-1. This radiofrequency is typically around 1 MHz. The Finnigan MAT Ion Trap Mass Spectrometer (ITMS), used for the internal configuration, operates at a drive frequency of 1.1 MHz. The trap is controlled by a computer processor to allow complete adjustment of scan functions and data collection using only a personal computer. Scan functions represent the temporal variation of the rf potential applied to the ring electrode and are used to display the relationship between the trapping field and other events that occur during a mass analysis experiment (e.g., ionization, cooling, isolation). Using a personal computer, the operator only needs to write an MS or MS/MS scan function into the software; no other hardware or electronics modification is necessary.

After ions are created within the trap by injection of electrons through an endcap electrode, or after ions are injected into the trap, ions of a range of mass/charge values may be held in stable orbits inside the trap depending on the amplitude of the rf potential applied to the ring electrode. A stable orbit has the form of a three-dimensional Lissajous figure and is defined by the radial and axial frequencies of motion.

## Ion Trap Mass Spectrometer (ITMS™)

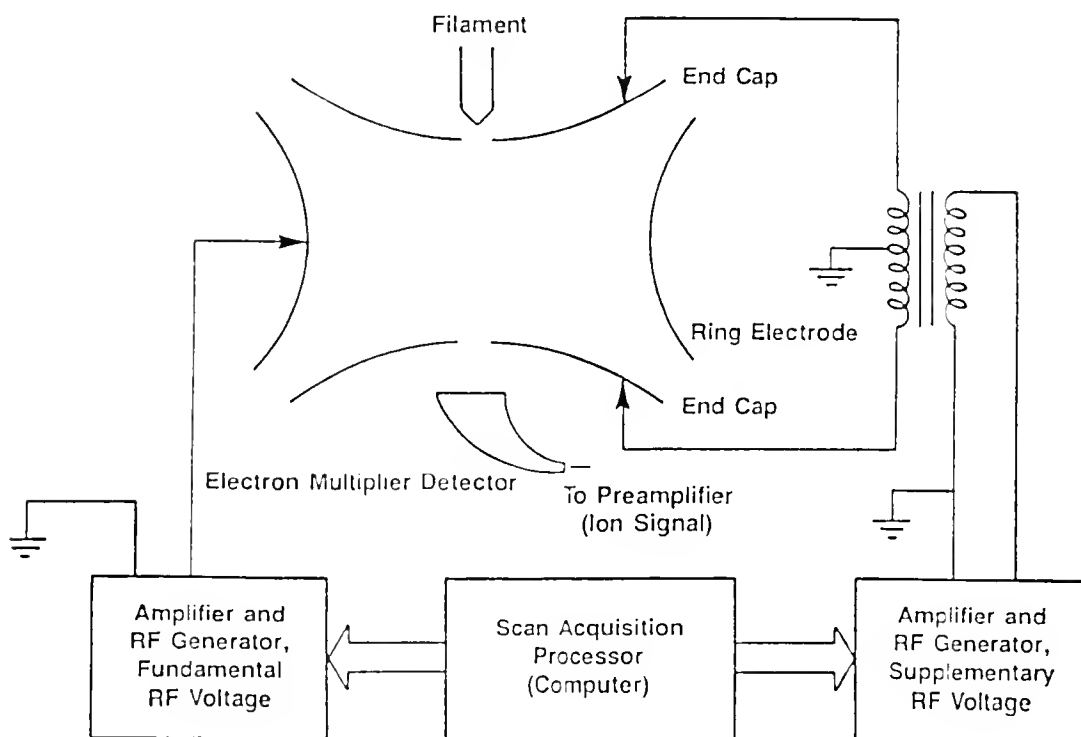


Figure 1-1. Schematic of quadrupole ion trap mass spectrometer showing which electrodes the various voltages are applied and the configuration of the filament and detector.



As the amplitude of the rf is increased, ions of increasing mass/charge value approach the low mass cutoff, become unstable in the z-direction (towards the endcaps), and exit the ion trap through holes in one of the endcaps and strike a detector. The detector positioned behind one of the endcaps is typically an electron multiplier that produces the ion current signal. Most often, several mass scans, called "microscans," are summed and the averaged mass spectrum is sent to the computer for display and recording.

### Performing MS/MS on the Ion Trap

As stated previously, performing MS/MS on the quadrupole ion trap only requires editing the software in order to carry out the added steps required in a scan function. Several methods exist for performing MS/MS. Apex isolation is the most common method of ion isolation in the ion trap; as do most other methods, it requires a dc potential applied to ring electrode. The proper setting of rf and dc potentials, which will be discussed in detail in Chapter 2, will create an electric field inside the ion trap where only ions of a particular mass/charge value will have a stable trajectory and all other ions of masses above and below that value will have unstable trajectories. These other ions will be ejected from the trap or strike an electrode, and they will no longer be stored and detected in the subsequent mass scan.

The purpose of isolating ions of a single mass/charge is so that they (the parent ions) may be fragmented and the ions produced (the daughter ions) will not

be interfered with by the other ions. These daughter ions, will then be products only of the parent ion and the information obtained in the daughter ion spectra can be utilized as such. Several methods also exist for fragmenting the parent ion. Throughout the work presented in this dissertation, the method of resonantly enhanced excitation of the parent ion for collisionally induced dissociation (CID) was used. Application of a resonant excitation voltage (applied across the endcap electrodes) induces the parent ions to achieve more energetic orbits in the axial direction. These energetic orbits cause the parent ions to collide with the required buffer gas inside the trap; these collisions can eventually lead to dissociation as presented in the reaction



where  $\mathbf{P}^{+}$  is the parent ion,  $\mathbf{D}^{+}$  represents the daughter ions, and  $\mathbf{N}$  represents the neutral fragments. The daughter ions that are trapped can then be scanned to obtain a daughter mass spectrum. As stated previously, tandem mass spectrometry provides a second dimension of selectivity and valuable information for ion identification.

### LDI and MALDI Combined with MS

Laser desorption is a method by which atoms and molecules in the condensed phase are transferred to the gas phase through the absorption of sufficient energy from laser radiation. The process produces both neutral and ionic species. Laser desorption ionization (LDI) is used in this dissertation to specify exclusively the

production of ionic species. The history of lasers combined with mass spectrometry began about thirty years ago with the use of high laser energies to perform elemental analyses.<sup>6</sup> With the eventual addition of molecular ion analyses to the laser desorption method,<sup>6</sup> the technique showed great potential as an analytical tool. Adding to this potential is the ability to tightly focus laser beams all the way down to their diffraction limits making microscopic imaging by LDI possible. When tight laser focussing was not necessary, laser radiation can easily be introduced into the vacuum chambers and ionization sources using fiber-optics.<sup>24,25</sup> LDI mass spectrometry has been used primarily as a qualitative technique, but there have been many applications of LDI/MS to quantitative studies as well.<sup>26</sup>

Several other uses of lasers with mass spectrometry have made a widespread appearance over the past several decades. Laser photodissociation has been performed with mass spectrometry.<sup>27</sup> The many different photodissociation methods include two-pulse experiments, where the first pulse is used to desorb ions and the second pulse is used to photodissociate those ions. The pulses can both come from a single laser or individually from two different lasers, the second of which (the photodissociation laser) is tuned to the desired frequency for absorption by the ions. Combination of laser desorption with chemical ionization, to perform CI on laser-desorbed neutrals, has also been achieved.<sup>28</sup>

Laser desorption is a very versatile analytical tool because it can produce positively and negatively charged species.<sup>29</sup> The ionic species may be either singly charged or multiply charged. The species produced can also vary from atomic to

molecular and quasi-molecular particles. Much research has been performed over the last two decades to study the controlling factors in determining the species produced and to manipulate the laser desorption conditions to obtain the desired products.<sup>6</sup>

Most of the theories presented for the production process of laser-desorbed particles are divided into two categories based upon the general conditions of laser desorption. The first condition involves the slow thermal heating of the sample upon laser irradiation.<sup>8</sup> This process typically creates a long lasting ion pulse that lasts from several milliseconds up to several seconds in length. Often, this thermal process is performed using an infrared laser. The second condition involves the quick ablation of the sample upon laser irradiation.<sup>8</sup> This fast process usually produces an equally fast ion pulse that lasts from several nanoseconds up to several microseconds in length and is often performed with an ultraviolet laser. A very important characteristic of this method is the lack of thermal energy transfer from the sampling spot to the surrounding sample.<sup>30</sup> In electron micrographs of sample craters produced from this nonthermal process, the hole is usually very clean and has the same shape as the laser beam profile. Also, there is no visible charring of the surrounding sample. The methods of laser desorption ionization and matrix-assisted laser desorption ionization discussed in the following chapters are both part of the second condition of laser desorption.

Mass spectra of the ions produced from laser desorption typically show ions with even numbers of electrons; protonation and deprotonation are favored over

electron removal or addition.<sup>30</sup> Cationization by alkali metal ions also occurs very frequently. This tendency has been utilized to improve the production of ions by increasing the appearance of molecular adduct ions (also called quasi-molecular ions). The ions produced routinely have a widespread kinetic energy range.<sup>31</sup> Average kinetic energy of laser-desorbed ions also varies over the time immediately after the laser pulse.<sup>29</sup> The more polar a sample is, the more easily it can be desorbed as an ion. This relationship is opposite to what is normally considered for electron ionization or chemical ionization, in which the required volatility is generally favored by lower polarity. It is also common practice to use preformed ions for calibration and testing purposes in LDI/MS. The important parameters in laser desorption are photon wavelength, laser irradiance, laser pulse width, absorption spectrum of the sample, the orientation of the impinging laser beam to the sample, sample thickness and smoothness, sample homogeneity, and substrate composition. These parameters will be given for each of the various experiments presented throughout this dissertation and periodically discussed for their effect on obtaining good mass spectra.

### Matrix-assisted LDI

As stated before, when the use of lasers with mass spectrometry first began, the high laser irradiances available were applied to the rapid vaporization of materials for elemental analysis and pyrolysis. The method of matrix-assisted laser desorption ionization (MALDI), as first introduced by Hillenkamp and Karas in

1987, makes possible routine analysis of *intact* biological molecules.<sup>30,32</sup> The molecular weights of biomolecules, therefore, can be obtained. These molecules include peptides, proteins, glycoproteins, glycosides, nucleosides, nucleic acid, and oligosaccharides. Molecular masses of up to approximately 300,000 u have been obtained using MALDI and studies to improve sensitivity and resolution continue to be reported.<sup>33</sup> Although MALDI has been primarily used to study biological molecules with molecular masses of 1000 u or greater, the mass range of analytes is much lower in the research discussed in later chapters. MALDI is used in this research to increase the production of molecular ions to increase sensitivity, since the analytes are thermally labile compounds and easily fragmented by laser desorption ionization.

### How MALDI Works

In order to avoid fragmentation, a matrix compound rather than the analyte absorbs the laser pulse energy. Further, analyte molecules are separated within the matrix to prevent clustering, as shown in Figure 1-2. The matrix molecules, which typically outnumber the analyte molecules 1000-to-1, also provide a source of hydrogen for protonation reactions. In effect, the matrix absorbs the laser energy which volatilizes the analyte molecules, and soft chemical ionization of analyte occurs in the selvedge region just above the sample surface.<sup>30</sup> The matrix compounds share the following characteristics: low sublimation temperature, high absorptivity at the laser wavelength, and miscibility of the matrix solution with the analyte solutions.<sup>30</sup>

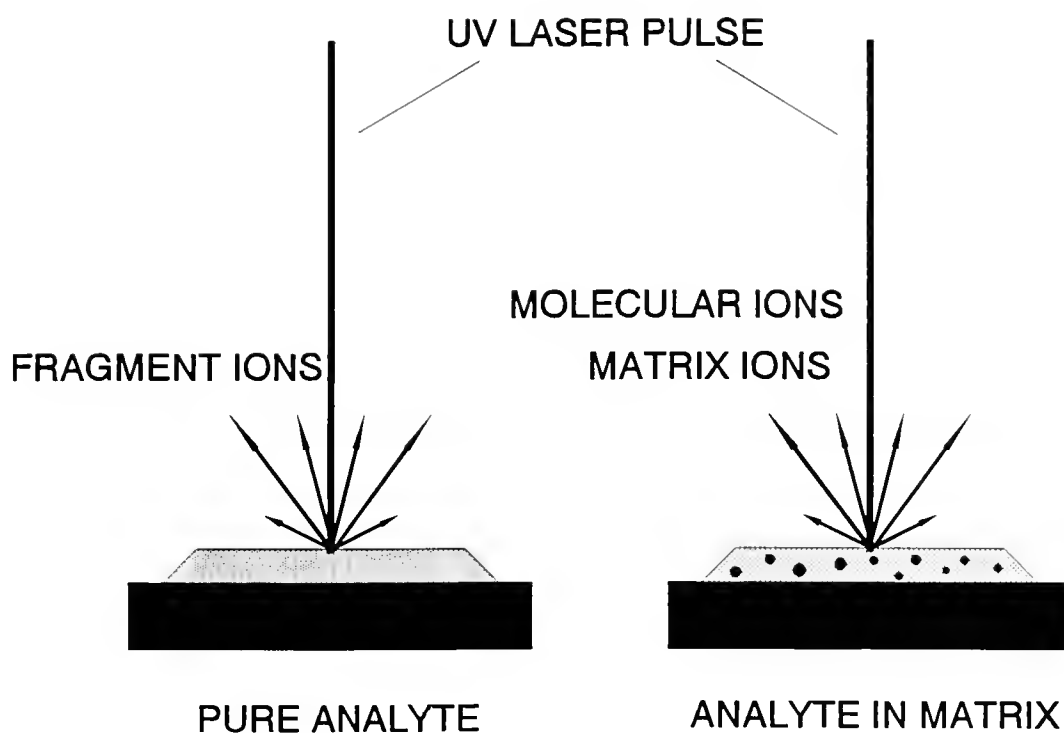


Figure 1-2. Illustrative comparison of LDI and MALDI sample composition and ionization products.

Thus far, the MALDI ionization mechanism has not been completely understood. What is known is that MALDI provides an effective and controlled transfer of the laser energy to the condensed phase by predominantly one-photon absorption.<sup>29</sup> This absorption is then followed by an expansion of analyte ions carried away by the ejection of matrix molecules from the sample surface. MALDI therefore involves the ablation of several layers of molecules per laser shot and is considered a bulk analysis method, as opposed to a surface method. The irradiance threshold for optimum molecular ion production is uniform and around  $10^6 \text{ W cm}^{-2}$ . Pan and Cotter, using a delayed ion extraction linear time-of-flight MS method, have shown the average velocity of ions produced by MALDI to be approximately 1000 m/s.<sup>34</sup> In a separate study, Beavis and Chait showed the average velocity is approximately 750 m/s and independent of the ion mass.<sup>35</sup> These velocity characteristics, along with other characteristics, demonstrate that ion production depends primarily on the matrix molecules, not on the analyte molecules. This property is seen in the uniformity of the sample preparation methods and the quality of the mass spectra obtained from MALDI.

Typical ultraviolet energy sources used are pulsed Nd:YAG, excimer, and nitrogen lasers. The matrix compounds used are sinapinic acid, gentisic acid, nicotinic acid, nitrobenzyl alcohol, and derivatives of these compounds.



### Comparison to Other Desorption Methods

As mentioned before, MALDI is a bulk method, whereas secondary ion mass spectrometry (SIMS) and fast atom bombardment (FAB) MS are surface methods. MALDI involves the analysis of many molecular layers, where SIMS and FAB analyze a single layer or a few layers.<sup>36</sup> For the purpose of microprobe analysis, FAB is typically not used since good spatial resolution or control of fragmentation cannot be achieved as with laser desorption.<sup>7</sup> SIMS, on the other hand, is commonly used as an ion microprobe technique. Originally, used for elemental mapping like laser microprobe mass spectrometry, SIMS is now also being used for the analysis of organic species as well.

In the SIMS method, a focused primary ion beam is rastered across the sample to produce secondary ions representative of that sample surface. The primary beam may be typically  $\text{Cs}^+$  ions with several keV of energy. The images produced give the intensity of mass-selected secondary ion emitted as a function of position of the primary ion beam. SIMS has been combined with triple quadrupole mass spectrometers, with the second stage of mass analysis improving the quality of the chemical image.<sup>37</sup> For nonconducting samples such as biological tissues, however, sample surface charging can occur from the influx of the primary ions, and decrease the efficiency of the desorption process.

## Recent Advances in LDI/Quadrupole Ion Trap MS

To introduce the following chapters on the dissertation research on laser desorption ionization/quadrupole ion trap MS, a short summary is given of work reported in this area. Details of these various studies by other research groups will not be given here as they will be provided in the appropriate chapters for comparison to the results presented in this dissertation.

Laser desorption on the quadrupole ion trap was first reported by Heller *et al.* in 1989.<sup>38</sup> A CO<sub>2</sub> laser was used to produce molecular and fragment ions from organic and biomolecular compounds. These compounds included sucrose and leucine enkephalin doped with potassium chloride to promote cationization. The configuration allowed the instrument to be used in its normal electron ionization mode as well. Electron ionization was also performed during the laser desorption ionization experiments, resulting in additional fragmentation in the mass spectra. Tandem mass spectrometry on laser-desorbed ions in the quadrupole ion trap was first reported by Glush *et al.* and used to demonstrate the production of daughter ions and granddaughter ions from laser-desorbed parent ions.<sup>39</sup> The researchers also applied this new technology for mixture analysis.<sup>40</sup>

Laser ablation sampling inside the ion trap volume has been used to obtain direct atomic mass spectrometric analysis of solid metal samples.<sup>41</sup> A pulsed Nd:YAG laser beam was used to ablate sample pins inserted radially through the ring electrode and a mass spectrum of silver solder was obtained. The preliminary results reported for laser desorption on the ion trap demonstrated the potential to

combine the attributes and advantages of both methods to achieve an instrument unique in analytical capability, sensitivity, and selectivity.

### Overview of Dissertation

At the beginning of this research project, only preliminary results by two research groups had been reported for laser desorption inside the ion trap.<sup>38,39</sup> Therefore, little was known about either the fundamentals of trapping laser-desorbed ions, or the ability to detect thermally labile molecules with this method. The interface of hardware, electronics, and software to achieve laser desorption on the ion trap is described in Chapter 2 of this dissertation. With the instrumentation in place and functioning, the first step in this research was to determine and characterize the most important factors in trapping ions formed at the ring electrode surface, particularly when it was possible that laser-desorbed ions were too energetic to be trapped efficiently. These factors include buffer gas pressure and low mass cutoff settings. It was also believed that the radiofrequency phase angle at the instant of laser desorption could affect trapping efficiency if the ion pulse was shorter in time than the trapping radiofrequency cycle. All of these fundamental studies are described in Chapter 3 of this dissertation.

The second step in this research was to develop the capability to desorb and ionize molecules of interest intact with little or no fragmentation. Matrix-assisted laser desorption ionization had not been performed on the ion trap for this purpose. Therefore, the use of MALDI on the ion trap was evaluated. The best use of laser

irradiance for trapping, the length of the ion signal, and the sample preparation with UV-absorbing matrices were studied. The results of these studies are given in Chapter 4. In Chapter 5, the external configuration for laser desorption is presented and compared to the internal method. Both methods are considered for their effect on ion signal lifetime, sensitivity, and ability to perform MS/MS. Chapter 6 summarizes all of the conclusions drawn from the previous chapters and includes suggestions for future studies.

## CHAPTER 2 INSTRUMENTAL AND EXPERIMENTAL DESCRIPTION

### Instrumental Description

#### Ion Trap Mass Spectrometer

A Finnigan MAT Ion Trap Mass Spectrometer (ITMS<sup>TM</sup>) was used for this research. It has MS<sup>n</sup> capability with the use of a Selective Mass Storage box (dc voltage supply) and an auxiliary frequency synthesizer for resonance excitation (tickle voltage) and axial modulation. A base pressure around  $8 \times 10^{-8}$  torr is maintained inside the heated manifold by a turbomolecular pump (170 L/s pumping speed). Helium is introduced into the manifold through a Granville-Phillips leak valve to act as a buffer gas and help trap and collisionally cool ions to the center of the trap. Gas pressures were measured on the ITMS by a Bayard-Alpert type ionization gauge (Granville-Phillips) mounted on the vacuum chamber. Pressure measurement corrections were made for helium using factors determined in our laboratory.<sup>42</sup> The mass-selective instability scan, or ramping the radiofrequency (rf) voltage as described in Chapter 1, was used for ion detection.<sup>21</sup> Ion currents were measured outside the ion trap during rf voltage ramping by an electrically shielded electron multiplier. In several experiments, a conversion dynode was also used to increase sensitivity.

## Ion Trap Theory

Several parameters to describe ion motion are used in later chapters to discuss the laser desorption results. The derivation of these parameters from ion trap theory is given here; equations were obtained from March and Hughes.<sup>43</sup>

The potential ( $\phi$ ) inside the ion trap is described by the following equation

$$\phi = \frac{1}{2} (U + V \cos \Omega t) \left( \frac{x^2 + y^2 - 2z^2}{r_0^2} \right) + \frac{U + V \cos \Omega t}{2} \quad (2-1)$$

where  $U$  represents the maximum dc potential and  $V$  the maximum rf potential (0-peak) applied between the ring and endcap electrodes,  $\Omega$  is the angular frequency of the rf drive potential,  $t$  is time,  $x$ ,  $y$ , and  $z$  are the directions inside the ion trap. The  $x,y$  plane leads out from the center of the trap to the nearest ring surface (e.g., the radius) and the  $z$  axis leads out from the center of the trap to the endcap electrodes. The parameter  $r_0$  is the internal radius of the ring electrode. Conventional ion traps use a geometry in which  $r_0^2 = 2z_0^2$ , where  $2z_0$  is the closest distance between the two endcaps, although all commercial traps actually are stretched in the  $z$ -axis from the conventional geometry.<sup>44</sup> The oscillation of the rf potential creates a dynamic electronic field inside the trap where ions are forced in one direction and then forced in the opposite direction in both the radial and axial planes. The force acting upon an ion of mass  $m$  and charge  $ze$  is given by

$$F = -ze \cdot \nabla \phi = mA \quad (2-2)$$

where  $\nabla$  represents  $(d/dx + d/dy + d/dz)$  and  $A$  is the acceleration vector. This relationship leads to representations of the forces acting upon the ion in the  $x$ ,  $y$ , and  $z$  and given by

$$\left(\frac{m}{e}\right)x + (U + V \cos \Omega t) \frac{x}{r_0^2} = 0 \quad (2-3)$$

$$\left(\frac{m}{e}\right)y + (U + V \cos \Omega t) \frac{y}{r_0^2} = 0 \quad (2-4)$$

$$\left(\frac{m}{e}\right)z - (U + V \cos \Omega t) \frac{2z}{r_0^2} = 0 \quad (2-5)$$

None of these expressions contain cross-terms between  $x$ ,  $y$ , and  $z$ , so the ion motion may be resolved into each of the respective perpendicular coordinates. The  $x$  and  $y$  components are identical and may be treated independently if angular momentum is ignored about the  $z$  axis. Due to the cylindrical symmetry, the  $x$  and  $y$  components are combined to give the radial component  $r$  using  $x^2 + y^2 = r^2$ .

The  $z$  component of motion is out of phase by half a cycle with respect to the  $x$  and  $y$  motions (therefore the minus sign); the factor of two arises because of the asymmetry of the device caused by the need to observe the Laplace condition  $\nabla^2 \phi = 0$  when applied to equation 2-1. These equations are all examples of the Mathieu

equation (the mathematics of ion stability within the trap follow the Mathieu second-order differential equation), which has the generalized form

$$\frac{d^2u}{d\xi^2} + (a_u + 2q_u \cos 2\xi)u = 0 \quad (2-6)$$

where

$$u = x, y, z \quad (2-7)$$

$$\xi = \Omega t/2 \quad (2-8)$$

$$a_z = -2a_x = -2a_y = -\frac{8eU}{mr_0^2\Omega^2} \quad (2-9)$$

and

$$q_z = -2q_x = -2q_y = -\frac{4eV}{mr_0^2\Omega^2} \quad (2-10)$$

and where  $\xi$  is a dimensionless quantity. Thus the equations 2-7 to 2-10 relate the Mathieu parameters  $a_z$  and  $q_z$  to the experimental variables and also to the time variables  $\Omega$  and  $t$ . The  $a$  and  $q$  parameters are very important to the operation of the trap since they determine whether the ion motion is stable or unstable. The



diagram shown in Figure 2-1 defines the primary region within which the axial and radial components of motion are stable, the region of overlap indicating the  $a_z$ ,  $q_z$  coordinates corresponding to those ions that are held in the trap. The plot is called the stability diagram.

Lines drawn across the stability region in Figure 2-1 are called iso- $\beta$  lines, and describe the detailed trajectories of the ions at that point; the boundaries of the diagram correspond to  $\beta_r, \beta_z = 0$  and  $\beta_r, \beta_z = 1$ , with the boundary  $\beta_z = 1$  being that at which mass-selective instability is normally achieved during a mass scan.  $\beta$  values, as well as  $a_z$ ,  $q_z$  coordinates and ion secular frequencies, will be discussed in later chapters in reference to CID conditions, axial modulation, and black holes.

### Nitrogen Laser and Interface

A diagram of the laser desorption ionization quadrupole ion trap mass spectrometer is shown in Figure 2-2. The beam from a pulsed nitrogen laser (Laser Science 337ND) is directed through a UV-grade focussing lens and a low distortion quartz window mounted in a vacuum flange. The focussing lens (Melles-Griot) has a focal length of 25.4 cm. Neutral density filters were used to control the laser irradiance. Average beam spot size, as measured by the hole created by the laser on the sample surface, was approximately 0.04 mm<sup>2</sup>.

The nitrogen laser operates at a wavelength of 337.1 nm with a spectral bandwidth of 0.2 nm. It has a 3 ns pulse width (FWHM) with an average jitter of  $\pm 10$  ns, and a repetition rate  $\leq 20$  Hz. The laser energy is  $>250$   $\mu$ J/pulse with a

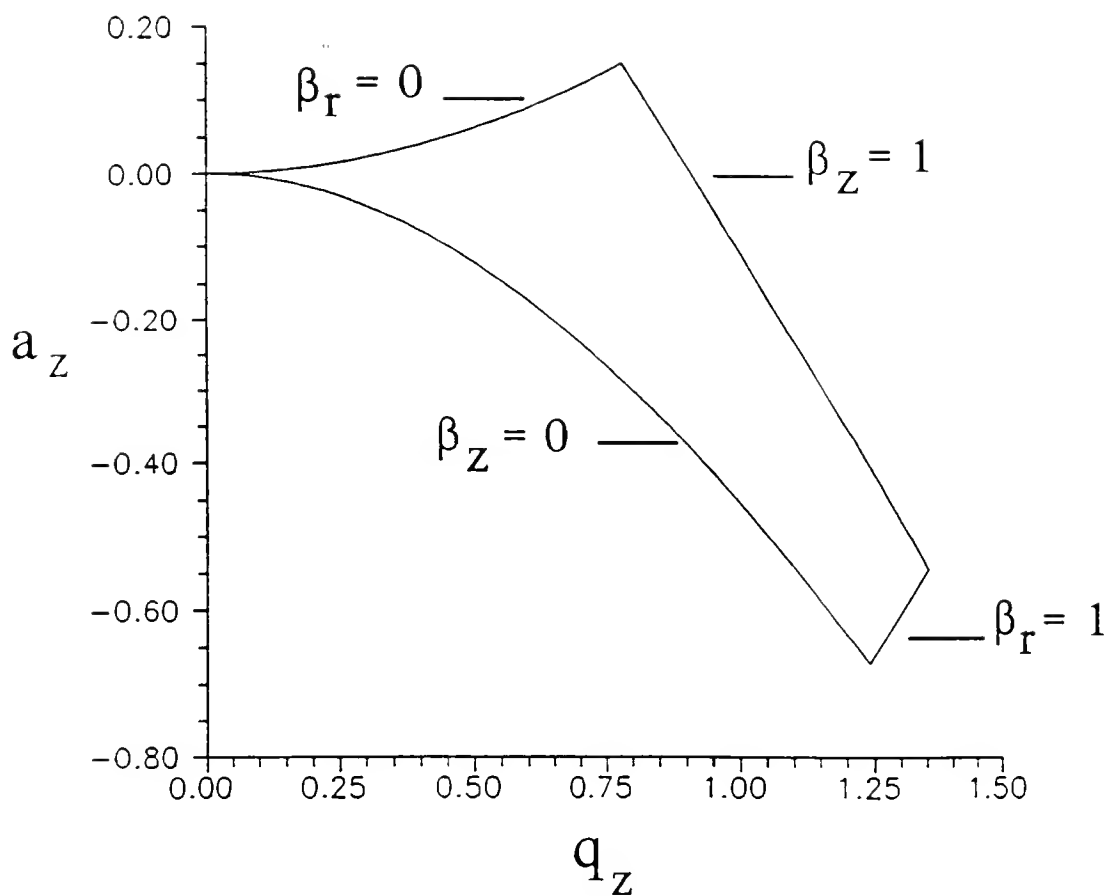


Figure 2-1. Plot of stability diagram defined by iso- $\beta$  lines. Ions which have  $a_z$ ,  $q_z$  coordinates within the bound region have stable trajectories.

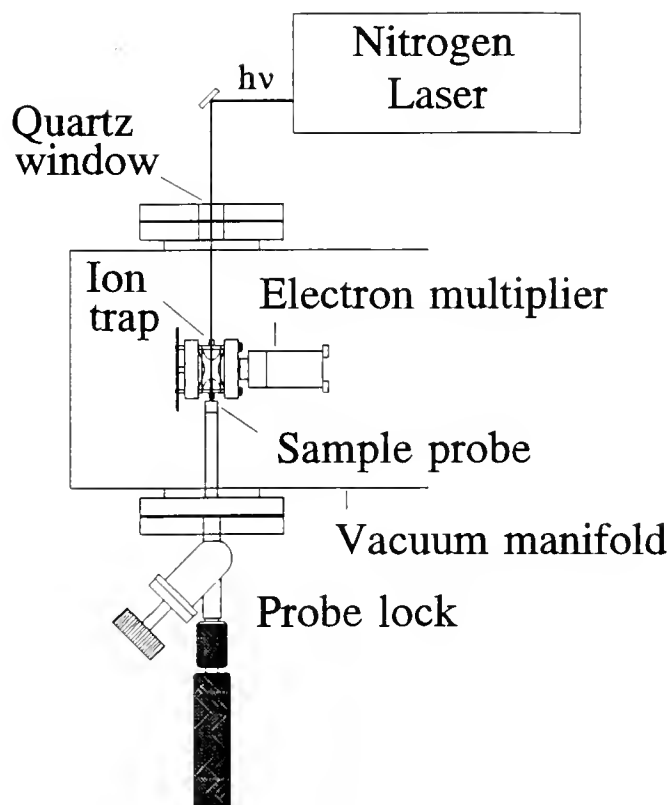


Figure 2-2. Schematic of laser desorption ionization/quadrupole ion trap mass spectrometer.

peak power of 85 kW, more than sufficient to produce large numbers of ions from all types of samples. The beam area is  $40 \text{ mm}^2$  with a beam divergence of  $<0.3 \text{ mrad}$ . Pulse-to-pulse stability is given to be  $\pm 4\%$  at a 10 Hz repetition rate. With the laser focussed to a spot size of around  $0.13 \text{ mm}^2$ , the irradiance is calculated to be approximately  $6 \times 10^7 \text{ W/cm}^2$  (this value does not include any constant attenuating factors such as the flange window). In typical applications, however, the laser is attenuated with neutral density filters to transmit only 5-10% of the energy, thus giving calculated irradiances around  $3 \times 10^6 - 6 \times 10^6 \text{ W/cm}^2$ . These values are near the optimum laser irradiances ( $1 \times 10^6 \text{ W/cm}^2$ ) for the ion production threshold for MALDI.

To enter the ion trap, the laser beam passes through a modified ring electrode via a 3.18 mm diameter hole as shown in Figure 2-3. The endcap electrodes were not modified. A sample is introduced into the vacuum manifold on the tip of a stainless steel probe through a flange-mounted vacuum probe lock. The tip of the sample probe is then inserted into the ion trap through a 3.18 mm diameter hole opposite the laser beam entry hole and positioned along the ring electrode surface. The instrument can be used in its conventional EI and CI modes with the laser desorption interface hardware in place.

Various materials have been used for the probe tip including stainless steel, copper, aluminum, glass, graphite, and Macor. Probe tips have 0.10 inch diameters and approximately 1 inch lengths. They are held in Teflon holders that are press fit into the stainless steel probe. These Teflon holders are very important since they

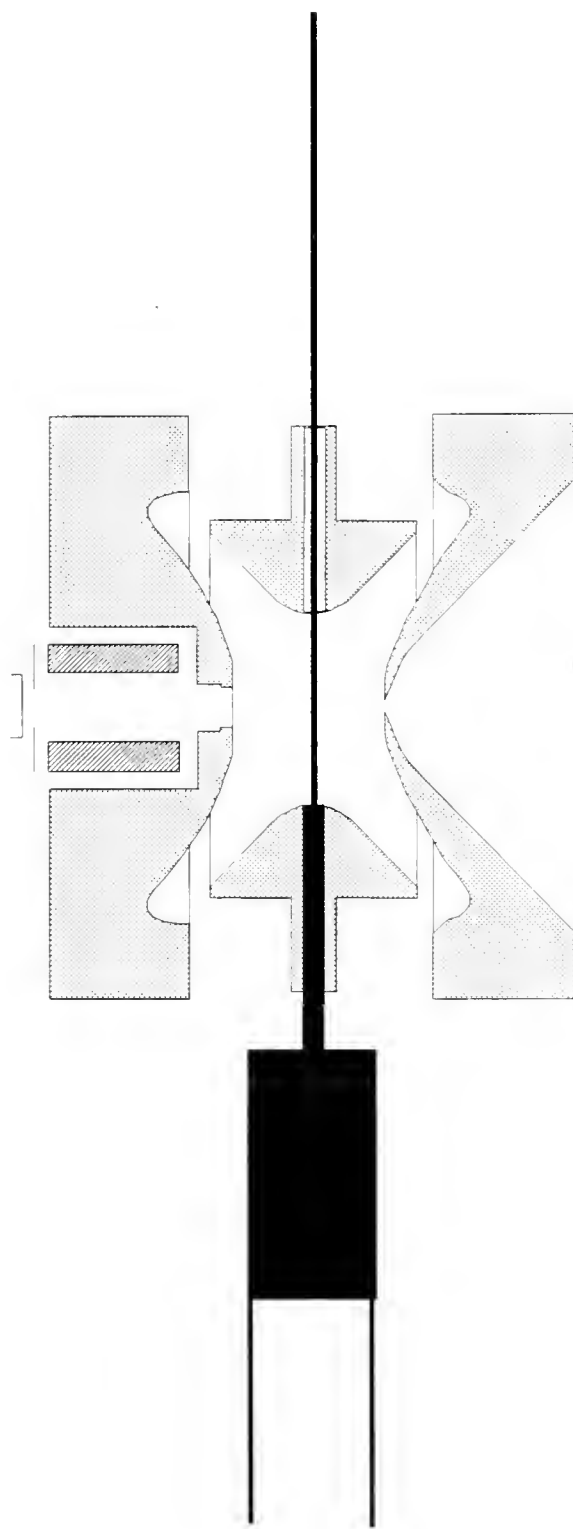


Figure 2-3. Schematic of laser/quadrupole ion trap showing the introduction of the laser beam and sample probe tip.

provide the electrical insulation between the rf ring and the operator-handled probe. The distance between the ring inner surface and the outside of the ring hole is 0.433 inches, and a mark indicating this distance on the probe tip is used as a guide to achieve a proper and constant insertion depth of the probe tip.

In order to aim the laser for sampling, fluorescence from the Macor probe tip surface is used to see the ultraviolet beam spot. The laser beam is aimed using a mirror and adjustable mirror mount. Typically, the laser spot is placed to one side of the probe tip surface and the tip is rotated so that several sampling spots can be obtained from a single sample residue.

### Experimental Setup

#### Scan functions and Timing

As stated in Chapter 1 for ion trap operation, scan functions represent the rf voltage amplitude over time for comparison to various events that occur during a single analysis step. The various events include, in sequential order, 1) electronics initialization trigger, 2) rf voltage warmup period, 3) laser trigger and ion trapping, 4) ion cooling and storage period, 5) multiplier warmup period, 6) rf voltage ramp and data acquisition scan, and 7) voltages off period for emptying trap of ions between scans. A scan function showing the important events is given in Figure 2-4. This scan function shows that a single laser pulse occurs during the trap and store time. The rf voltage during the laser pulse is set to a level that is required for trapping the ions of interest.

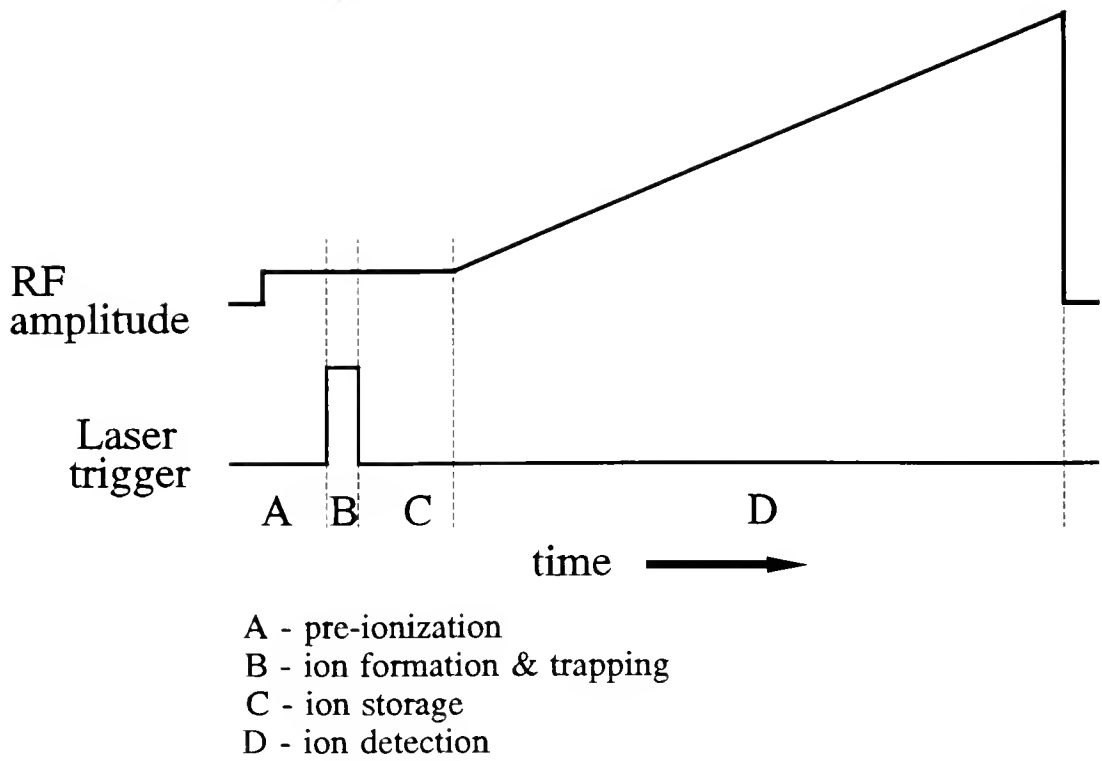


Figure 2-4. Drawing of rf scan function showing sequence of important events.

The proper timing of the laser pulse with the scan function is important to insure trapping of ions. Repetition rate of the scan function must not exceed the maximum pulse rate of the nitrogen laser (20 Hz). Typically, the scan function has a length of 100 ms that corresponds to the laser's optimum operating repetition rate of 10 Hz. The trigger that is sent to the laser comes from the ITMS electronics. Computer control of the laser trigger was established through software written in our laboratory.

### Trapping Radiofrequency Phase Synchronization Circuit

In order to synchronize the laser pulse with the rf phase angle, a trigger circuit was developed which utilized the clock pulse of the rf generator circuit and a TTL pulse controlled by the software. The scan table in the software is set to 100  $\mu$ s to insure laser triggering. As shown in Figure 2-5, the 1.1 MHz 15 V square wave (rf clock signal) of the rf generator and the asynchronous laser trigger (TTL pulse) were passed through a buffer and sent to the inputs of a dual edge-triggered flip flop (Motorola MC14013). The 1.1 MHz signal is sent to the clock input of the flip-flop and the TTL pulse is sent to the data input. The output signal of the flip flop circuit (Q1) is similar to the laser trigger signal except that the rising edge (Lo  $\rightarrow$  Hi) of the output pulse is synchronized with the rising edge of the rf clock signal. Q1 could be used to trigger the laser synchronously with the rf phase. Instead, Q1 is used to trigger a pair of monostables so that the rf phase angle during the laser pulse may be varied by adding a delay to the signal. The first monostable is triggered by the



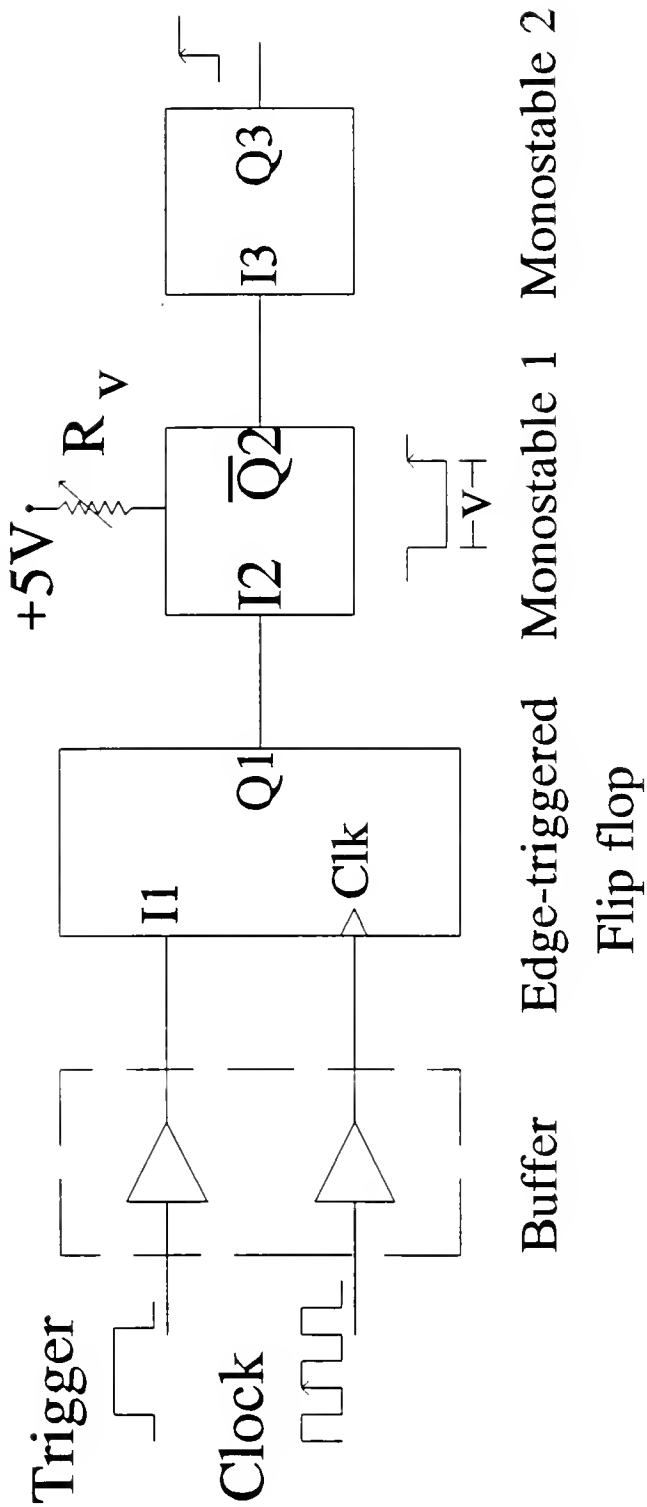


Figure 2-5. Diagram of the rf phase synchronization circuit. The variable resistor ( $R_v$ ) is adjusted for different rf phase angle settings during the laser pulse.

Q1 and the complementary output (Q2), or low pulse, of the signal is then sent to the second monostable. The Q2 signal is varied in length using a calibrated 10-turn variable 10 k $\Omega$  precision resistor (see Appendix A for calibration data). The rising edge of Q2 then triggers the second monostable that creates a high pulse (Q3) which is synchronized with the rf phase and variable over  $1\frac{1}{2}$  rf cycles.

A comparison is made between the laser pulse and the rf voltage on a digital oscilloscope by using the amplified response from a silicon photodiode (TL032) which is impinged upon by part of the laser pulse and the rf voltage (measured at the vacuum manifold feedthrough). The various signals described above are shown in Figure 2-6 where trace (a) is the initial software produced trigger, (b) is the rf clock, (c) is the rf synchronous trigger, (d) is the delay pulse with variable width  $v$ , (e) is the rf synchronous laser trigger, (f) is the photodiode response to the laser pulse, and (g) is the actual trapping rf field. It is important to note that at all times the low mass cutoff was maintained on the ITMS so that the rf voltage was measured at a safe level.

The turn settings of the precision resistor were calibrated to the pulse width ( $v$ ) of the first monostable and rf phase angle. Values obtained from this calibration were used to increment the laser pulse over several rf phase angles. The relationship between the pot number setting of the variable resistor and the rf phase angle is shown in Figure 2-7.

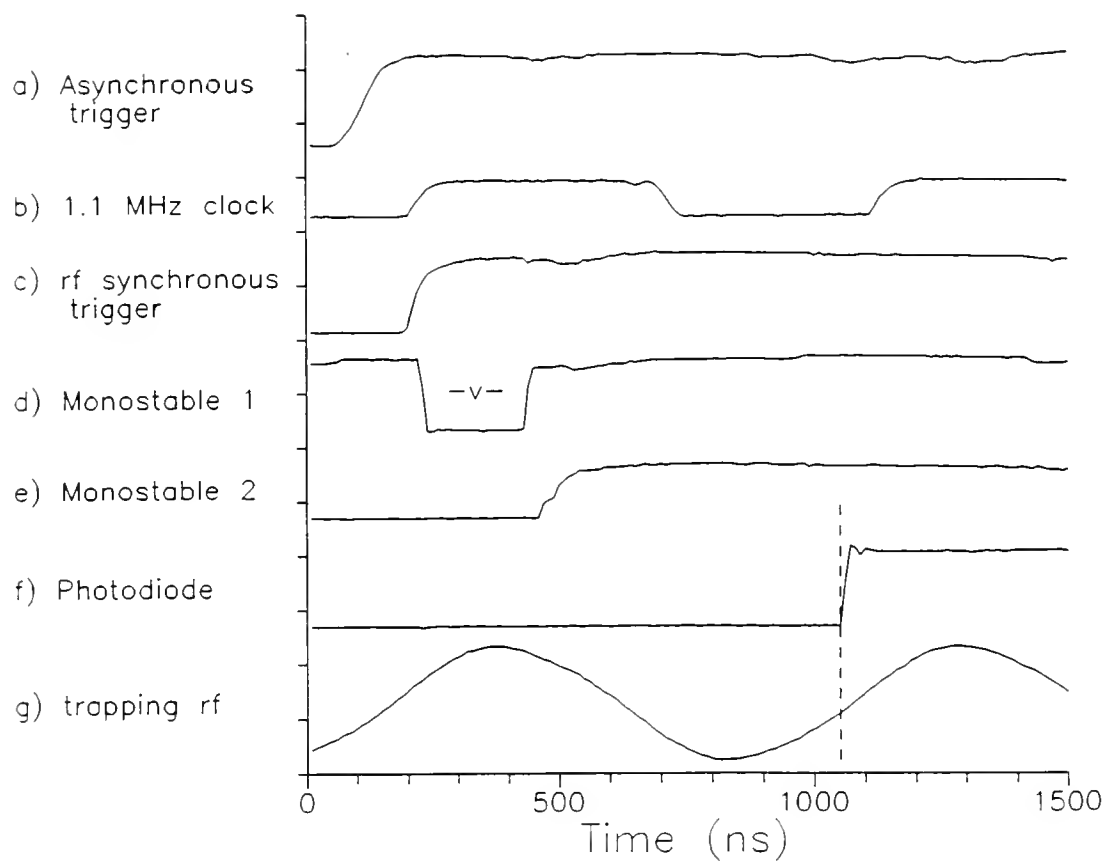


Figure 2-6. Timing dplot for rf phase synchronization experiment. See text for trace descriptions.

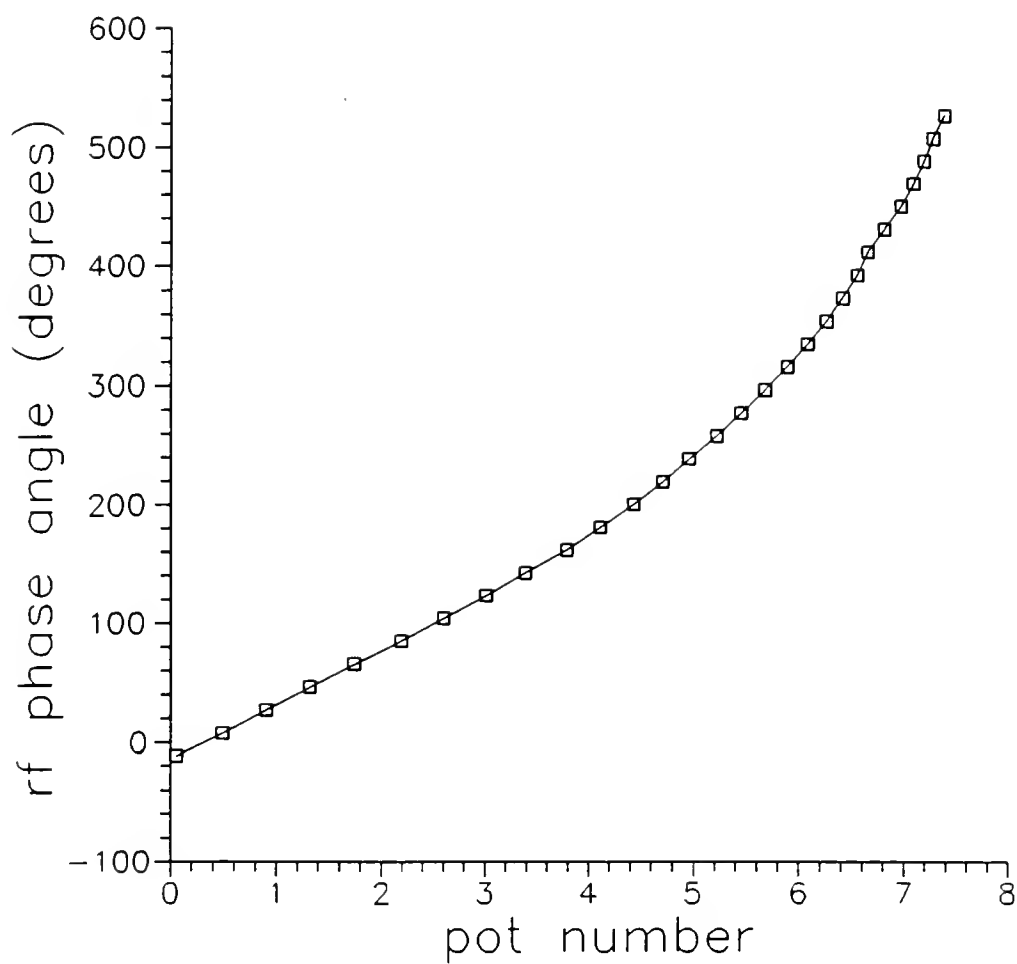
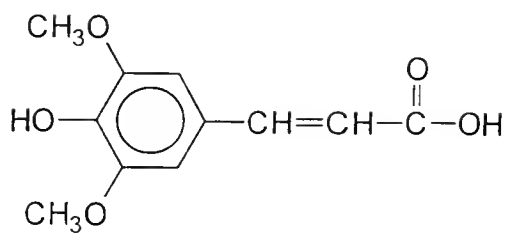


Figure 2-7. Plot of rf phase angle versus variable resistor position settings used for rf phase angle study.

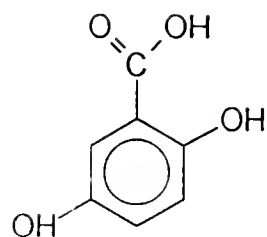
### Sample Preparation

Compounds of interest were dissolved in distilled water or methanol to various concentrations from a few micromolar to a few millimolar. The matrix solutions for MALDI were always dissolved in methanol with 0.1% trifluoroacetic acid. The matrix compounds used were sinapinic acid (MW 224), 2,5-dihydroxybenzoic acid (MW 154), 2,4-dinitroaniline (MW 183), coumarin-120 (MW 175), and nicotinic acid (MW 123). Structures and molecular weights of these matrices are given in Figure 2-8. Note that the molecular weights are all lower than 225 u and therefore do not interfere in the typically mass range of interest ( $>350$  u). As described in Chapter 1, the matrix compounds should absorb efficiently at the operating UV wavelength. A UV absorption spectrum of sinapinic acid (3,5-dimethoxy-4-hydroxycinnaminic acid) is given in Figure 2-9. The molar absorptivity at 337 nm was found to be  $14391 \text{ M}^{-1}\text{cm}^{-1}$ . The molar absorptivities at 337 nm for the other matrices are similar (coumarin-120,  $14519 \text{ M}^{-1}\text{cm}^{-1}$ ; 2,4-dinitroaniline,  $11971 \text{ M}^{-1}\text{cm}^{-1}$ ) except for nicotinic acid which is much lower ( $29.0 \text{ M}^{-1}\text{cm}^{-1}$ ). For the analyte compound studied in the following MALDI experiments, spiperone, the molar absorptivity at 337 nm is  $74.0 \text{ M}^{-1}\text{cm}^{-1}$ .

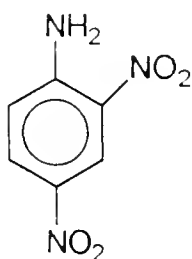
For laser desorption-ionization, 2 to 4  $\mu\text{L}$  of sample solution is deposited on a clean probe tip and air dried before placing in vacuum. For MALDI experiments, 2  $\mu\text{L}$  of the analyte solution is deposited on a clean probe tip followed by 2  $\mu\text{L}$  of matrix solution. The sample-matrix mixture is also air dried before placing in the vacuum. The method of matrix-assisted laser desorption ionization requires a dry



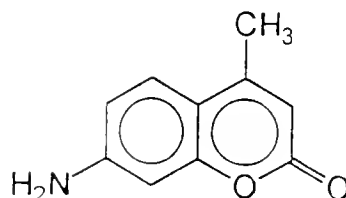
a) MW 224



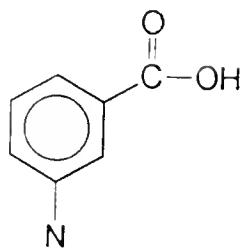
b) MW 154



c) MW 183



d) MW 175



e) MW 123

Figure 2-8. Structures and molecular weights of UV absorbing matrix compounds used for MALDI experiments: a) sinapinic acid, b) 2,5-dihydroxybenzoic acid, c) 2,4-dinitroaniline, d) coumarin-120, and e) nicotinic acid.

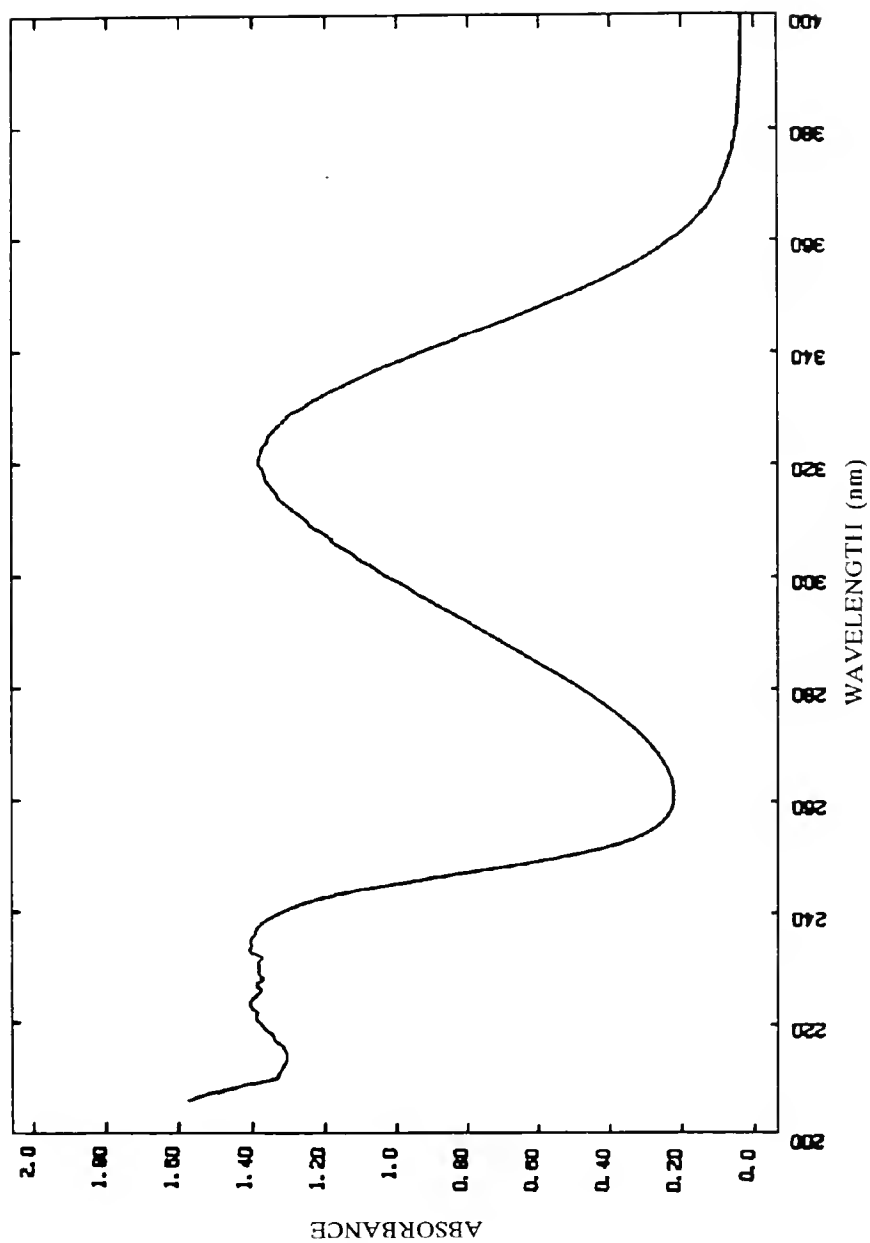


Figure 2-9. UV absorption spectrum of the matrix compound sinapinic acid. Molar absorptivity at 337 nm is  $14391 \text{ M}^{-1} \text{ cm}^{-1}$ .

homogeneous mixture of analyte and matrix on the probe tip, such that the analyte molecules are individually surrounded by matrix molecules. The equal volumes and 1:1000 concentrations give the analyte to matrix ratio that works best. When obtaining the first few mass spectra from a new sample, the laser transmission usually must be adjusted with the neutral density filters.



### CHAPTER 3

## FUNDAMENTAL STUDIES OF LASER DESORPTION IONIZATION/QUADRUPOLE ION TRAP MASS SPECTROMETRY USING AN INTERNAL CONFIGURATION

The laser desorption/ion trap system was modified and important instrumental parameters were studied in order to better understand the trapping process. In the instrumental configuration presented here, the trapping process for laser-desorbed ions resembles that of ion injection systems which have been previously demonstrated on the ion trap.<sup>45,46</sup> In contrast to the conventional ionization methods such as electron ionization which takes place within the ion trap volume, the laser-desorbed ions in these experiments are formed at the surface of the ring electrode, and therefore at both the physical and electrical stability boundaries for the ion trap. Ions formed at the position of the ring surface are then "injected" into the ion trap with the kinetic energy imparted by the laser desorption ionization process.

In theory, ions injected into the trap will eventually be ejected from the trap boundary because of the initial kinetic energy which allowed them to enter the radiofrequency trapping field.<sup>4</sup> The millitorr of helium buffer gas commonly used in the trap to improve sensitivity and mass resolution can also serve to collisionally cool injected ions,<sup>21</sup> as well as ions formed at the ring electrode. Trapping would be most favorable for ions of low kinetic energy and divergent from the symmetrical radiofrequency field plane which radially connects the ring electrode surfaces.<sup>21</sup> Ions

formed upon laser ionization at a solid surface would no doubt contain a wide range of injection angles to satisfy the latter property, but the average kinetic energy of laser-desorbed ions typically would be too high for efficient trapping. Therefore, the instrumental parameters during ionization which affect trapping would need to be studied for their effect on trapping efficiency. The more important of these parameters, radiofrequency phase angle, radiofrequency amplitude, and buffer gas pressure, are the focus of this chapter.

To perform these experiments, samples were needed which would provide an abundant and steady source of ions over hundreds of laser pulses. Samples which could be shaped in the form of the probe tip can be ablated by the laser with little effect on the ion signal for very many shots. Rods of graphite, stainless steel, and copper were used in these studies without any other preparation.

### Effect of Radiofrequency Phase Angle on Trapping Efficiency

While rf amplitude and buffer gas pressure have been studied previously for ion injection experiments, the phase of the sinusoidal trapping voltage during ion injection has not been investigated; however, the effect of the rf phase at the instant of laser desorption was evaluated experimentally in our laboratory because of the possibility that it may have a significant effect on trapping efficiency for ions produced at the ring electrode surface.

Previously, Kishore and Ghosh<sup>47</sup> and Ghosh *et al.*<sup>48</sup> calculated rf phase dependency in the trapping efficiency for injected ions. In this theoretical study, ions

were injected asymptotically and the optimum initial phase (occurring after a specified delay before the rf field was turned on) was approximately  $180^\circ$ . They calculated the optimum initial phase as that which the ions were stable for hundreds of rf cycles. O and Schuessler also showed a theoretical dependency of injected ions on the rf phase.<sup>49</sup> Their calculations demonstrated that the trapping of externally produced ions (without buffer gas) was possible for a very narrow range of injection phases and that the optimum rf phase angle was dependent on the velocity of the ion. In an analogous study, Pedder *et al.* used an ion trap simulation program, Hyperion, to study the rf phase angle effect on the kinetic energy of electrons entering the trap through the endcap electrode and thus on electron ionization.<sup>50</sup>

In preliminary studies in our laboratory (and in reports by others), the laser trigger was not synchronized with the rf phase. It was observed that the ion signal varied greatly from pulse to pulse. Due to the short laser desorption event (the laser pulse width is 3 ns in our system compared to the 909 ns period of the 1.1 MHz rf), the ion trapping efficiency might be expected to be dependent on the rf phase. The rf phase synchronous triggering circuit described in Chapter 2 can vary the delay time between the rf trigger and the laser trigger from 200 to 1200 ns, thus enabling the study of laser pulse triggering over an entire rf period. In order to perform this experiment, a constant source of sample ions is needed for a large number of laser pulses. Toward this end, a graphite rod was used as the probe tip and ions were produced from its surface. A mass spectrum of graphite from an average of the first

set of 10 laser pulses in the rf phase angle data discussed below is given in Figure 3-1.

During the experiments, ten laser desorption ionization mass spectra were taken at each of 29 different points over approximately  $1\frac{1}{2}$  rf cycles, each point accounting for a phase delay increment of  $20^\circ$  (50 ns). Each set of 10 spectra was averaged to obtain the plots of the  $C_3^+$  ion intensity with respect to rf phase angle, as seen in Figure 3-2a and 3-2b for two separate runs. These plots show patterns of the  $C_3^+$  intensity (displayed as averaged data points and error bars) compared to the pattern of the rf voltage sine wave (displayed by the solid lines). The ion current patterns are seen to decay over the entire period of  $1\frac{1}{2}$  rf cycles which is attributable to a small change in focal length as the sample is ablated from the surface, or to change in surface composition. Continued desorption of ions from the graphite surface, however, showed no overall change in the ion compositions seen in the mass spectra. However, cyclical patterns can be seen which are comparable to the sine wave except that they have slower rises and quicker falls in intensity, and are shifted in phase from the rf field. For the plot shown in Figure 3-2a, the first maximum is seen to occur at an rf phase angle of  $123^\circ$ , shifted from the rf sine wave maximum at  $90^\circ$ . The first minimum is seen to occur at an rf phase angle of  $238^\circ$ , shifted from the sine wave minimum at  $270^\circ$ .

The  $C_3^+$  ion is more intense than the other graphite ions detected using laser desorption ionization (as seen in the mass spectrum in Figure 3-1). However, it is possible in these data to observe a pattern in the  $C_4^+$  and  $C_5^+$  signals which follow

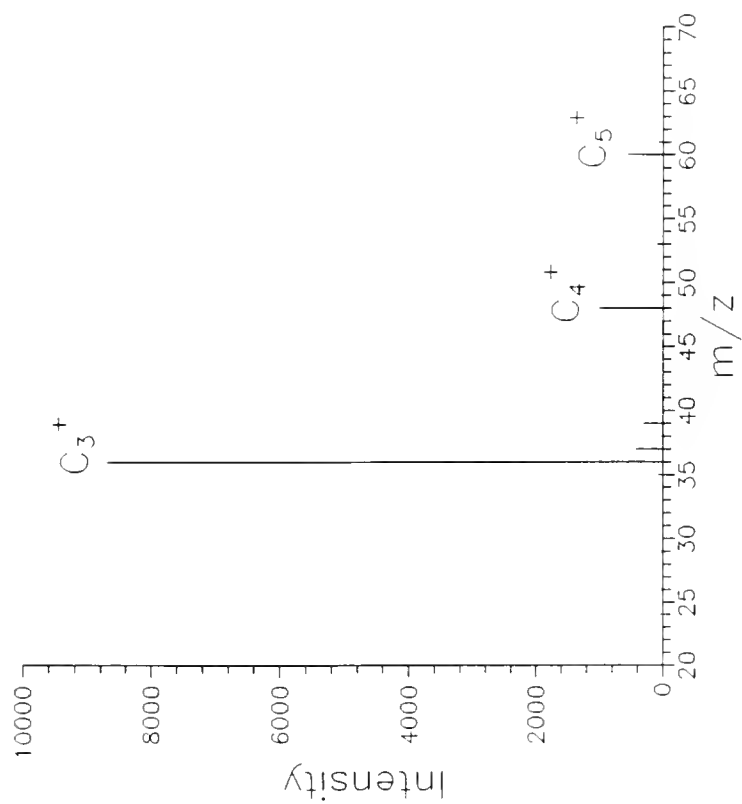


Figure 3-1. Laser desorption ionization mass spectrum of graphite. Average of 10 scans (1 microscan each scan).

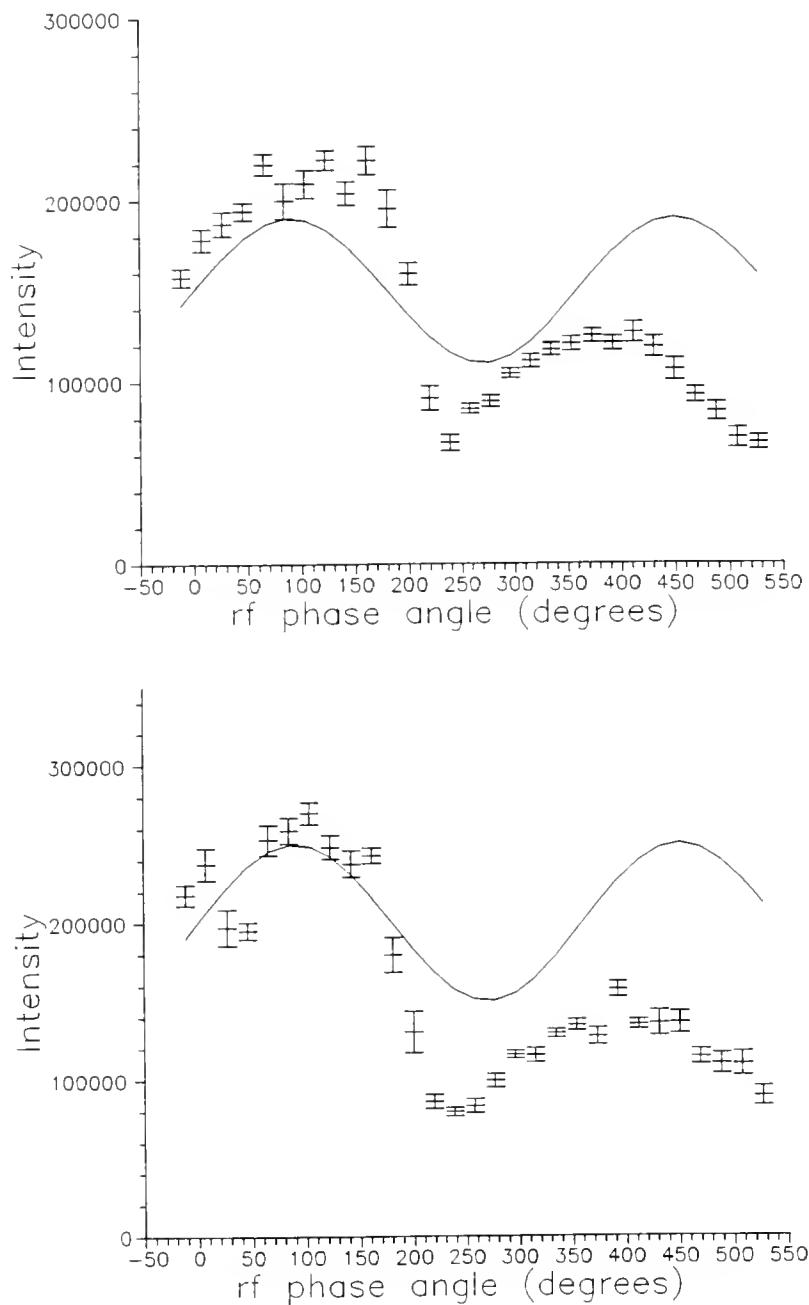


Figure 3-2.  $C_3^+$  intensity and trapping rf amplitude vs. rf phase angle: a) Run 1, b) Run 2. Error bars designate standard error of the mean. Average of 10 scans (1 microscan each scan).

a similar shape to that of the  $C_3^+$ , although each is shifted in phase angle by different amounts, as shown in Figures 3-3 and 3-4, respectively, for two runs. The patterns of these ions are also more sporadic due to their lower signal-to-noise ratio. A comparison of the ions at different masses brings up the question of whether or not this rf phase dependence of the ion trapping efficiency is also mass dependent, thus complicating the matter of determining the optimum point of laser desorption in the rf phase of the ion trap for any given sample.

### Effect of Radiofrequency Amplitude on Trapping Efficiency

Ions stored in the ion trap are subject to a low mass cutoff: ions of  $m/z$  lower than this value have unstable trajectories, while ions of higher  $m/z$  will have stable trajectories in the trap. The low mass cutoff level is directly proportional to the rf voltage applied to the ring electrode. The effect of low mass cutoff on ion trapping efficiency during trapping of laser-desorbed ions was studied. The intensity of laser-desorbed  $^{56}\text{Fe}^+$  ions versus the low mass cutoff during trapping and storage is shown in Figure 3-5. As seen in the plot, the ion intensity varies with the low mass cutoff level, with a maximum occurring at 39.4 u and complete loss of ion storage above 56 u. The maximum ion intensity at the low mass cutoff of 39.4 u is nearly two times greater than that measured at a low mass cutoff of 10 u. Also seen in the plot is a minimum which occurs at a low mass cutoff of 43.2 u. When the data is plotted versus the  $q_z$  for  $m/z$  56, we can see that this minimum occurs at a  $q_z$  equal to 0.69, as shown in Figure 3-6. The loss of trapping efficiency, termed a "black hole," arises

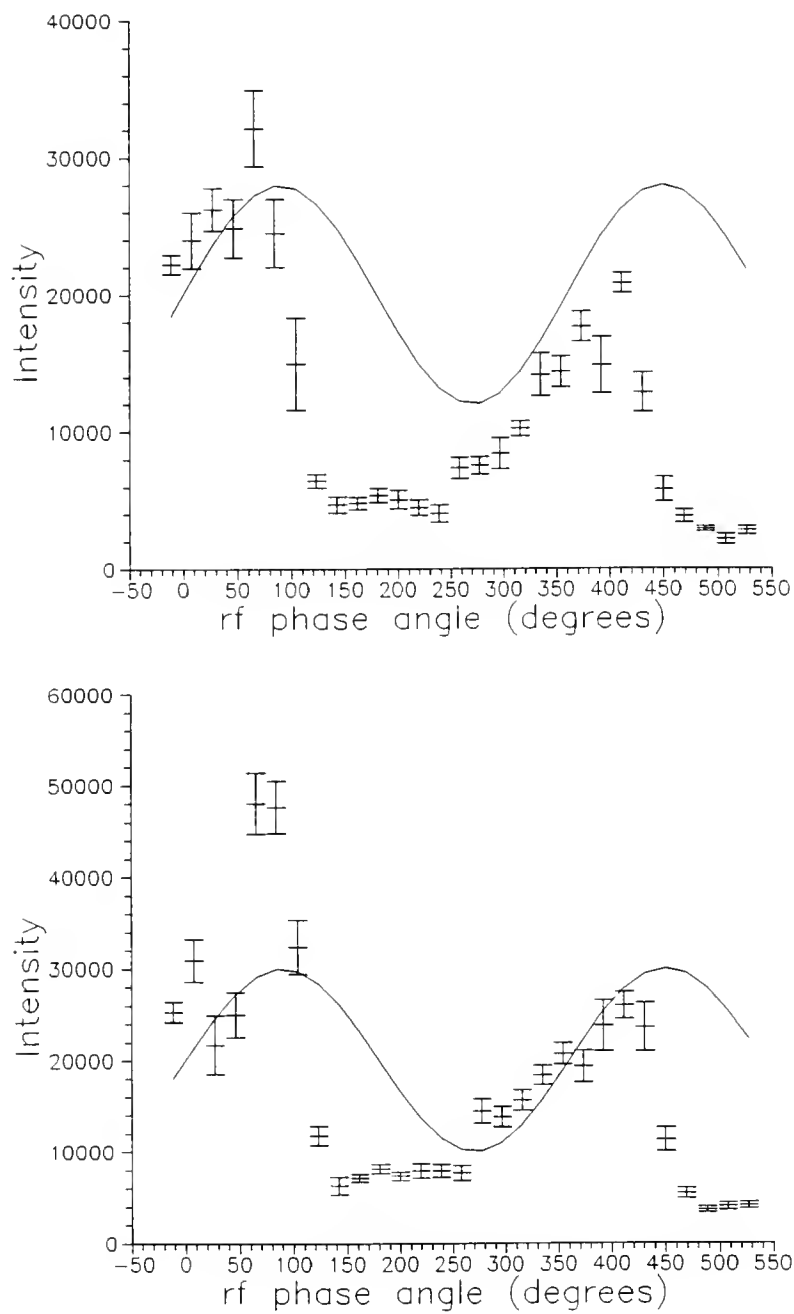


Figure 3-3.  $C_4^+$  intensity and trapping rf amplitude vs. rf phase angle: a) Run 1, b) Run 2. Error bars designate standard error of the mean. Average of 10 scans (1 microscan each scan).



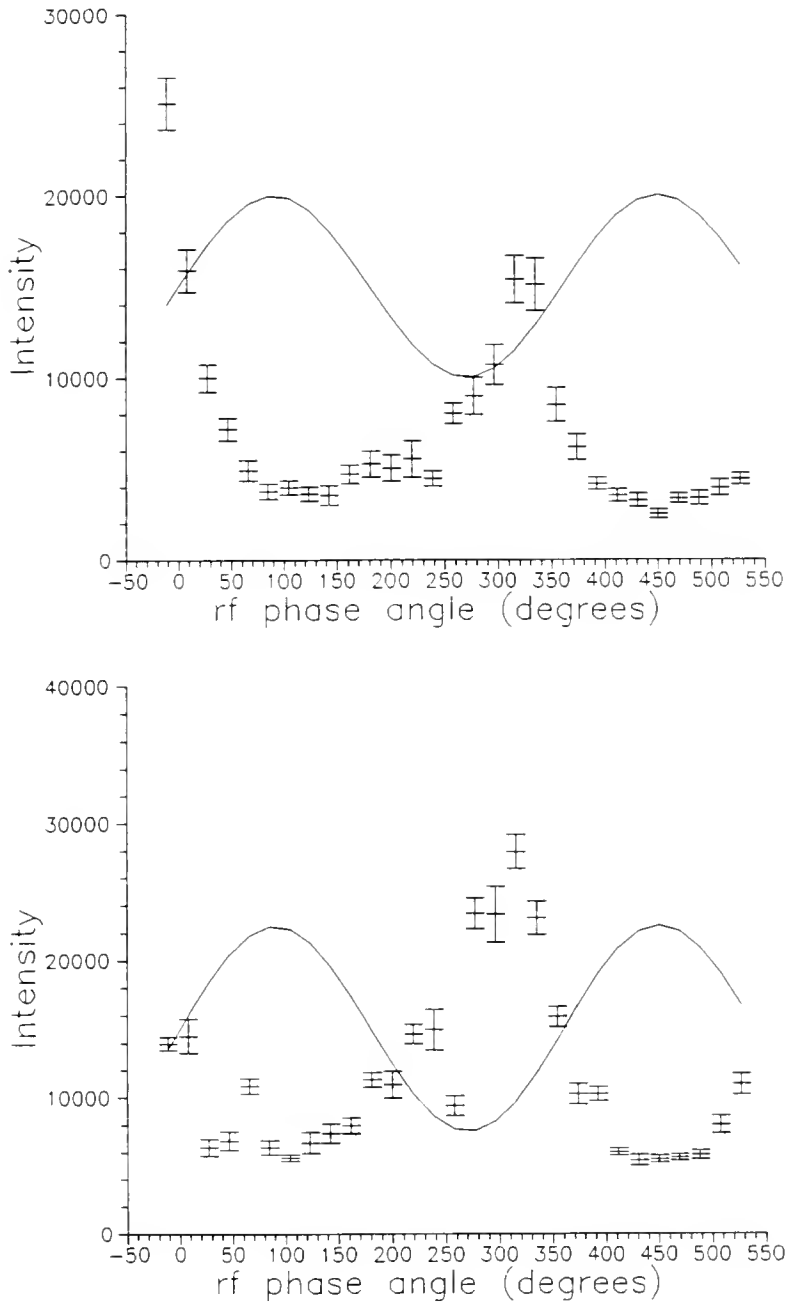


Figure 3-4.  $C_5^+$  intensity and trapping rf amplitude vs. rf phase angle: a) Run 1, b) Run 2. Error bars designate standard error of the mean. Average of 10 scans (1 microscan each scan).

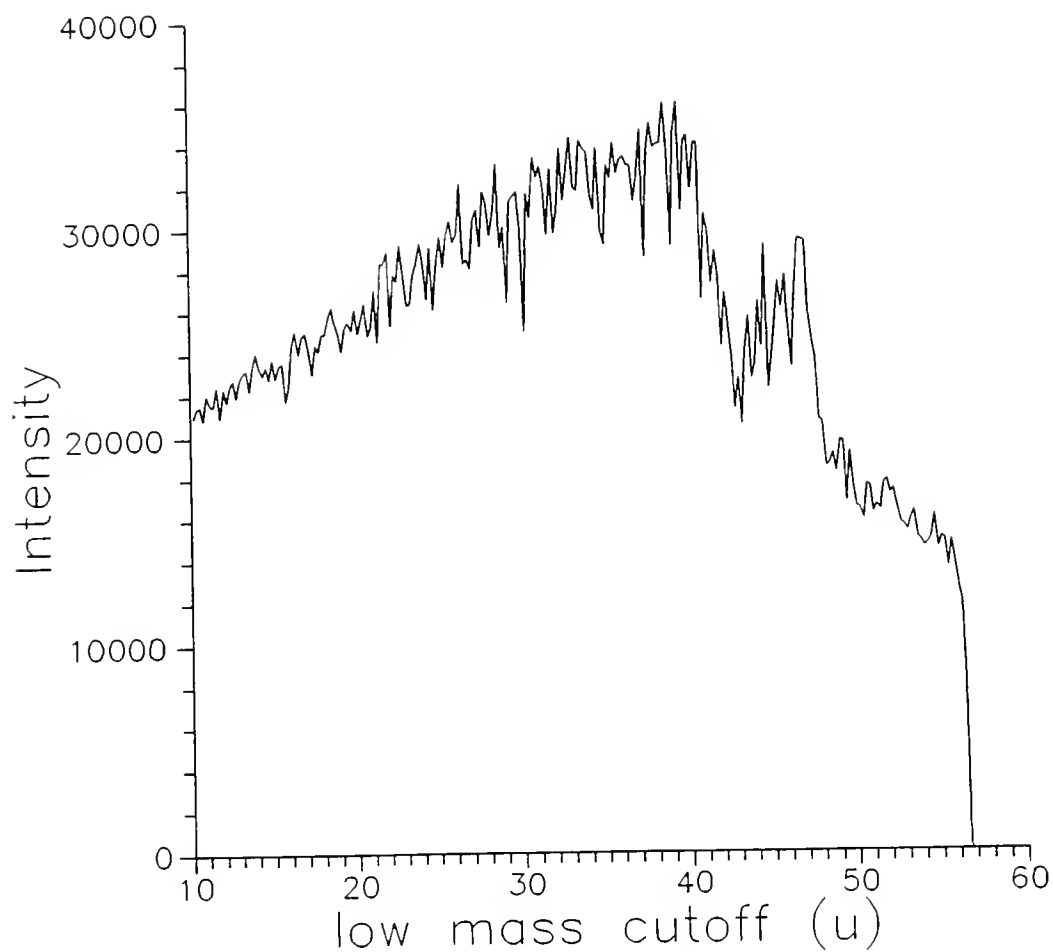


Figure 3-5.  $^{56}\text{Fe}^+$  intensity vs. low mass cutoff. 1 scan each data point (10 microscans each scan).

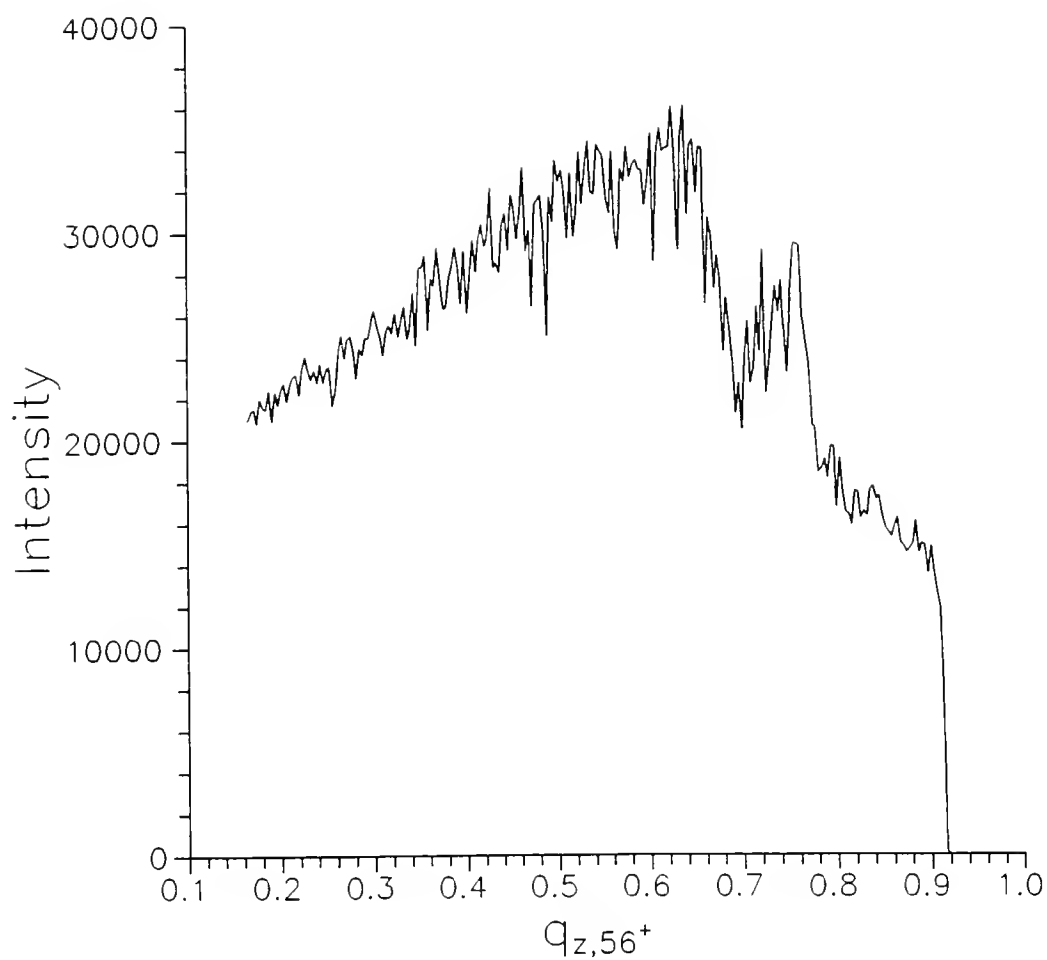


Figure 3-6.  $^{56}\text{Fe}^+$  intensity vs.  $q_z$  for  $m/z$  56. 1 scan each data point (10 microscans each scan).

from octapolar distortions to the quadrupolar trapping field at the stability coordinate ( $a_z, q_z = 0, 0.69$ ) corresponding to a  $\beta_z = 1/2$ ; it has been described theoretically by Wang and Franzen,<sup>51,52</sup> has been seen in chemical ionization and CID experiments as well, and is currently the focus of research in our laboratory and others.<sup>53,54,55</sup> Also shown for comparison in Figures 3-7a and 3-7b are the intensity versus  $q_z$  plots for copper-63 and copper-65 ions, respectively. All three plots show that the ions follow a similar pattern for trapping efficiency for their respective  $q_z$  values during the trapping and storage periods. The maximum ion intensity for all three ions was found to occur at a setting of approximately  $q_z = 0.65$ . In Figures 3-7a and 3-7b for the copper isotope ions, a second minimum is seen to occur which was not clearly evident in the iron data. This second minimum corresponds to a black hole arising from a hexapolar field distortion at  $\beta_z = 2/3$ .

In the data presented here, the  $m/z$  of the ions are quite close, so the effects of intensity versus  $q_z$  are similar and predictable. The effect of rf amplitude on trapping efficiency has been found to be different for laser-desorbed ions of higher  $m/z$ . This effect, however, is possibly not a storage effect but a trapping effect. The trapping (or "acceptance") volume at high rf voltages is very small for ions that are injected,<sup>56</sup> such as ions formed at the ring surface. A similar reason was given to support the data presented in a report by Louris *et al.*<sup>45</sup> Higher mass ions will undergo fewer collisions than lower mass ions because of their lower velocities. High  $m/z$  ions, however, need more collisions to remove kinetic energy because of the larger difference in mass from the collision gas.<sup>45</sup> Also, by increasing the  $q_z$  during

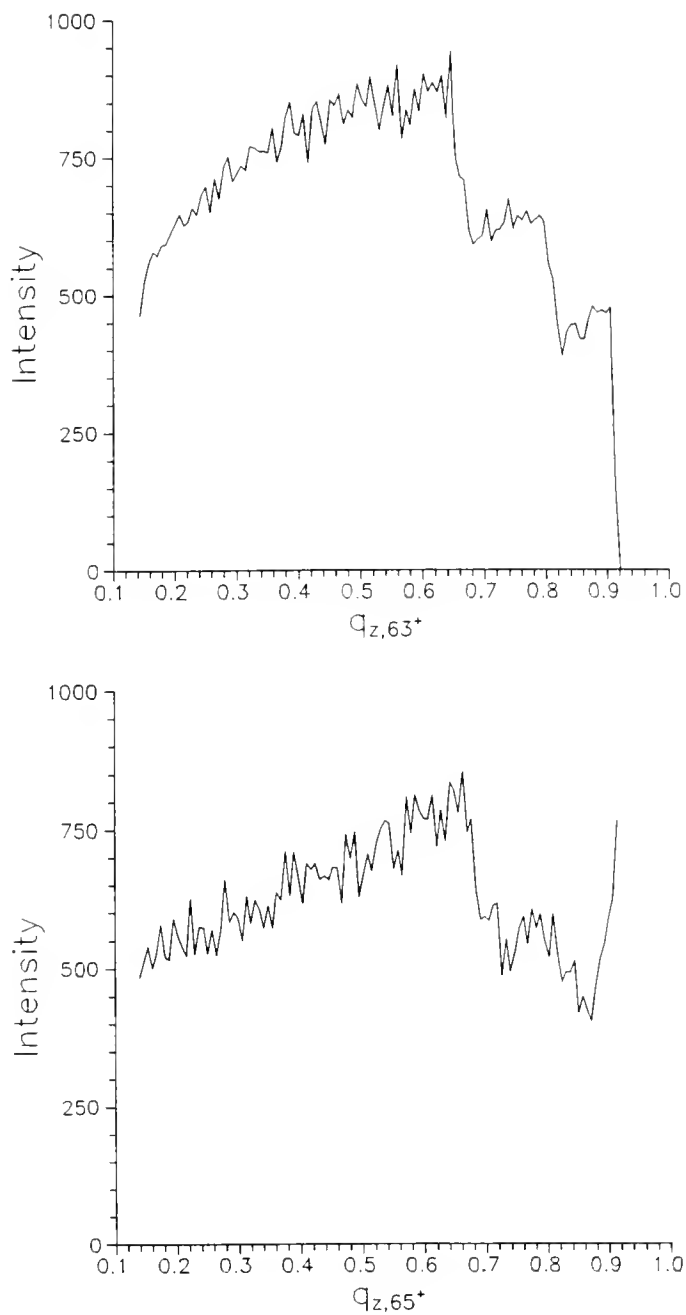


Figure 3-7. Copper isotope ion intensities versus  $q_z$ : a)  $^{63}\text{Cu}^+$  intensity vs.  $q_z$  for  $m/z$  63, b)  $^{65}\text{Cu}^+$  intensity vs.  $q_z$  for  $m/z$  65. 1 scan each data point (5 microscans each data scan).

injection, the higher mass ions will be increasingly unlikely to reach the center of the trap and become stabilized. The combination of these effects probably leads to the observed decrease in trapping efficiency. In fact, very few ions are detected when low mass cutoff levels are above 150 to 200 u in our experiments for detecting ions between 350 u and 600 u. Although laser-desorbed ions of  $m/z$  up to several thousands, have been detected in the ion trap, the low mass cutoff levels were set low and the ions were detected using axial modulation for mass range extension.<sup>57</sup>

### Effect of Buffer Gas Pressure on Trapping Efficiency

The experimental parameter with most significant effect on trapping efficiency is buffer gas pressure. Buffer gas collisionally cools the ions so that they may be trapped once they enter the ion trap volume. After ion trapping has occurred, buffer gas continues to play an important role during ion storage by relaxing the ion motion toward the center of the trap. This process is used to achieve better resolution and sensitivity, as was first discussed by Stafford *et al.*<sup>21</sup> In the case for helium buffer gas, Glish *et al.* showed increased intensity for quaternary ammonium salt ions produced by laser desorption at the ring surface with an increase in pressure.<sup>41</sup> Figure 3-8 shows the effect helium pressure has on the intensity of laser-desorbed iron ions of  $m/z$  56. In this plot, the  $^{56}\text{Fe}^+$  intensity increases rapidly from 0.0025 mtorr to 2.5 mtorr. No ions were detected at the base pressure ( $8 \times 10^{-8}$  torr). To improve the cooling ability of the buffer gas, argon was used instead; the relationship between  $^{56}\text{Fe}^+$  intensity and argon pressure is shown in Figure 3-9. In this figure, the  $^{56}\text{Fe}^+$

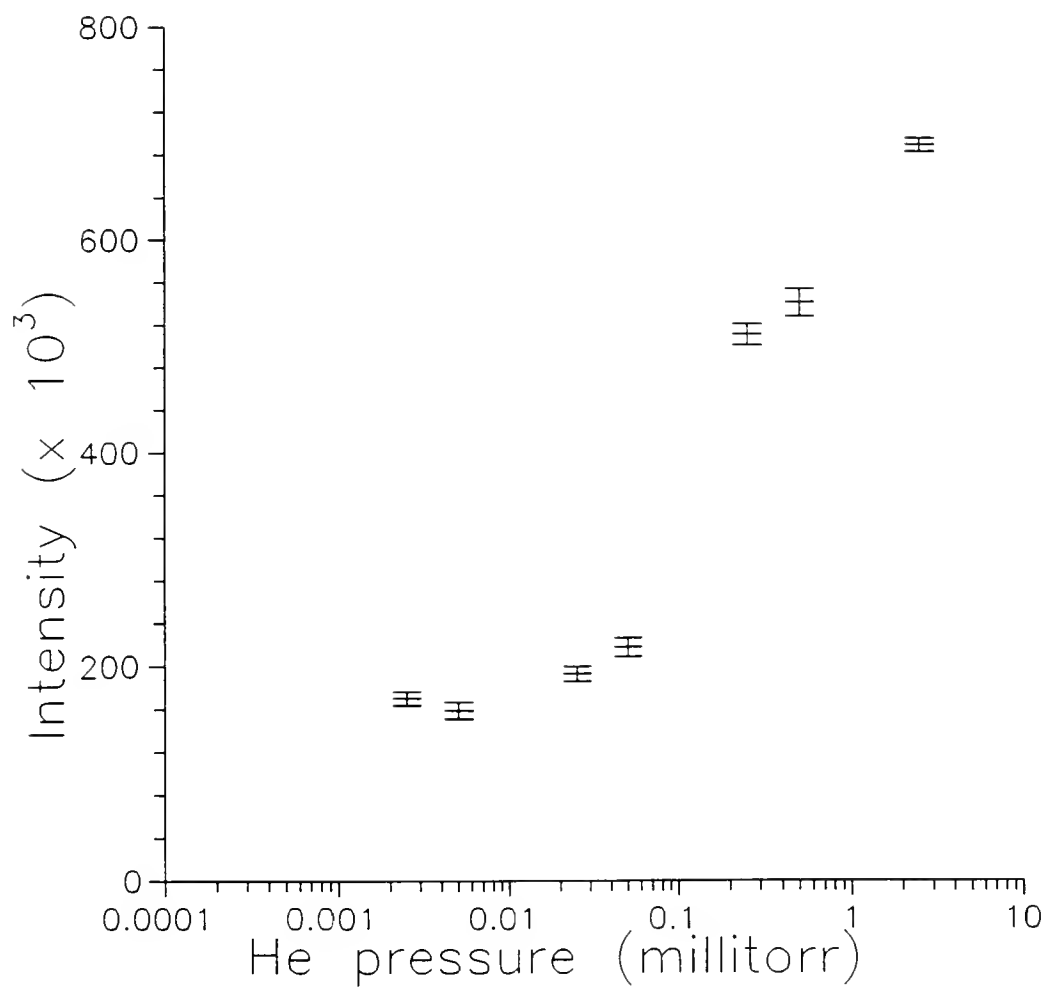


Figure 3-8.  $^{56}\text{Fe}^+$  intensity vs. He buffer gas pressure. Error bars designate standard error of the mean. 50 scans each data point (1 microscan each scan).

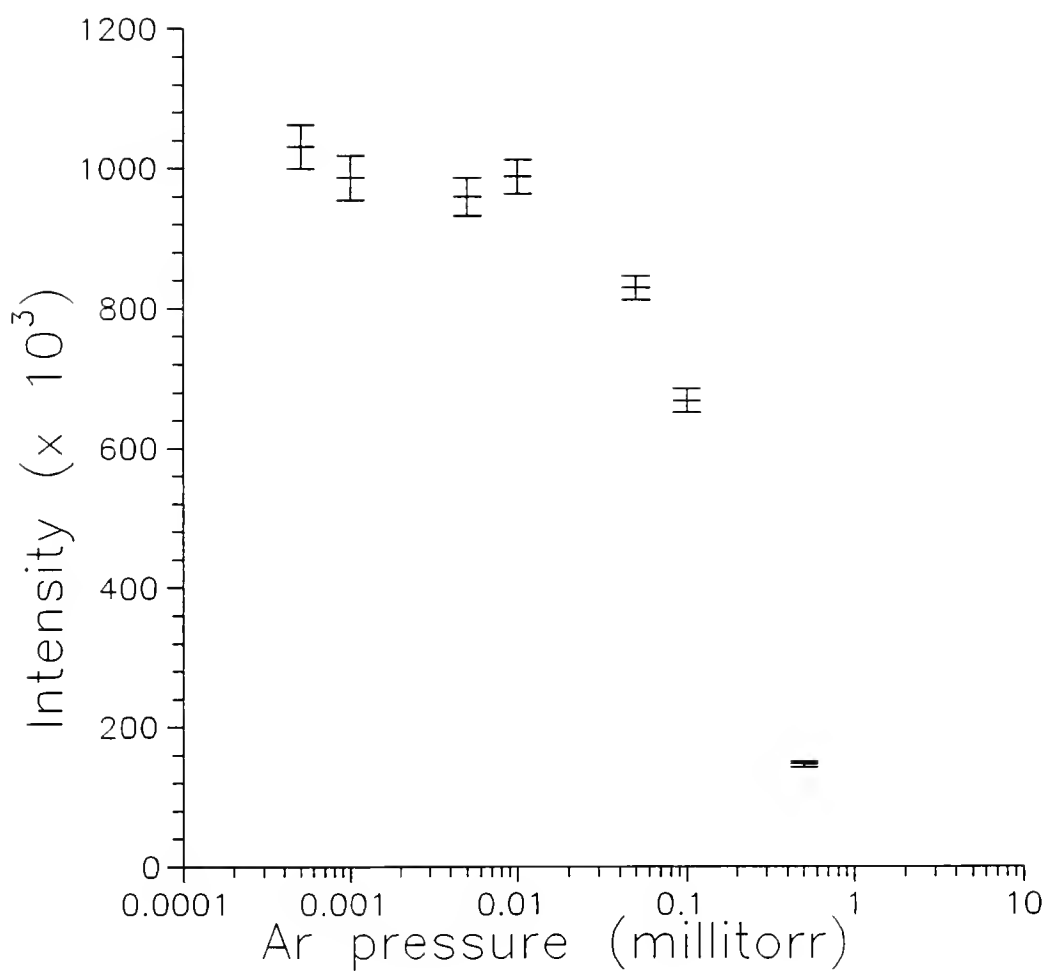


Figure 3-9.  $^{56}\text{Fe}^+$  intensity vs. Ar buffer gas pressure. Error bars designate standard error of the mean. 50 scans each data point (1 microscan each scan).



intensity decreases from 0.0005 mtorr to 0.5 mtorr with a rapid decline beginning at pressure greater than 0.01 mtorr. At the lower pressures, argon, with its much heavier mass than helium, removes kinetic energy from the ions more efficiently per collision than helium. A combination of scattering losses and ion peak reduction due to peak spreading (loss of mass resolution) explains the signal decay.

The observations made of the buffer gas pressure effect on ions produced at the ring surface are similar to those seen in a study of injection of gold ions through the endcap electrode from an external source.<sup>45</sup> Helium, neon, argon and xenon buffer gases all promoted ion trapping. Neon was found similar to helium in promoting trapping, but argon and xenon yielded signals only 10-20% as intense as helium. Xenon produced broad peaks in the mass spectrum whereas the other three gases produced peaks of unit resolution.

The results obtained using a copper sample show the expected increase in  $^{63}\text{Cu}^+$  and  $^{65}\text{Cu}^+$  intensity with increasing helium pressure, as seen in Figures 3-10a and 3-10b, respectively. It is important to note, however, that the isotope ratio in these measurements deviate from the expected natural abundance ratio of 2.3 ( $^{63}\text{Cu}/^{65}\text{Cu}$ ). Figure 3-11 shows a plot of  $^{63}\text{Cu}^+ / ^{65}\text{Cu}^+$  intensity ratio. The ratio increases from approximately 0.4 to 2.1 from 0.0025 mtorr to 2.5 mtorr helium. The appearance of the incorrect isotope ratio at the lower pressures is not completely understood. While ion abundance is maintained below the onset of space charge conditions, the apparent loss of  $^{63}\text{Cu}^+$  (or gain of  $^{65}\text{Cu}^+$ ) is unexpected. No other ions were seen in the spectra suggesting that no side reactions were taking place.

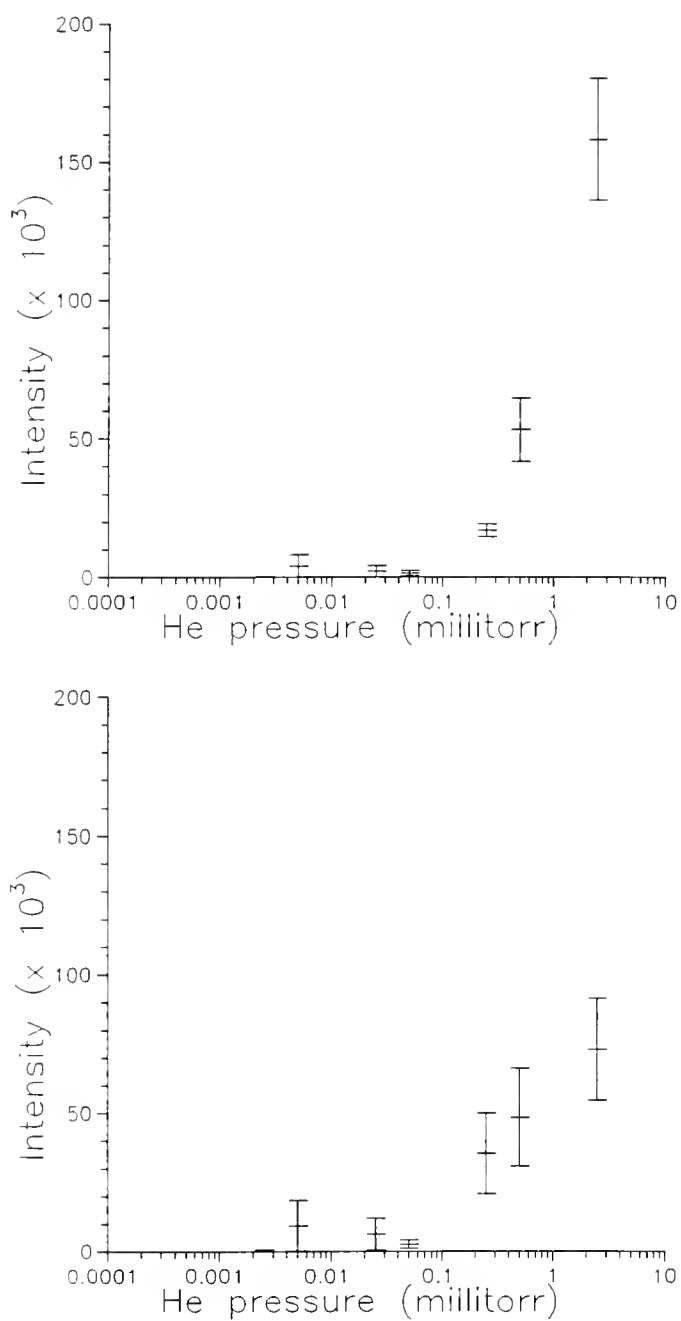


Figure 3-10. Copper isotope ion intensities vs. helium buffer gas pressure: a)  $^{63}\text{Cu}^+$  intensity vs. He pressure, b)  $^{65}\text{Cu}^+$  intensities vs. He pressure. Error bars designate standard error of the mean. 50 scans each data point (1 microscan each scan).

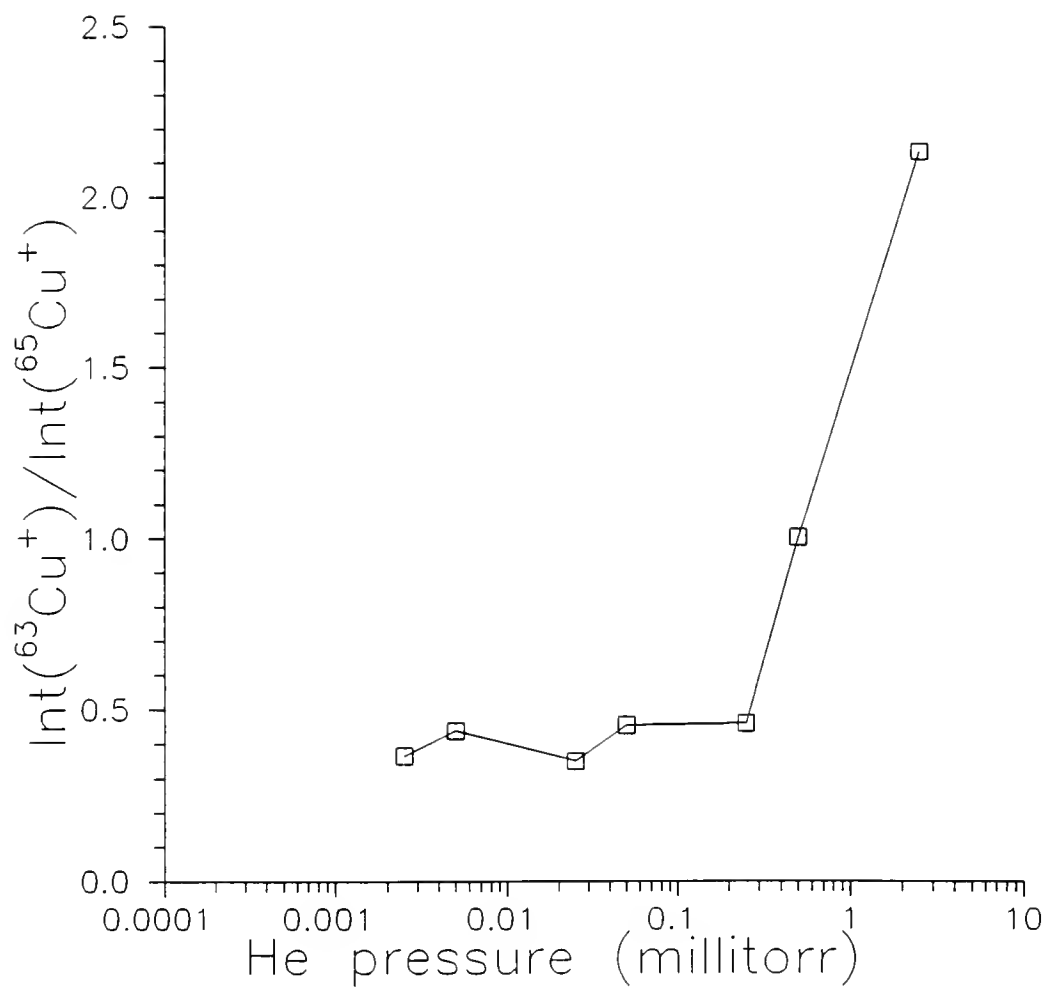


Figure 3-11.  $^{63}\text{Cu}^+ / ^{65}\text{Cu}^+$  isotope ratio vs. He buffer gas pressure. 50 scans each data point (1 microscan each scan).

And it is doubtful that the incorrect ratio is due to the sample or ionization process. In the use of a stainless steel probe tip to make iron ions, the calculated isotope ratios for observed iron isotopes, chromium isotopes, and nickel isotopes were all found to be correct.

The use of argon buffer gas was also studied with the copper isotopes. Figures 3-12a and 3-12b show the intensity versus argon pressure plot for  $^{63}\text{Cu}^+$  and  $^{65}\text{Cu}^+$ . The data are similar to those seen for  $^{56}\text{Fe}^+$  in Figure 3-9 in that there is a decrease in ion intensity at the high end of the pressure range. In the plots of copper intensities versus argon pressure, however, a reduction in ion intensity is also seen at the high end of the pressure range creating maximum intensities at 0.025 mtorr for both isotopes.

A plot of the copper isotope intensity ratio versus argon pressure gives the results in Figure 3-13. The copper isotope ratio varied 0.6 to 1.3 over the measured argon pressure range from 0.0005 mtorr to 0.5 mtorr. Although the isotope ratio increased with increasing argon pressure, the ratio never reached the natural abundance ratio of 2.3.

### Conclusions

Efficient trapping of ions produced by laser desorption ionization at the ring electrode surface requires careful control of rf phase angle, rf amplitude, and buffer gas pressure. The trapping efficiency of laser-desorbed graphite ions was found to be dependent on the rf phase angle during the laser desorption event. A cyclical

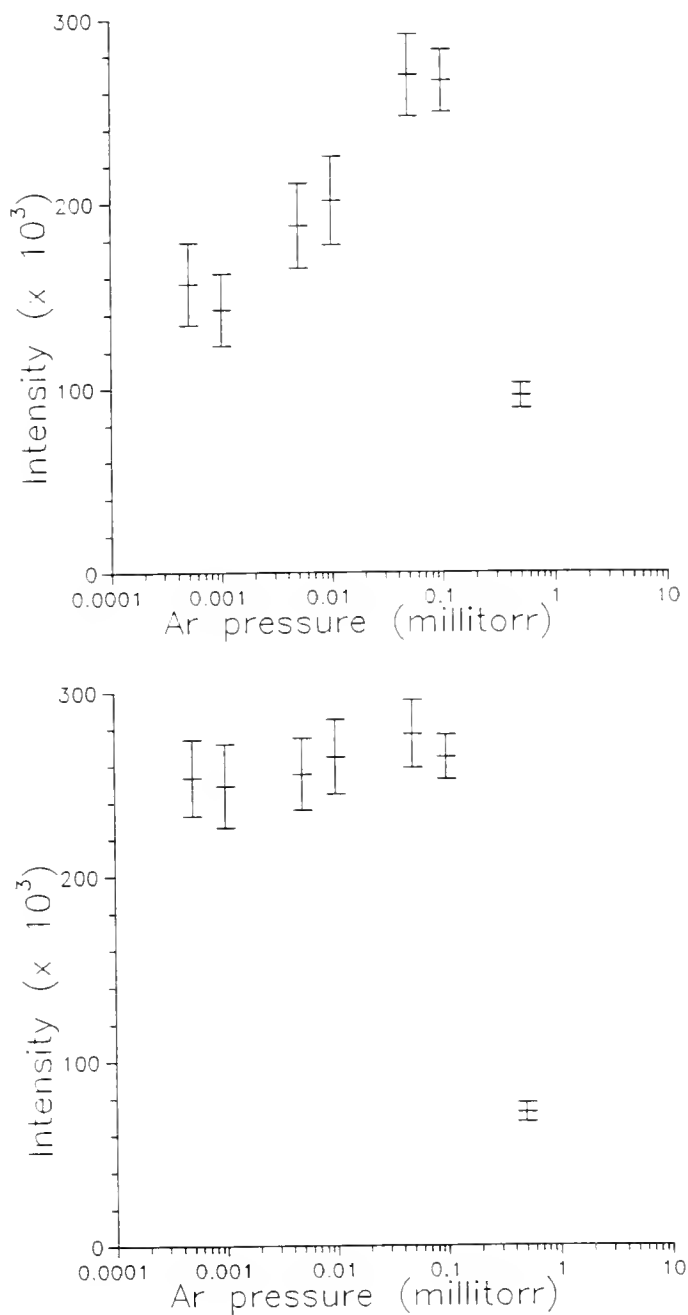


Figure 3-12. Copper isotope ion intensities versus argon buffer gas pressure: a)  $^{63}\text{Cu}^+$  intensity vs. Ar pressure, b)  $^{65}\text{Cu}^+$  intensities vs. Ar pressure. Error bars designate standard error of the mean. 50 scans each data point (1 microscan each scan).

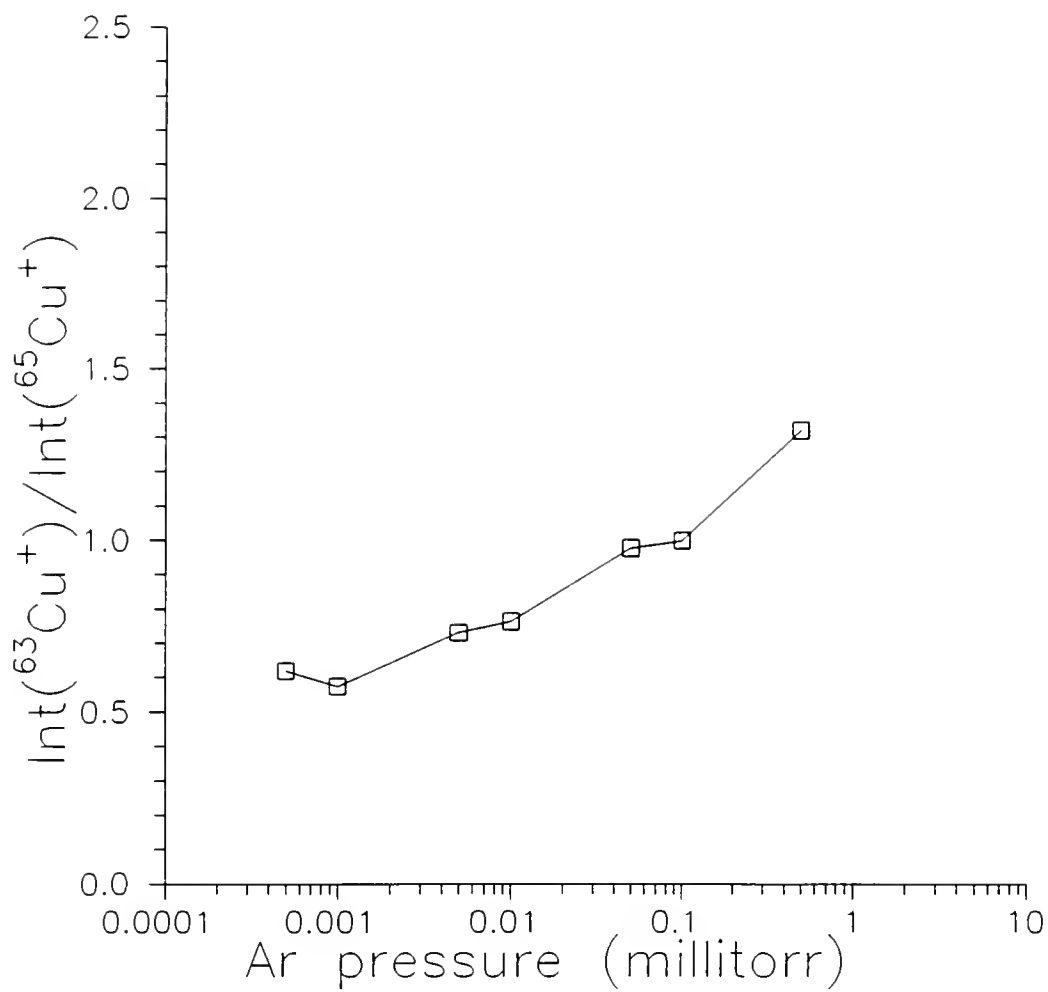


Figure 3-13.  $^{63}\text{Cu}^+ / ^{65}\text{Cu}^+$  isotope ratio vs. Ar buffer gas pressure.

pattern was seen in the intensity of  $C_3^+$  which is comparable to the rf voltage sine wave except that it has a slower rise and quicker fall in intensity, and is shifted in phase from the rf field.  $C_4^+$  and  $C_5^+$  signals were also found to be dependent on rf phase angle with different patterns over the measured rf phase angle range. The results from the different ions suggest that the rf phase dependence of the trapping efficiency is also mass dependent, thus complicating the matter of determining the optimum point of laser desorption in the rf phase of the ion trap for any given sample.

The rf voltage was found to have a similar effect on the intensities of  $^{56}\text{Fe}^+$ ,  $^{63}\text{Cu}^+$ , and  $^{65}\text{Cu}^+$ . Also, minima in the ion intensities demonstrated the appearance of black holes in the ion trapping efficiency when the data was plotted versus  $q_z$ . The maximum intensities measured were approximately twice as large as the lowest measured low mass cutoff value and found to occur at coinciding  $q_z$  values of 0.65.

Buffer gas pressure was found to have the most significant effect on trapping efficiency of all of the instrumental parameters studied. No ions were detected at the base pressure. With helium buffer gas,  $^{56}\text{Fe}^+$  intensity increased rapidly from 0.005 mtorr to 5 mtorr. With argon buffer gas,  $^{56}\text{Fe}^+$  intensity decreased from 0.0005 mtorr to 0.5 mtorr, most likely caused by a combination of scattering losses and loss of resolution (peak spreading and height reduction). Results obtained here were similar to those in other reports using laser-desorbed ions and ion injection systems on the quadrupole ion trap.

Copper ion results were similar to those obtained using iron for helium and argon buffer gas. The isotope ratio of the copper ions, however, was found to vary over the measured buffer gas ranges and deviate from the natural abundance ratio.

The observations made here of the effects of these instrumental parameters are in general more similar to those that would be obtained performing ion injection from an external source than ionization inside the ion volume (e.g. conventional EI and CI on the trap). These observations suggests that in order to obtain the best trapping efficiency using this configuration, the effect of rf phase angle and rf amplitude need to be determined on the sample of interest; the buffer gas pressure in the case of helium should be set to its highest possible pressure (e.g. before the onset of space charge or arcing). At optimum rf phase angle and rf amplitude, the ion intensities in this study doubled in both cases. For the helium buffer gas pressure study, the  $^{56}\text{Fe}^+$  intensity varied by a factor of 4 from the lowest helium pressure to the highest pressure. For  $^{63}\text{Cu}^+$  and  $^{65}\text{Cu}^+$ , the intensities varied by a factor of approximately 800 and 136 over the same pressure range for helium, respectively.



## CHAPTER 4

### LASER DESORPTION IONIZATION/QUADRUPOLE ION TRAP MASS SPECTROMETRY USING AN INTERNAL SOURCE CONFIGURATION

#### Laser Desorption Ionization

Whereas the previous chapter dealt with the fundamentals of trapping laser-desorbed ions formed at the ring electrode surface, this chapter presents research performed to evaluate the combination of the capabilities of laser desorption with the capabilities of the quadrupole ion trap mass spectrometer. An abundant number of ions over many laser pulses can be obtained with laser desorption ionization on organic salts. Therefore, to initially evaluate tandem mass spectrometry of laser-desorbed ions in the ion trap, laser desorption ionization was performed on trimethylphenylammonium bromide.

#### MS/MS of Trimethylphenylammonium Bromide

Using a five microliter syringe, 4  $\mu\text{L}$  of a 5 mM solution of trimethylphenylammonium bromide (TMPA) in methanol was placed on the stainless steel probe tip and dried in air. The probe tip was placed inside the ring electrode and the sample surface positioned flush with the ring surface. The results obtained from laser desorption ionization (LDI) of TMPA are given in Figures 4-1 and 4-2. In Figure 4-1a, the laser desorption mass spectrum of TMPA using a full mass scan

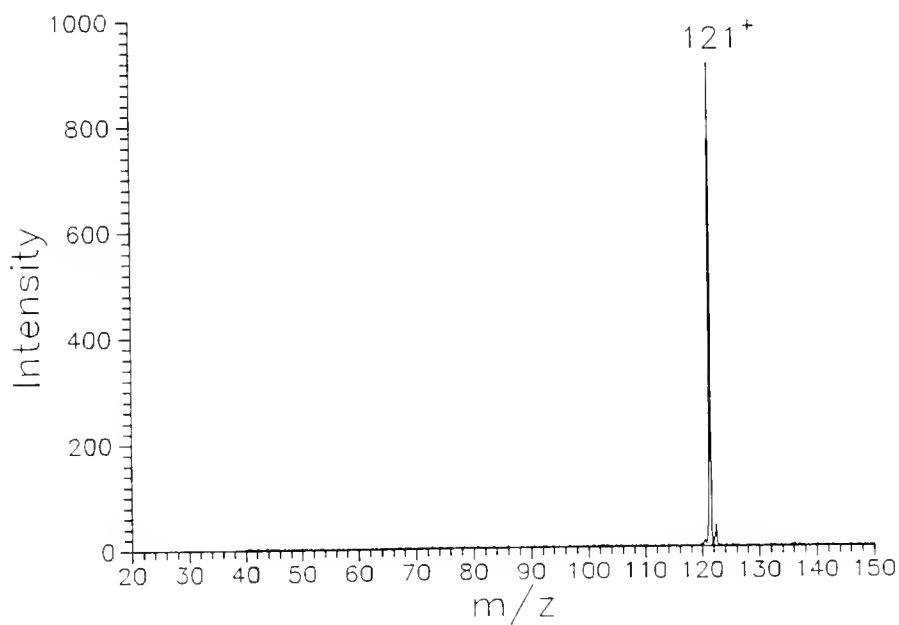
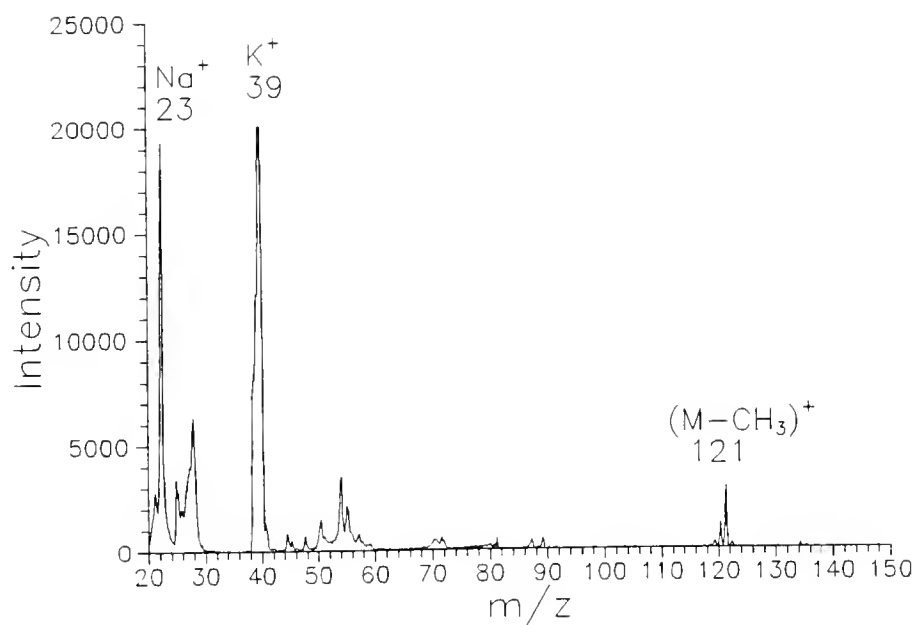


Figure 4-1. Laser desorption ionization mass spectra of trimethylphenylammonium bromide, a) full mass scan, b) single ion isolation of the  $121^+$  fragment ion.

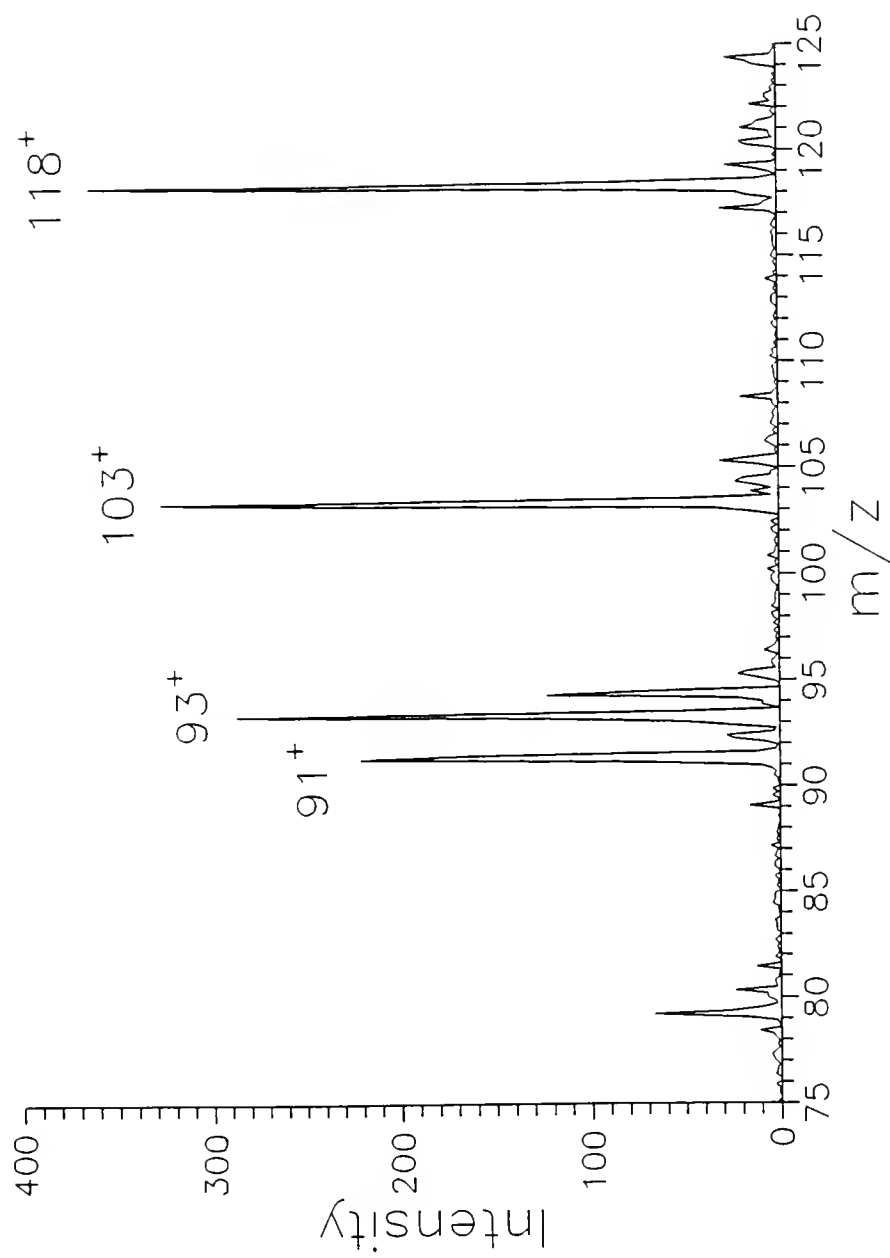


Figure 4-2. LDI/MS/MS of 121<sup>+</sup> ion of trimethylphenylammonium bromide.

from 20 to 640 u is shown. In this spectrum, the displayed data from  $m/z$  20 to 150 show two large and unresolved peaks at the low mass end due to highly abundant sodium and potassium ions. These ions are typical LDI products observed most often in the mass spectra of unpurified organic compounds and biological samples. We also see a set of unresolved peaks between 50 and 60 u due to the stainless steel probe tip background. The peaks are comprised of the various isotopes of iron, chromium, and nickel. Under different conditions for LDI, each of these ions were fully resolved for study. The interest here, however, is in any ions obtained from the TMPA sample. There is an extremely small peak at  $m/z$  136 for the molecular ion, but the ion used for the following analysis is the one found at  $m/z$  121 which is a fragment of TMPA. This ion is formed by the loss of a methyl group from the trimethylphenylammonium cation (a preformed ion). Using a two-step ion isolation routine developed in our lab by Nathan Yates, this TMPA fragment ion can be isolated by ejecting all of the other ions from the trap.

Performing this isolation step and taking a mass scan gives the mass spectrum shown in Figure 4-1b. In this spectrum, the only major peak is that for the TMPA fragment ion at  $m/z$  121. A few smaller peaks at  $m/z$  120 and 122 are due to incomplete ion isolation, but they are less than 5% of the intensity of  $m/z$  121 ion. The efficiency of the single ion isolation displayed in Figures 1a and 1b is only about 33%, but it must be noted that isolation step involved ejecting more of  $m/z$  121 ion than was really necessary. Typically, isolation is performed to maintain as much of the ion of interest as possible in the ion trap with surrounding ions (in this case at

m/z 120 and 122) having a relative intensity much greater than in this experiment, usually up to 10%.

A collision-induced dissociation (CID) step was then added to the scan function after the ion isolation step. During the CID process, the m/z 121 ion is resonantly excited causing the ions to obtain larger and more energetic trajectories. The additional collisions with helium buffer gas induce the ions to fragment and the ions produced can then be stored if their trajectories are stable in the ion trap. A mass scan of these "daughter" ions are shown in Figure 4-2. This daughter ion spectrum shows several peaks which can be identified by the amount of mass lost. The peaks noted in the figure are m/z 118 which has the composition  $\text{C}(\text{CH}_3)\text{N}-\phi^+$ , m/z 103 which is  $\text{CN}-\phi^+$ , m/z 93 which is  $\text{H}_2\text{N}-\phi^+$ , and m/z 91 which is  $\text{N}-\phi^+$ .

It is important to note in this mass spectrum, and in all of the spectra shown later, that the method of assigning peaks to the mass axis is different on the ITMS from most other mass spectrometers. With the ITMS, the peak for m/z 118 should be found to the right of the hatch mark signifying 118 and to the left of the hatch mark signifying 119. The center of the peak, therefore, is placed in the center of the space between these two hatch marks. This convention is used for all of the data obtained from the ITMS and ITS40 instruments and will be noticeable where the hatch marks in the mass spectra represent a single mass unit.

A combination of factors determines the efficiency with which CID is performed in the ion trap, an efficiency usually described as the conversion of parent ion to daughter ions. With all of the instrumental parameters optimized (including

buffer gas pressure, resonant excitation frequency and voltage, and low mass cutoff), the most important determinant is the compound itself and its ability to be fragmented with the obtainable collision energies in the trap. The CID efficiency for the mass spectrum shown in Figure 4-2 was not optimized, but yet the appearance of several different fragment ions was the desired result of this experiment. These data show that tandem mass spectrometry can be performed on laser-desorbed ions in the ion trap, and the results obtained can be used to identify ions which are not the most abundant products of the laser desorption process.

### Positive and Negative Ion Spectra

As stated in the introduction, laser desorption ionization can produce a wide range of particles including both positive and negative ions. The quadrupole ion trap can also store both positive and negative species; the method of detection presumably allows only one polarity to be detected at a time. Figures 4-3a and 4-3b show the positive and negative ion spectra for sodium iodide, respectively. In order to obtain the positive ion spectrum, a negative voltage (-4 kV) was applied to the conversion dynode to attract positive ion species toward it. In this mass spectrum, we see peaks at  $m/z$  127 ( $I^+$ , shifted on the mass axis due to space charge), and sodium iodide cluster peaks at  $m/z$  173 ( $Na_2I^+$ , also shifted on the mass axis due to space charge),  $m/z$  277 ( $NaI_2^+$ ), and  $m/z$  323 ( $Na_3I_2^+$ ).

In order to obtain the mass spectrum shown in Figure 4-3b, a positive voltage (+4 kV) was applied to the conversion dynode to attract negative ions toward it.

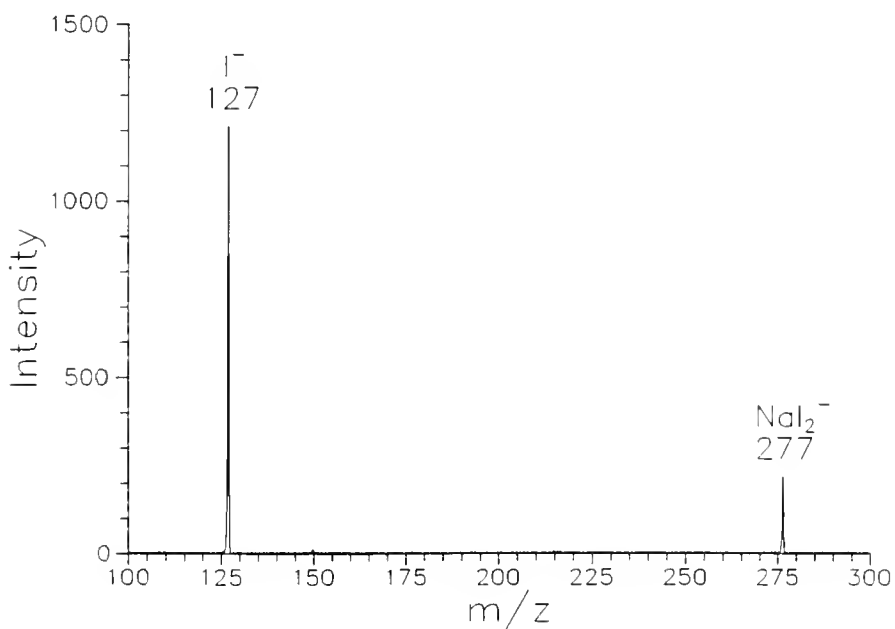
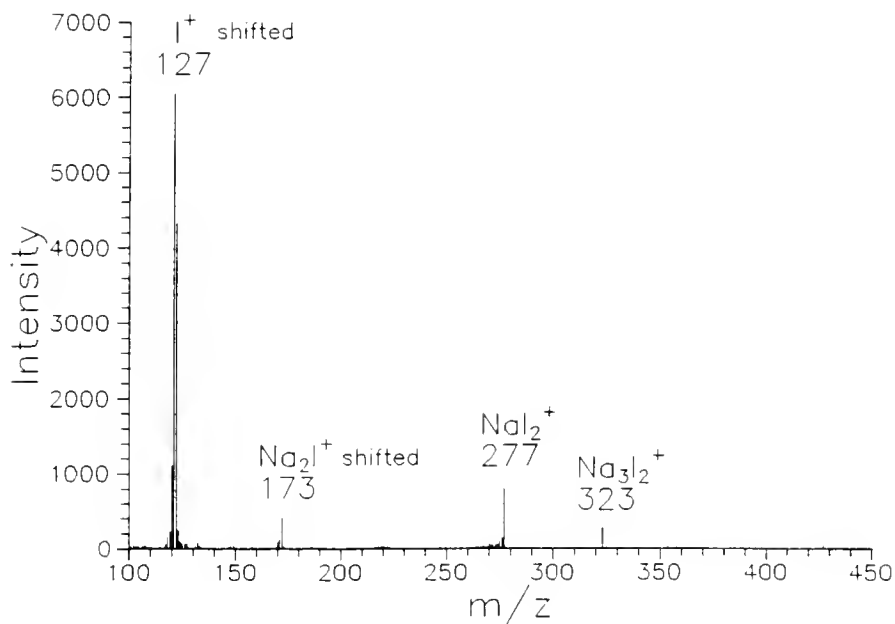


Figure 4-3. LDI/MS of sodium ions, a) positive (average of 5 scans, 20 microscans each scan), b) negative ion spectra. Several peaks are shifted to the right due to space charging (a) or calibration error (b).

Two peaks are seen in this mass spectrum at  $m/z$  127 for the  $I^-$  ion and  $m/z$  277 for the  $NaI_2^+$  ion. In both experiments, the ions hit the conversion dynode and any emitted negative particles were attracted to the more positively charged electron multiplier for detection. The opposite charged species may appear as artifacts in the mass spectra (e.g., a negative ion may hit the detector although the voltage settings make it highly unfavorable), but trapping conditions may be altered to remove these ions.<sup>58</sup>

### Matrix Compounds

Of the different compounds studied using laser desorption ionization in the ion trap mass spectrometer, the UV absorbing matrices were expected to give good ion signals due to their strong energy absorbance characteristics at the nitrogen laser wavelength as discussed in Chapter 2. LDI mass spectra were obtained for the various matrix compounds used so that ions which are produced in the MALDI experiments could be attributed to either the analyte or the matrix compound. The matrices used were methanol solutions of sinapinic acid, nicotinic acid, 2,4-dinitroaniline, coumarin-120, and 2,5-dihydroxybenzoic acid. Of these compounds, the ones which were used consistently were sinapinic acid and 2,5-dihydroxybenzoic acid. These matrices were observed to give the desired MALDI results in our laboratory. Reports in the literature also showed these matrices to be the most popular due to their universal applicability and uniform MALDI spectra.



The LDI mass spectrum for 2,5-dihydroxybenzoic acid (DHB) is given in Figure 4-4. In this spectrum, the largest peaks observed are at  $m/z$  ratios of 136, 137, and 153 (the masses are off the axis assignment by about 0.5 u). These fragment ion peaks are attributable to a loss of a hydrogen ( $m/z$  153), a loss of a hydroxyl group ( $m/z$  137), and a loss of water ( $m/z$  136). All of these fragment ions were easily assigned and the mass spectrum is typical of those obtained using laser desorption ionization. No ions are seen for the molecule at  $m/z$  154. The characteristics of the LDI mass spectrum are similar to spectra obtained performing electron ionization (EI) on gaseous samples. It is noted then for future reference when performing matrix-assisted laser desorption ionization using a DHB matrix solution that these ions may appear in the mass range below 154 u.

Another compound which was observed to work well in preliminary experiments performed in our laboratory was 2,4-dinitroaniline (2,4-DNA). The LDI mass spectrum for 2,4-DNA is given in Figure 4-5. In this mass spectrum, we observe the protonated molecular ion peak,  $(M+H)^+$ , for 2,4-DNA at  $m/z$  184 that may have been produced by self chemical ionization. We also detect peaks at  $m/z$  167 for  $[M-NH_2]^+$ ,  $m/z$  154 for  $[M+H-NO]^+$ ,  $m/z$  136 for  $[M-HNO_2]^+$ ,  $m/z$  123 for  $[M-N_2O_2]^+$ , and  $m/z$  89 for  $[C_6H_3N]^+$ . A peak is seen at  $m/z$  39 for potassium and at  $m/z$  24 for sodium shifted to the right by 1 mass unit.

The mass spectrum for 2,4-DNA given in Figure 4-5 is the 33rd scan performed in this experiment. The relationship of several of the ions in the mass spectra over the first 50 scans is shown in Figure 4-6. In this plot of ion intensities

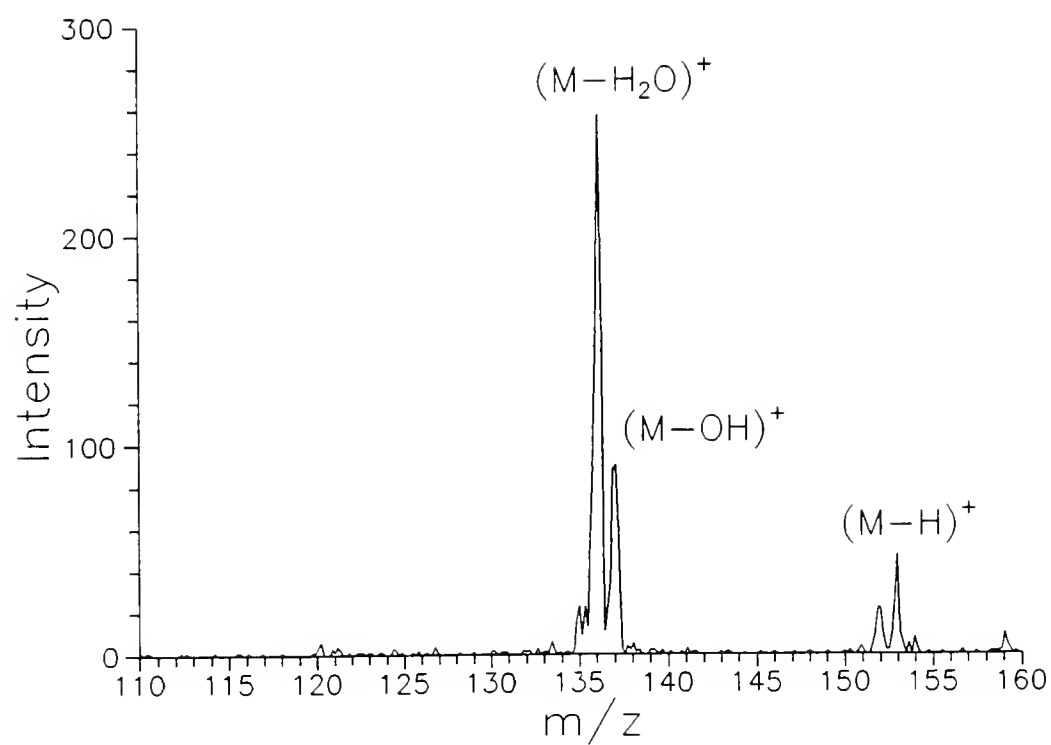


Figure 4-4. LDI/MS of 2,5-dihydroxybenzoic acid.

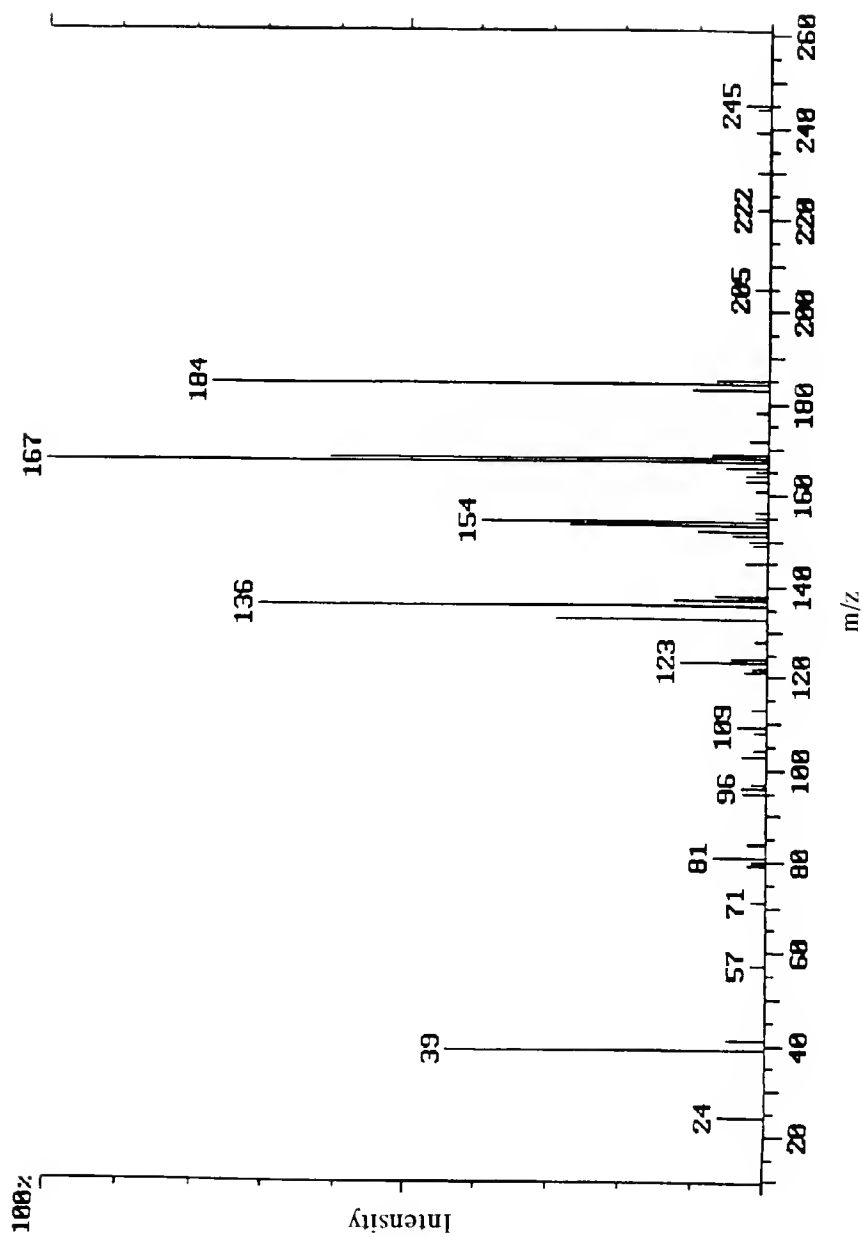


Figure 4-5. LDI/MS of 10  $\mu\text{g}$  of 2,4-dinitroaniline (MW 183) deposited on the probe tip (1 microscan).

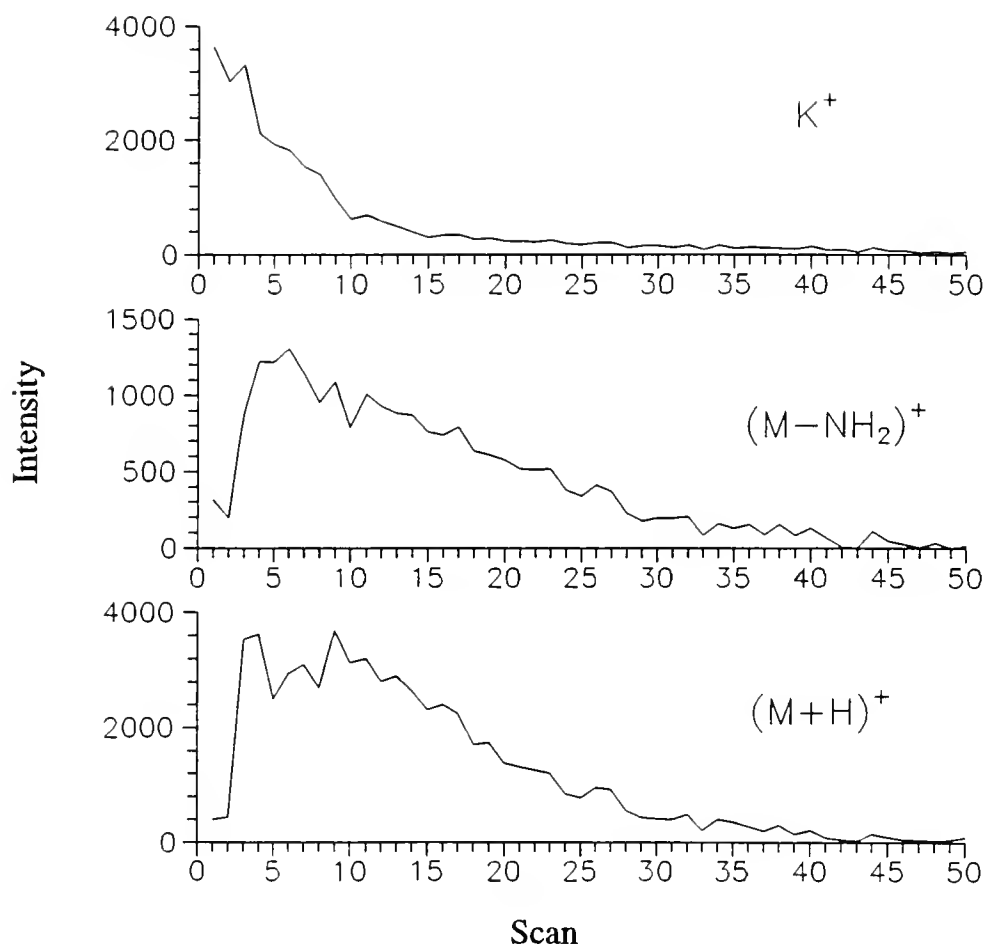


Figure 4-6. Mass chromatograms from LDI/MS of 10  $\mu$ g of 2,4-dinitroaniline (MW 183). 1 microscan each scan.

versus scan, the potassium ion intensity is seen to begin at a maximum intensity and decrease over 50 scans. Each scan represents a single laser pulse followed by a mass scan (e.g., no scan averaging). The intensities for 2,4-DNA ions at  $m/z$  164 and  $m/z$  184 are seen to increase from nearly from 10% of their maximum intensity to 100% after the first two pulses. The ion intensities then decrease from that maximum over the following 45 scans. Between scans 10 through 50, however, the 2,4-DNA ions are greater in intensity than the potassium ions. This relationship is typical of many of the experiments performed using LDI in our laboratory. The first few laser shots may contain a large number of alkali metal ions, the sample ions dominate the spectra after several shots, and the overall sample ion intensities decay over multiple laser shots. The first few mass spectra also tend to be greatly space charged as the initial layers of sample material are removed. The space charge can occur because either there is a higher abundance of preformed alkali metal ions at the sample top layers which are efficiently desorbed by the laser and greatly increase the ion number, or the combination of fresh sample material, alkali metal ions, and laser irradiance setting produces a large number of sample and alkali ions producing space charge conditions. Therefore, to obtain the best mass spectra of resolved sample ions in this situation, a later mass scan can be used such as scan #33 in this experimental series as was given in Figure 4-5. The occurrence of space charge conditions causing the loss of mass resolution was also observed by Gill and Blades for LDI/MS of both organic and inorganic samples under varying conditions and laser irradiance settings.<sup>41</sup>

The full scan mass spectrum for sinapinic acid, the other most commonly used matrix compound, is given in Figure 4-7a. In this figure is a peak at  $m/z$  224 for the molecular ion surrounded by many smaller peaks, particularly below  $m/z$  210. While the molecular peak is easily seen, the smaller ion peaks are not easily discernable and their assignment to sinapinic acid fragments or background is difficult. This result is another example of the need for tandem mass spectrometry to obtain analytically useful information from laser desorption ionization. As shown before for TMPA, Figure 4-7b gives the single ion isolation scan of molecular sinapinic acid. In this mass spectrum, we also see a few small peaks at  $(M+1)$  and  $(M-1)$ , but isolation is essentially complete. The ion intensity for the peak at  $m/z$  224 is more than ten times greater than the ion intensity in Figure 4-7a and probably due to a change in sample surface conditions to improve ion production (similar to the process seen for 2,4-DNA in Figure 4-6. Figure 4-8 gives the daughter mass spectrum of sinapinic acid. While we still have molecular ions at  $m/z$  224 due to incomplete dissociation conditions, there are also peaks at  $m/z$  209 for  $[M-CH_3]^+$ ,  $m/z$  193 for  $[M-OCH_3]^+$ ,  $m/z$  179 for  $[M-COOH]^+$ , and  $m/z$  164 for  $[M-C_2O_2H_4]^+$ . The quality and characteristics of the LDI mass spectra shown above are similar to those obtained by Heller *et al.* and Glish *et al.* for similar studies.<sup>38,39</sup>

### Matrix-Assisted Laser Desorption Ionization

The purpose of the following experiments were to determine whether a mixture of the UV-absorbing compound with the analyte compound would enhance

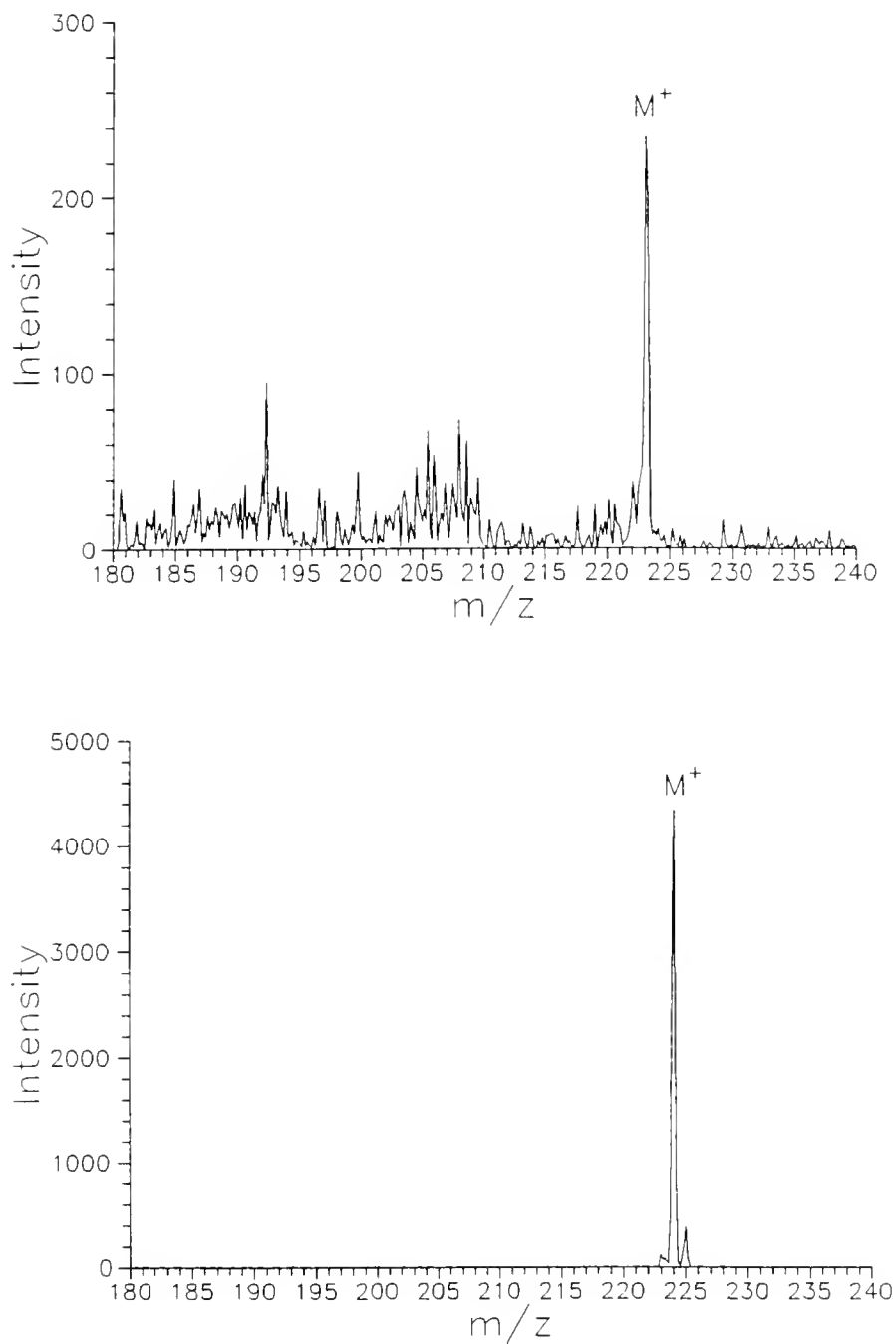


Figure 4-7. LDI mass spectrum of sinapinic acid, a) full mass scan, b) isolation of molecular ion at  $m/z$  224.

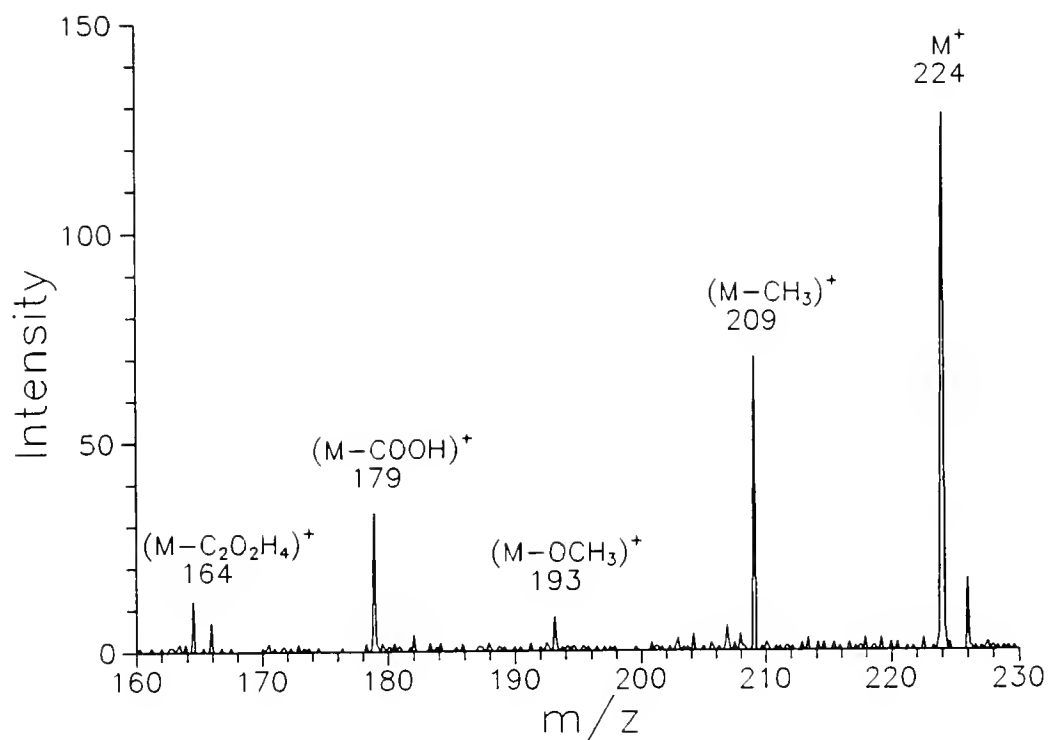


Figure 4-8. Daughter mass spectrum of sinapinic acid molecular ions produced by LDI.



the production of molecular or pseudo-molecular analyte ions. As discussed in Chapter 1, matrix-assisted laser desorption ionization (MALDI) was developed to produce molecular ions for thermally labile and involatile compounds. This method is usually applied to biological compounds such as peptides and proteins. MALDI was initially utilized in our laboratory for the enhancement of the production of molecular spiperone ions from the solid residue of the drug compound. Two important aspects, however, needed to be considered for the application of MALDI to spiperone. First, suitability of the method to spiperone and ease in obtaining molecular ions needed to be evaluated. Second, the production of higher mass ions formed at the ring surface using MALDI may pose a problem for the internal ionization configuration used on the ion trap. Initial experiments by Beavis and Chait showed that peptide ions formed by MALDI carry initial kinetic energies that increase linearly with mass, which could be a potential problem for efficient trapping of ions. However, later work by Pan and Cotter as well as Beavis and Chait, demonstrated that initial kinetic energies begin to level off at higher mass.<sup>34,35</sup> These two research groups showed that MALDI ions essentially have around the same velocity (750 - 1000 m/s). Therefore, with nearly equal velocities, the higher the mass the higher the kinetic energy. These results, along with the successful trapping of peptide and proteins ions in a Fourier-transform mass spectrometer, suggested that MALDI ions formed in ion trap could be stored for analysis as well.

Another consideration for the application of MALDI to the ion trap, although not for spiperone analysis, was that ions formed by MALDI typically carry a single

charge unlike the multiply charged ions produced by electrospray ionization. This characteristic of MALDI limits the mass range that can be achieved utilizing ions carrying a high number of charges. While this limitation is not a problem for spiperone (MW 395) or other drug compounds which have molecular masses below the conventional ion trap maximum mass (650 u), the utilization of MALDI for high mass ions will require mass range extension methods to be applied to the ion trap as well. Results from this approach have been demonstrated by a few research groups for the analysis of peptides and proteins.<sup>19</sup>

### MALDI of Spiperone

Spiperone, or spiroperidol (8-[3-(p-fluorobenzoyl)propyl]-1-phenyl-1,3,8-triazaspiro[4.5]decan-4-one), is an antipsychotic drug which was first suggested for use in evaluating the ion trap by Mike Lee of Bristol-Myers Squibb. He was trying to detect spiperone that had been sprayed onto the surface of a tissue sample using secondary ion/time-of-flight mass spectrometry. Initially, spiperone was analyzed in our laboratory using LDI. The resultant mass spectrum is shown in Figure 4-9. The molecular ion peak which would be situated at  $m/z$  395 is hardly discernable in this spectrum. All of the spiperone that is ionized is also fragmented. The two major ions obtained are the spiperone fragment ions at  $m/z$  165 and  $m/z$  98. The low mass cutoff during trapping and storage was 40 u and the helium pressure was 0.6 mtorr. For similar conditions of low mass cutoff and helium pressure, matrix-assisted laser desorption ionization produces the results shown in Figure 4-10. To obtain this

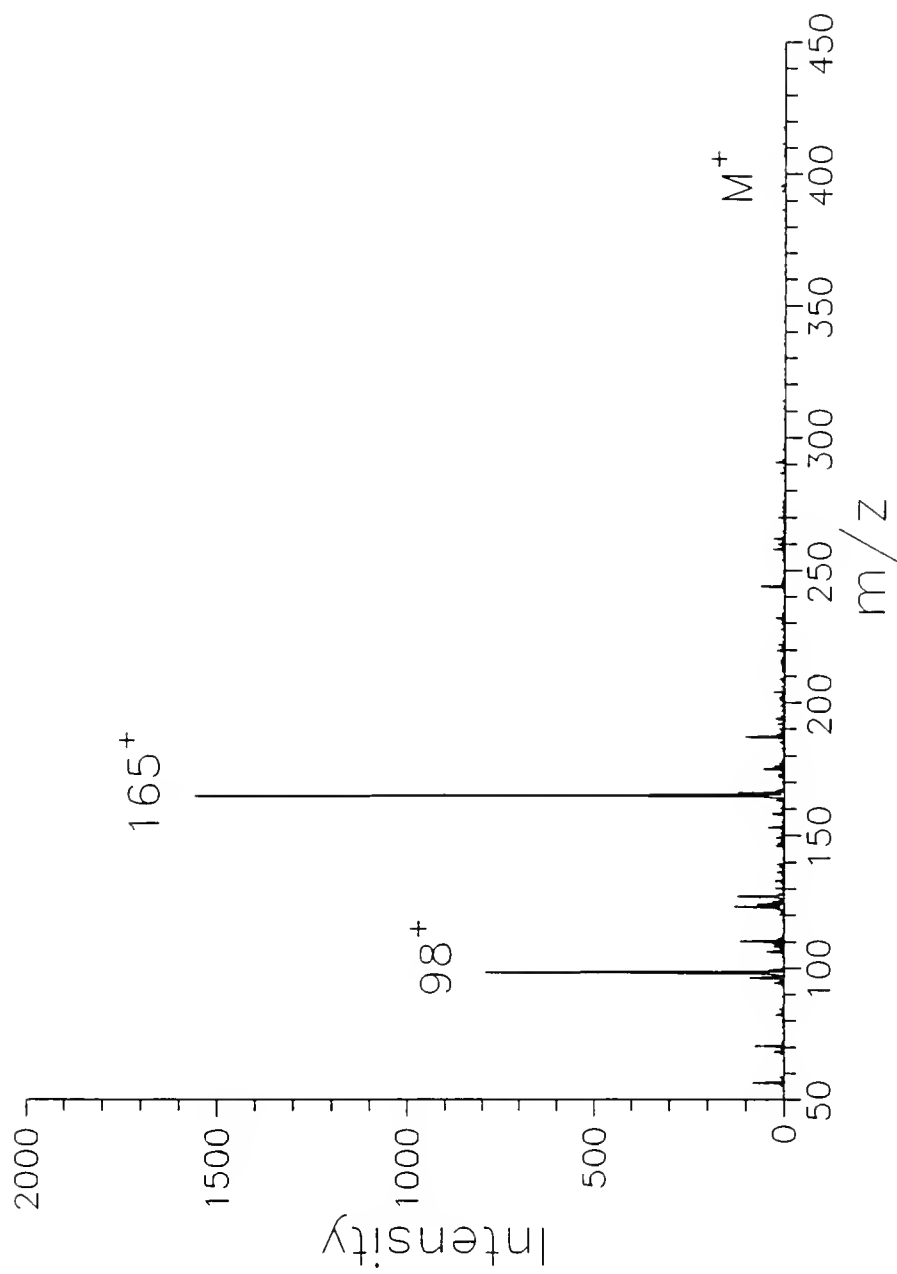


Figure 4-9. Laser desorption ionization mass spectrum of spiperone (MW 395).

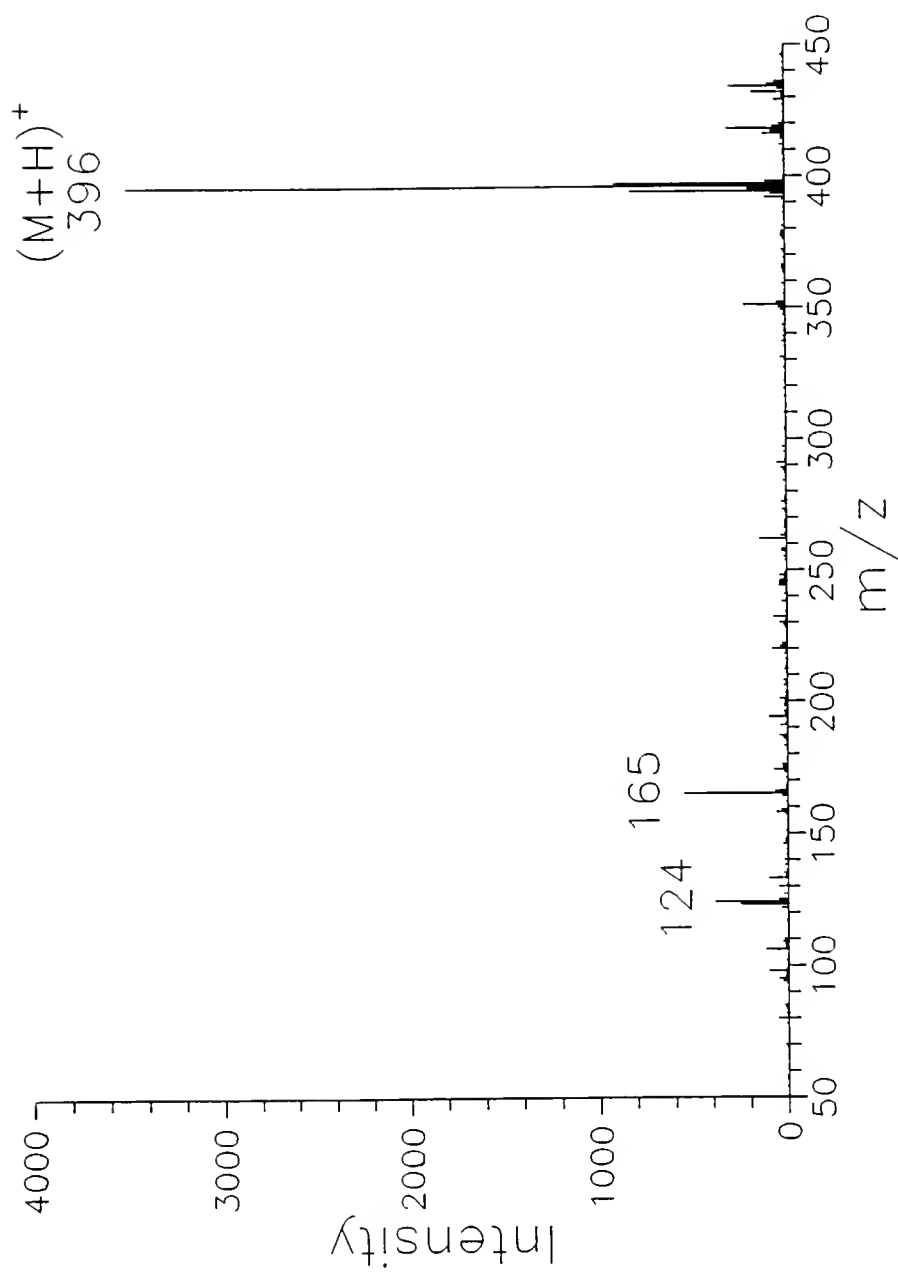


Figure 4-10. Matrix-assisted laser desorption ionization mass spectrum of spiperone using nicotinic acid matrix (0.5% TFA) in methanol.

spectrum, 4  $\mu$ L of a 0.5 M nicotinic acid matrix solution with 0.5% trifluoroacetic acid (TFA) was placed on a cleaned stainless steel probe tip surface. The TFA was added to help promote dissolution of the matrix compound into the solvent. When this solution dried, 4  $\mu$ L of a 0.5 mM solution of spiperone was placed on the probe tip surface on top of the crystals formed from the matrix solution. The addition of the spiperone/methanol solution caused the matrix crystals to dissolve. The analyte and matrix compounds were mixed in a 1:1000 molar ratio on the probe tip. With the evaporation of the methanol solvent, a very thin white film was formed over probe tip surface. Higher concentrations than the one mentioned above would give crystals which clumped together on the probe tip surface, much in the same way it would for 1 g/L solution of TMPA and other organic salts that were studied.

In Figure 4-10, we see the protonated spiperone ion peak at  $m/z$  396. It is the base peak in the spectrum and more than five times greater in intensity than the  $165^+$  fragment ion of spiperone. Immediately surrounding the protonated spiperone peak are peaks at  $m/z$  394, 395, and 397. While the molecular ion and the carbon-13 peak may contribute to this series of peaks, more likely their appearance is due to peak spread and loss of mass resolution. Above the protonated spiperone peak around  $m/z$  418 and 434 are small peaks indicative of the sodium and potassium additions to spiperone, respectively. The  $m/z$  165 ion is most probably due to the spiperone fragment seen in Figure 4-9, but the peak at  $m/z$  124 is probably a fragment ion of nicotinic acid which was used as the matrix compound. As discussed in the Chapter 1 introduction to MALDI, the nicotinic acid matrix absorbs the laser

energy and is desorbed from the sample surface. During that process, the flux of matrix ions carries intact spiperone molecules off the sample surface and provides a source of hydrogen for protonation reactions to occur in the dense gas plume region just of the sample surface. Although the MALDI process has not been fully explained, the results of the method are successful as a soft ionization technique and exemplified by the differences in the two mass spectra shown in Figures 4-9 and 4-10. The differences between the two laser ionization approaches can be utilized analytically similar to the differences between electron ionization and chemical ionization.

#### MALDI Signal Lifetimes

Aside from the increase in molecular ion production from spiperone as shown in Figure 4-10, the length of time the spiperone ion signal lasts also increases using MALDI. The plot of relative intensity of the  $(M+H)^+$  ion of spiperone versus scan is given in Figure 4-11. In this plot, the ion signal is above 50% of its maximum value for 15 scans. Between the 16th and 35th scan the signal decreases to less than 10% of its maximum value. It is important for the ion signal from a particular sample residue to last more than a few scans so that proper adjustment of the laser desorption conditions, or the instrumental settings, can be made to improve the quality of the mass spectrum. For comparison, the relative intensity of the protonated spiperone from the LDI experiment shows that in LDI optimization of parameters for molecular spiperone would be essentially impossible.

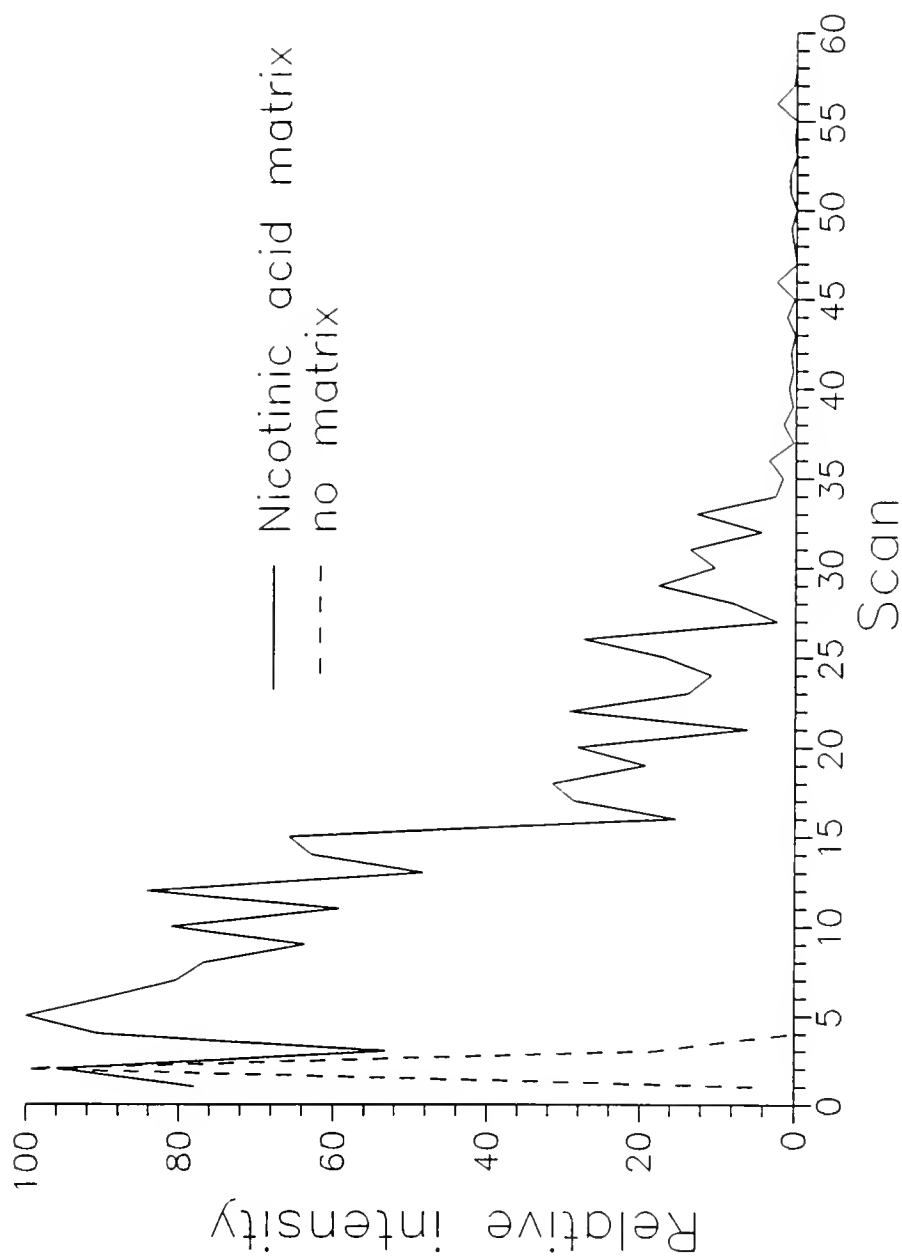


Figure 4-11.  $(M+H)^+$  signal of spiperone vs. time for MALDI using an acidified nicotinic acid matrix and LDI.

When the intensities of protonated spiperone and  $165^+$  fragment ion are plotted, as shown in Figure 4-12, one can see that, although both ion signals vary greatly in intensity, the protonated spiperone ion decreases over 35 scans while the  $165^+$  ion stays generally the same in intensity. This plot shows that the decrease in molecular spiperone ion production is not replaced by increased production in fragmentation, but that the spiperone/matrix mixture on the probe tip surface is changing in a manner that the MALDI process is no longer productive. This effect may be due to a change in the spiperone/matrix mixture caused by the laser desorption itself. For the most part, however, loss of ion signal over several laser pulses was usually attributed to removal of sample from the probe tip surface with each laser shot. The rate of sample removal was decreased by decreasing the laser irradiance, resulting in ion signals being maintained over more laser shots.

### Laser Irradiance

Laser irradiance not only affects how long the sample lasts on the probe tip surface before being completely ablated, but is also a very important factor in performing good MALDI and obtaining mass spectra with minimal fragmentation of the ion of interest. This optimization of the MALDI method is also of particular importance in analyzing mixtures so that the mass spectra are much simpler due to the lack of fragmentation ions and determination of molecular masses is much easier (similar to chemical ionization).



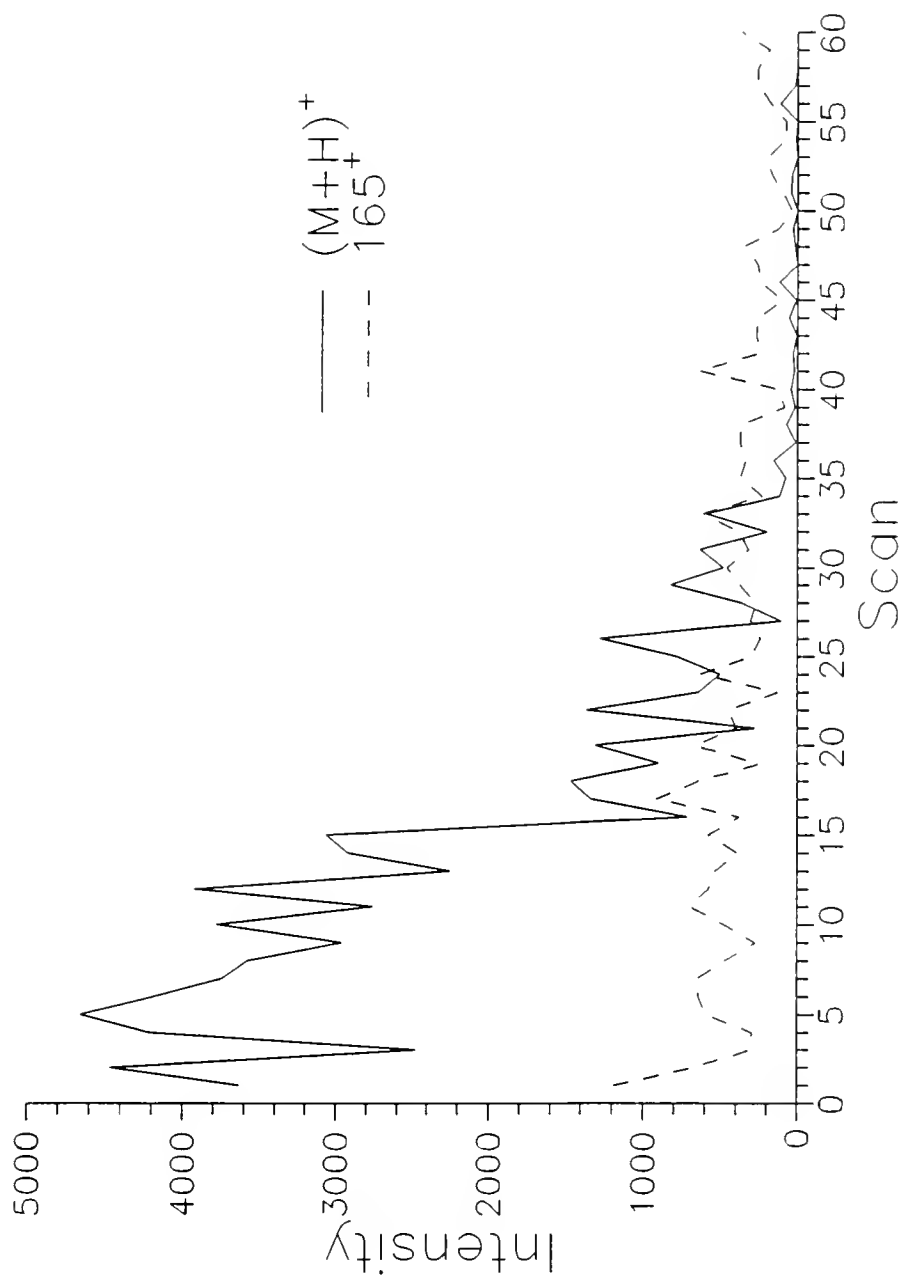


Figure 4-12.  $(M+H)^+$  and  $165^+$  fragment ion of spiperone vs. time.

Laser irradiance describes the power applied by a laser pulse per area and is usually given in units of  $\text{W}/\text{cm}^2$ . Electronically measuring the power of a pulsed nitrogen laser is difficult due to the short pulse time (3 ns) and requires expensive instrumentation. The absolute measurement of laser irradiance was not needed in order to perform our studies. The laser irradiance was approximated to the typical value reported for MALDI ( $10^6 \text{ W}/\text{cm}^2$ ) by calculation from the specifications provided with the nitrogen laser and measurement of the laser spot area.

When a polished surface of the stainless steel probe tip is hit by several hundred shots from the nitrogen laser using the optics described above, the spot left on the surface is rectangular in shape with the approximate dimensions  $0.4 \text{ mm} \times 0.1 \text{ mm}$ . These dimensions give a laser sampling area of  $0.04 \text{ mm}^2$ . For a sample of spiperone and sinapinic acid matrix solution deposited evenly on the probe tip surface, the hole made by the laser under vacuum in the sample is fairly circular with an approximate diameter of  $0.4 \text{ mm}$ . This diameter gives a laser sampling area of  $0.13 \text{ mm}^2$ . As described in Chapter 2, the given peak power (85 kW) over this spot size gives a laser irradiance of approximately  $6 \times 10^7 \text{ W}/\text{cm}^2$ . The laser irradiance was then controlled using neutral density filters. In the internal ionization configuration, the filters were added so that only about 10% of the laser energy was focussed onto the sample surface, a calculated irradiance of  $6 \times 10^6 \text{ W}/\text{cm}^2$ . Considering that other laser transmission reductions were not taken into account (e.g., energy loss at the flange window and focussing lens), the actual laser irradiance is most likely less than the calculated value and nearer to the reported optimum

irradiance value of  $1 \times 10^6$  W/cm<sup>2</sup>. A quick optimization of laser irradiance usually needs to be performed for each sample prior to obtaining the best data for molecular ion detection.

An example of laser irradiance optimization is shown by a comparison of the mass spectra given in Figure 4-13. In Figure 4-13a, a MALDI mass spectrum of spiperone using DHB matrix with 0.1% TFA and a calculated laser irradiance of  $6.4 \times 10^6$  W/cm<sup>2</sup> is shown (nominal optical density for the neutral density filters was 1.0). This spectrum indicates that no protonated spiperone ion was produced and the largest ion intensity obtained was for the spiperone fragment ion with  $m/z$  165. Several other unresolved peaks were also observed around the mass range for other spiperone fragment ions. Clearly, the laser irradiance is too high in this experiment. In Figure 4-13b, we see the MALDI mass spectrum obtained for the same sample under the same instrumental conditions (e.g., both are performed at a low mass cutoff of 40 u) except for a lower laser irradiance value of  $5.1 \times 10^6$  W/cm<sup>2</sup>. In this mass spectrum, where nominal optical density for the neutral density filters combined was 1.1, we see the appearance of protonated spiperone at  $m/z$  396 and the sodium molecular adduct at  $m/z$  418. We also see the spiperone fragment ions at  $m/z$  165, 123, and 98. The peak at  $m/z$  136, not ever seen in pure spiperone analyses, is attributed to the water-loss fragment of the matrix compound, 2,5-dihydroxybenzoic acid, as shown in Figure 4-4. It is interesting to note that although the DHB matrix is in much greater amount on the probe surface than the spiperone analyte, it does not appear to any extent except for the fragment ion at  $m/z$  136. The protonated

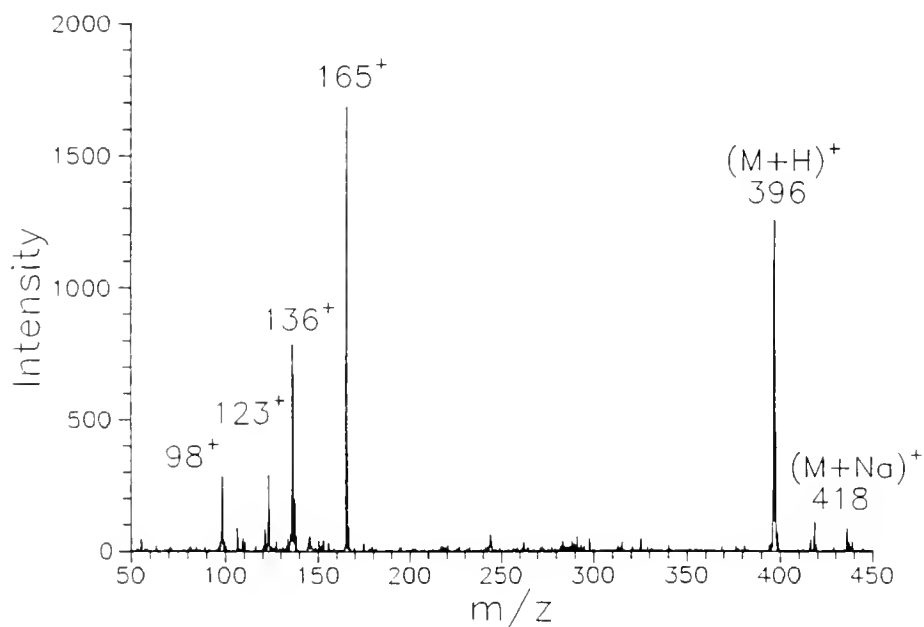
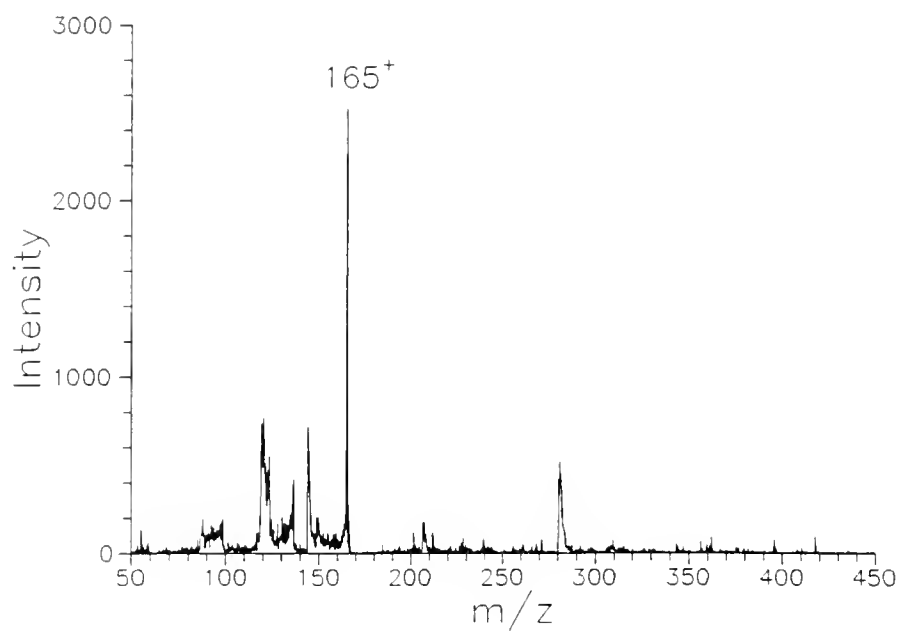


Figure 4-13. MALDI mass spectrum of spiperone using 2,5-dihydroxybenzoic acid with 0.1% TFA: a) laser irradiance =  $6.4 \times 10^6$  W/cm<sup>2</sup>, b) laser irradiance =  $5.1 \times 10^6$  W/cm<sup>2</sup>.

spiperone peak may not be the base peak in this mass spectrum, but these spectra in Figure 4-13 clearly illustrate the significant effect laser irradiance has upon the MALDI process.

### Matrix Preparation

Initially, the particular compound used for the matrix did not seem to make much difference, especially when compared to the effect of laser irradiance. With further experience using MALDI, several trends were observed in the quality of the spectra such as the ability to identify the ions obtained, the uniformity of the mass spectra. These subtle trends caused us to focus the development of the MALDI method on the use sinapinic acid and DHB matrices. As mentioned earlier, trifluoroacetic acid (TFA) was added to the matrix solutions to help dissolve the matrix compound into the solution. As suggested in the literature, TFA was added to concentration ranging from 0.1% to 0.5%.

Concentrations were primarily controlled by two factors. First, the amount of matrix and sample applied to probe tip was limited to avoid clustering of crystals during the evaporation of solvent. Second, sample and matrix amounts were used that were found to give strong ions signals for several laser shots and multiple sampling spots on the probe tip surface before the sample had to be replaced. The less often the sample had to be replaced, the less time it took to optimize the instrumentation and perform various studies.

Methanol is the matrix solvent that was used in almost all of the MALDI experiments to insure the complete dissolution of the matrix compound and the analyte. However, some sample analytes were in aqueous solutions (e.g., leucine enkephalin, shown later) which required the use of similar solvents or solvent mixtures for the matrix solutions as suggested in the literature. Therefore, a mixture of 70:30 acetonitrile:water was evaluated for comparison to the spectra obtained performing MALDI of spiperone in methanol solutions. In Figure 4-14 can be seen the resultant mass spectrum of spiperone using DHB matrix in the 70:30 acetonitrile:water solution with 0.1% TFA. The mass spectrum is essentially the same as the spectrum obtained using the methanol solutions except there are no sodium or potassium adducts observed and the fragmentation was essentially non-existent. These results indicate a possibly better MALDI solvent in acetonitrile:water for this particular experiment, but other ions may be seen in the mass spectrum due to contamination in the analyte sample. Also, as stated previously, the solvent used for the analyte solvent should dictate which solvent is used for the matrix solution. For example, it was observed that when adding analyte and matrix solution to mix on the probe tip, the matrix crystals are pushed aside when the aqueous analyte solution is added. Therefore, the aqueous analyte solution needed to be deposited on the probe tip first, followed by the hydrophobic matrix compounds.

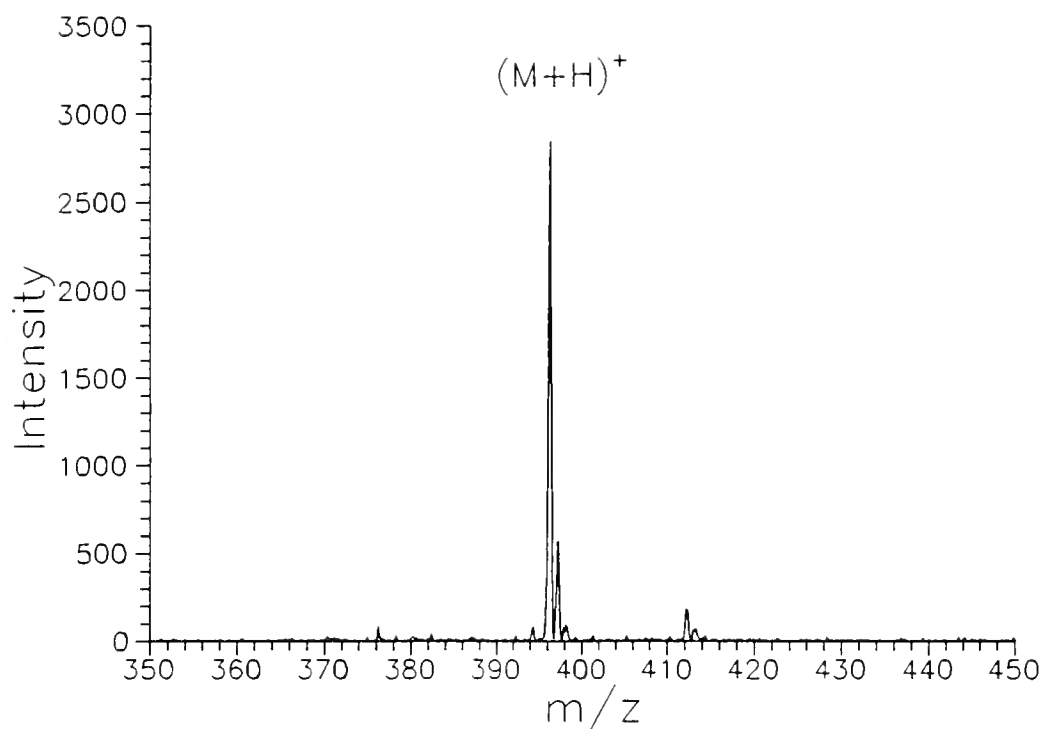


Figure 4-14. MALDI mass spectrum of spiperone using 2,5-dihydroxybenzoic acid matrix in 70:30 acetonitrile:water and 0.1% trifluoroacetic acid.

### Lowest Sample Amount

There are two methods used in the literature to describe the sampling amount or limit of detection for laser desorption experiments. The first method is a measurement of the amount of total sample deposited on the probe tip surface. This measurement is important in that it describes the total amount of sample required for analysis. The second method is a measurement of the amount of sample ablated during the laser desorption event to produce the mass spectra. This amount is usually obtained by measuring the size of the crater created by the laser pulse and calculating the amount sampled from the total amount deposited (presumably uniformly) over the entire sample area. This measurement is also important in that it relates the idea that any sample left after analysis by laser desorption could be easily retrieved for further analyses since it should be undamaged.

In Figure 4-15, the protonated molecular peak from MALDI of 74 ng of spiperone deposited on the probe tip is shown. The  $m/z$  396 ion peak is clearly discernable with an intensity of 54 counts (arbitrary units). To obtain this spectrum, 4  $\mu\text{L}$  of a 47  $\mu\text{M}$  solution of spiperone in methanol was placed on the probe tip, and mixed with 4  $\mu\text{L}$  of a 48 mM DHB matrix solution. The total spiperone sample, therefore, spread over the probe tip is 74 ng, or 187 picomoles (method 1). With a  $0.13\text{ mm}^2$  spot size and a  $6.7\text{ mm}^2$  sample surface, the approximate fraction of the spiperone desorbed by the laser is 0.019. Therefore, the amount of spiperone ablated to obtain the mass spectrum is approximately 1.4 ng, or 3.5 picomoles (method 2).



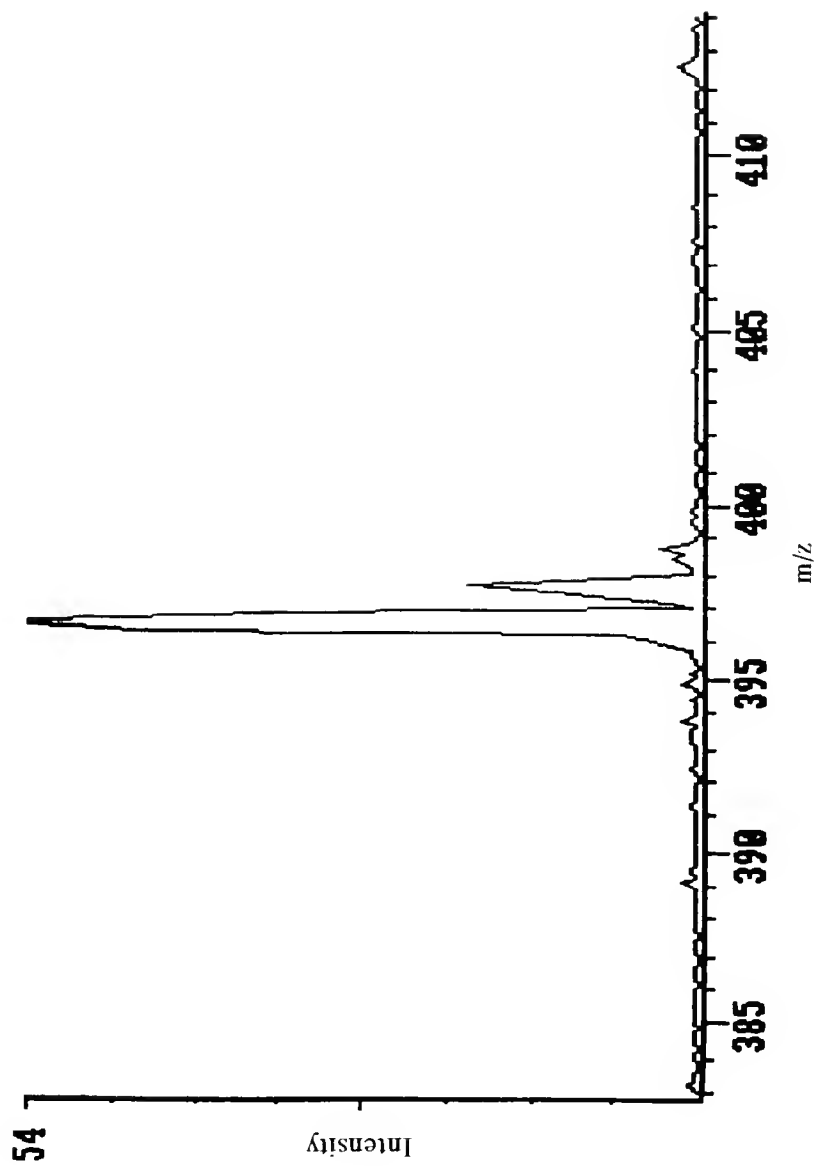


Figure 4-15. MALDI/MS of 74 nanograms of spiperone (4  $\mu$ L of a 47  $\mu$ M methanol solution) mixed on the probe tip with 4  $\mu$ L of 48 mM DHB matrix solution.

Chambers *et al.* were able to extrapolate a theoretical detection limit of 4 femtomoles from data obtained for MALDI/ITMS of leucine enkephalin.<sup>57</sup> Femtomole detection limits for other polypeptides below  $m/z$  2000 and picomole detection limits for polypeptides for  $m/z$  2800 to 12000 were also obtained. The increase in detection limit with analyte molecular mass was explained with the pseudo-potential well depth model.<sup>57</sup> Basically, two competing processes are believed to take place during the trapping of ions. First, the higher the mass of the ion, the larger amplitude of the trapping field required for efficient trapping (due to the higher kinetic energy of the ion). Second, the larger amplitude trapping field is also believed to have a lower acceptance trapping volume which decreases the trapping efficiency. This smaller trapping volume requires the ions to be positioned more towards the center of the trap so that they may be trapped. In a previous study, Glish *et al.* obtained spectra with sample loadings of 10 picomoles for various unspecified samples.<sup>39</sup> They did note, however, that the single laser shot spectra at this sample level were erratic due to ion statistical fluctuations. Averaging ten spectra, however, resulted in spectra with signal-to-noise ratios greater than five. They also believed that there was much room for improvement of their preliminary results.

#### MALDI/MS/MS of Spiperone

The additional adduct or matrix ions seen in the various mass spectra for spiperone pose less of a problem for sample analysis with the ion trap than with

other mass analyzers, since multiple stages of mass analysis can be employed for increased selectivity. Figure 4-16 shows the daughter mass spectrum obtained by collision-induced dissociation of protonated spiperone,  $m/z$  396, produced with MALDI. This daughter spectrum is similar to that obtained using other methods of sample introduction and mass analysis including solids probe chemical ionization on the ion trap and triple stage quadrupole. The low mass cutoff used for trapping and storage was 40 u, which corresponds to a  $q_z$  value of 0.092. Although this  $q_z$  value is much lower than normally used for EI or CI (typically 0.3), results obtained with a single stage of mass analysis demonstrated efficient trapping. The scan function used to perform MS/MS on spiperone is described in Table 4-1. In this table, the list of the 19 steps for MS/MS of  $m/z$  396 using the 2-step isolation scan function is given. Steps #8 and #11 show the function of 2-step method which is the ejection of the higher mass ions ( $m/z > 396$ ) followed by the ejection of the lower mass ions ( $m/z < 396$ ), respectively. Following these two functions, collision-induced dissociation is performed in step #15 to produce the daughter ions which are detected in step #18. The steps in between the ones described are for either cooling the ions to the center of trap or for changing the low mass cutoff to the desired level.

Low mass cutoff levels used in MALDI scans were almost always 40 u or above in order to eject sodium and potassium ions from the trap. Higher low mass cutoff levels, from 100 to 300 u, were evaluated for use in MALDI scans, but results were sporadic depending on the sample. Most often, low mass cutoffs above 150 u

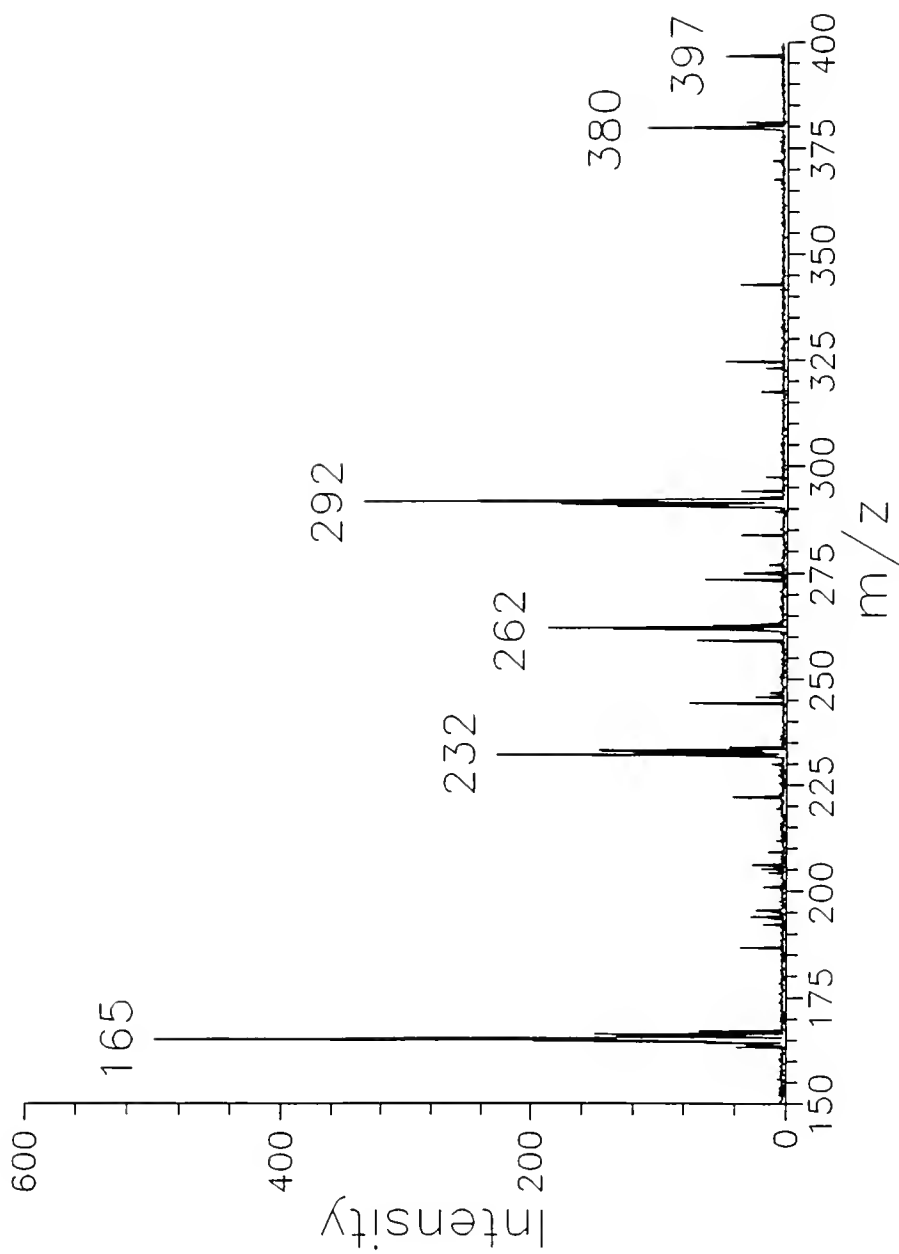


Figure 4-16. MALDI/MS/MS daughter spectrum of protonated spiperone,  $m/z$  396 (average of 10 scans).

Table 4-1. Steps in the MALDI/MS/MS scan function for the analysis of spiperone. Start LMC and End LMC describe the initial and final Low Mass Cutoff levels during each step in terms of mass units (u).

#		<u>Start LMC</u> (u)	<u>End LMC</u> (u)	<u>Aux. Voltages</u>	<u>Time</u> (ms)
1	Trigger	40.0	40.0		1.0
2	Pre-desorption	40.0	40.0		2.0
3	Laser trigger	40.0	40.0		0.1
4	Cool period	40.0	40.0		100.0
5	rf ramp #1	40.0	285.0		2.0
6	rf ramp #2	285.0	305.3		1.0
7	Cool period	305.3	305.3		5.0
8	Eject higher mass	305.3	305.3	DC = 664 V	5.0
9	rf ramp #3	305.3	370.7		2.0
10	Cool period	370.6	370.6		5.0
11	Eject lower mass	370.6	370.6	DC = -44.6 V	5.0
12	Cool period	370.6	370.6		5.0
13	rf ramp #4	370.6	40.0		3.0
14	Cool period	40.0	40.0		5.0
15	CID	40.0	40.0	TV = 0.1 mV	5.0
16	Cool period	40.0	40.0		5.0
17	Multiplier on	40.0	40.0		2.0
18	Data acquisition	40.0	650.0	TV = 6 V	110.5
19	rf off	0.0	0.0		1.0
				Total time =	268.6

gave few if any ions. The effect of low mass cutoff was studied for ions less than 100 u in Chapter 3. The results shown are applicable to the larger mass ions studied in this chapter except that for higher mass ions the trapping acceptance volume becomes smaller. The low mass cutoff will also be evaluated for the instrumental configuration described in Chapter 5.

It is also possible to perform MS/MS on the spiperone fragment ions produced in the laser desorption ionization process by isolating the fragment ion at  $m/z$  165 and performing CID. As seen in Figure 4-17, the MALDI/MS/MS mass spectrum of the  $m/z$  165 ion shows peaks for masses which are similar to those obtained for non matrix-assisted laser desorption. The structure of some of these ions is also given in the figure. The appearance of the peak at  $m/z$  171 is not understood. The intensity ratios of the various daughter ions is different from any seen in other spiperone mass scans. The large intensity of the  $m/z$  123 ion, much greater than the other fragment ions, was most likely the favored product of CID of the  $m/z$  165 ion.

In order to determine if the characteristics of the LDI and MALDI spectra are similar to more conventional ionization methods, the electron ionization (EI) and chemical ionization (CI) mass spectra of spiperone were obtained from a sample thermally desorbed from a solids probe. Figure 4-18 is the background subtracted EI mass spectrum of spiperone heated on the solids probe tip outside the ion trap assembly. Although contamination is suggested by several unknown peaks below  $m/z$  200 (at the time, the instrument had just been used for particle beam LC/MS analysis

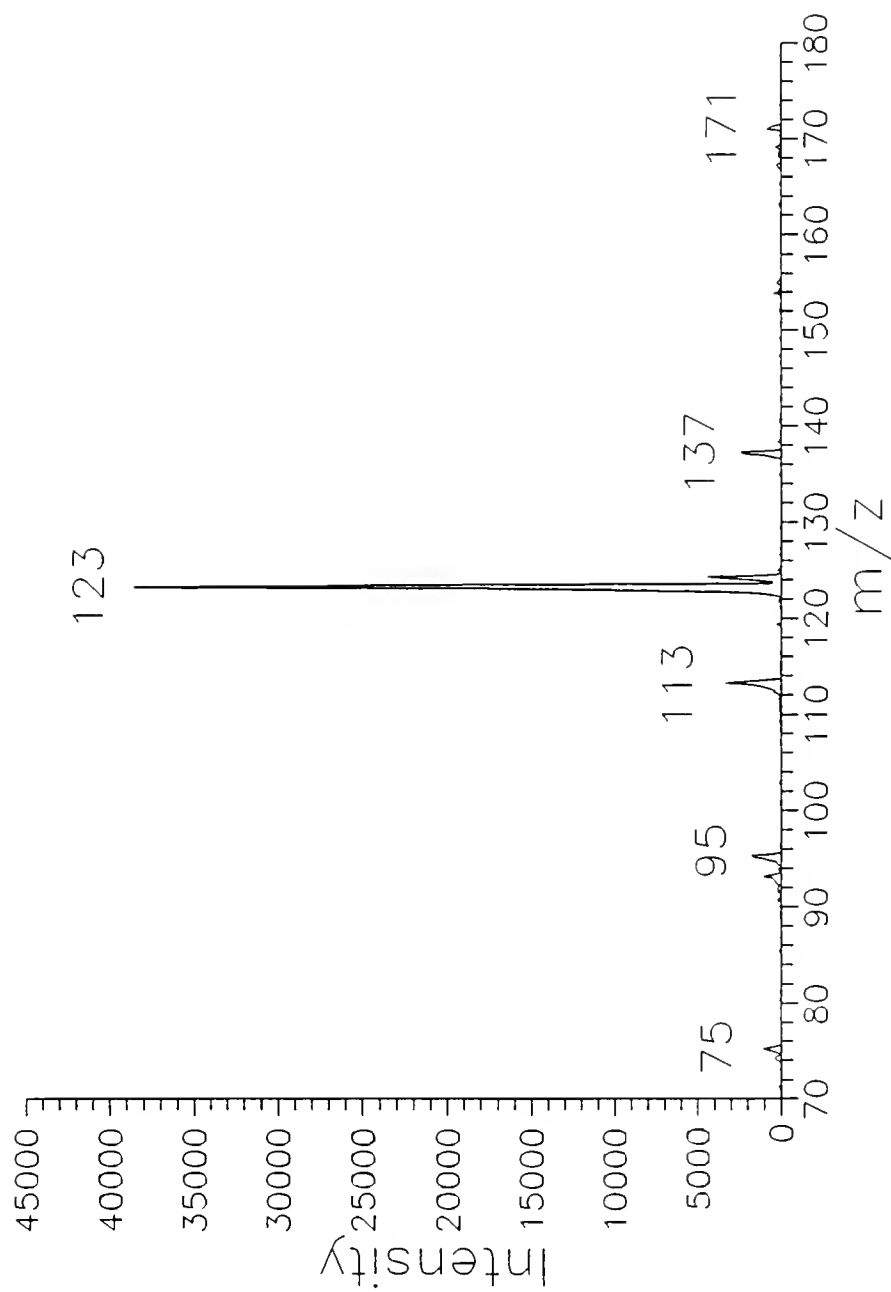


Figure 4-17. MALDI/MS/MS daughter spectrum of m/z 165 fragment ion of spiperone (average of 10 scans).

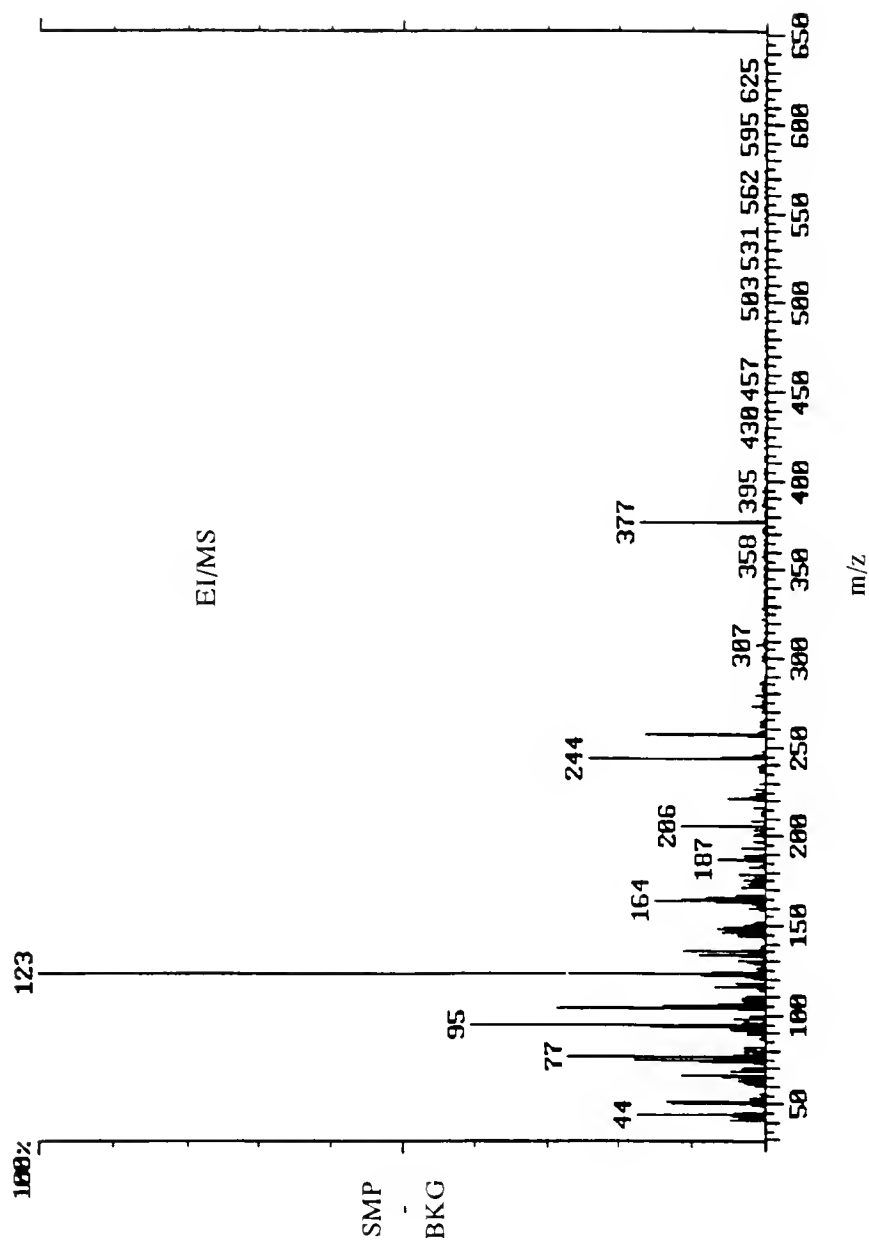


Figure 4-18. Electron ionization of spiperone off the solids probe on the ion trap mass spectrometer (10 microscans). Low mass cutoff during trapping was 40 u and ionization time was 2 ms.



and was believed to be dirty), the  $123^+$  fragment ion of spiperone is clearly detected and is the base peak. No molecular spiperone is detected as would be expected for a compound of its structure under the hard ionization conditions of EI.

For chemical ionization, methane was used as the reagent gas. Methane was introduced into the vacuum chamber through a leak valve and ionized with EI. The methane reagent ion at  $m/z$  17 was isolated and reacted with spiperone thermally desorbed from the solids probe. The mass spectrum is shown in Figure 4-19. The background subtracted spectrum is the average of scans 125 through 150 and shows protonated spiperone as the base peak. There are also some fragment ions seen, particularly at  $m/z$  165 and 98, which are easily identifiable from previously obtained spectra, but these ions are most likely due to residual electron ionization of spiperone at the beginning of the scan function. In the ion trap, the methane and sample volatiles exist with the products from EI and CI unless an isolation or ejection step is added to remove unwanted ions. It should also be noted, however, that the endcap was heated (as done for the particle beam experiments) and therefore the CI results may be inaccurate if the highly heated endcap surface ( $200^\circ\text{C}$ ) affected the sample production of spiperone gaseous neutrals. As in the previous EI spectrum, much chemical interference from contaminated ion trap electrode surfaces may have contributed to the background of the mass spectrum. Subtraction of this background, as done in the mass spectrum of Figure 4-19, removes most of these extraneous ions. A plot of the protonated spiperone intensity versus scan from the methane CI experiment is shown in Figure 4-20. The reaction time between

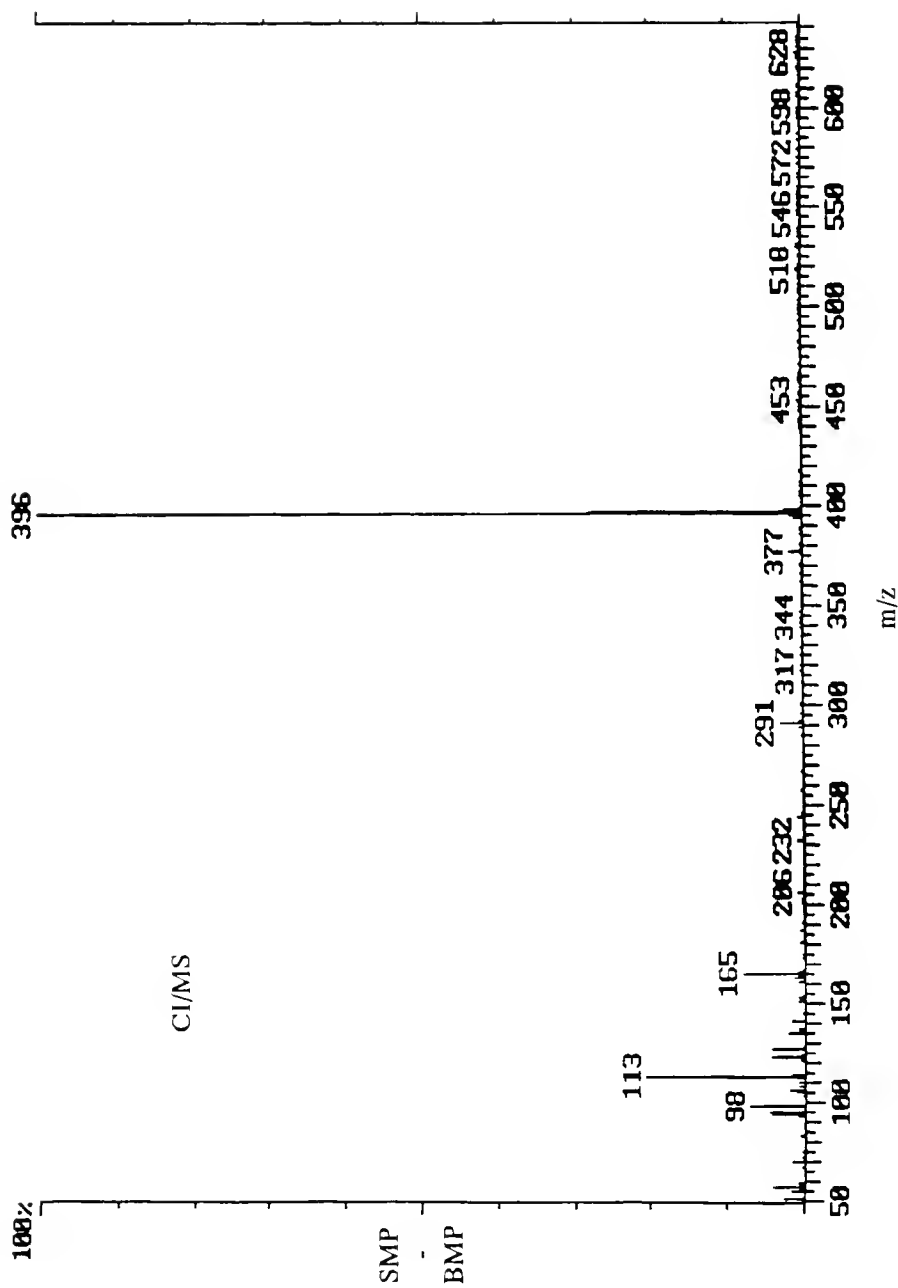


Figure 4-19. Methane chemical ionization mass spectrum of spiropiperone off the solids probe on the ion trap mass spectrometer (10 microseconds). Reaction time was 25 milliseconds.

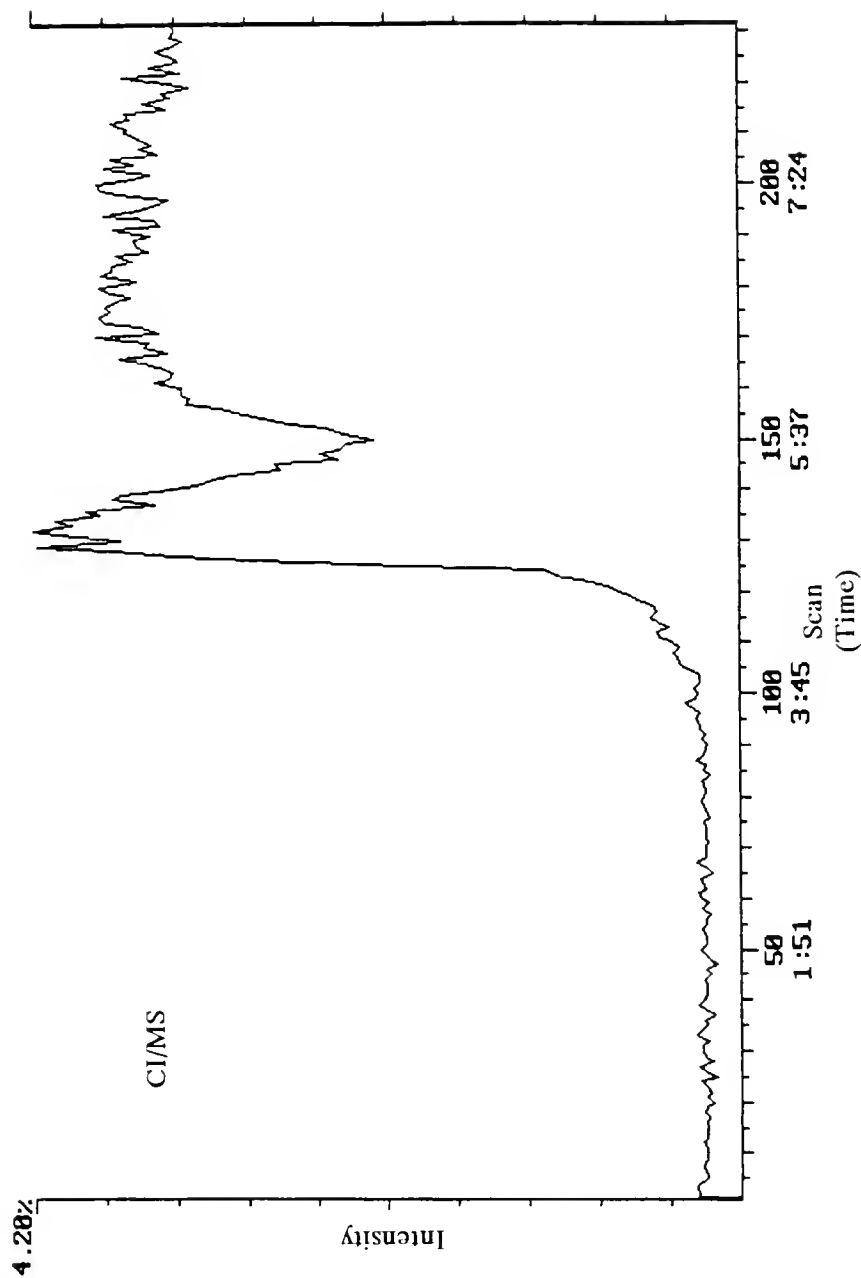


Figure 4-20. Intensity versus scan plot of protonated spiperone ( $m/z$  396) using methane chemical ionization of spiperone off the solids probe (10 microscans). Reaction time was 25 ms. Manifold temperature was 100 degrees celsius. Initial solids probe temperature was 70 degrees celsius and the temperature ramp was 120 degrees/minute, but the maximum ion signal (at scan #132 and retention time 4:57) was obtained after the reaching the final probe temperature.

methane reagent ions and the spiperone thermally desorbed neutrals was 25 ms and each scan consists of 10 microscans. Manifold temperature was 100° C. Initial solids probe temperature was 70° C and the temperature ramp was 120° C/minute, but the maximum ion signal (at scan #132 and scan time 4:57) was obtained after the reaching the final probe temperature.

Similar experiments thermally desorbing spiperone off the solids probe were performed using EI/MS, methane CI/MS, and methane CI/MS/MS on the triple quadrupole mass spectrometer (Finnigan TSQ70) in order to compare the mass spectra obtained on the ion trap. In the probe vial, 4 µL of a 1.6 mM spiperone solution was dried and the residue was heated from 50° C to 250° C at the rate of 50° C/minute. For EI/MS, the results from the triple quadrupole showed no molecular spiperone. Fragment ions were the same as those seen on the ion trap.

For CI/MS and CI/MS/MS, the results from the triple quadrupole also were similar to those obtained on the ion trap in respect to protonated spiperone and spiperone fragment ion types. As on the ion trap, the MS/MS data showed the fragment ion at  $m/z$  165 as the base peak in the daughter mass spectra of protonated spiperone. To obtain the daughter mass spectra, the collision energy in the second quadrupole was set to 25 eV with 0.9 mtorr of argon gas. The third quadrupole was scanned from  $m/z$  50 to 450. The MALDI/MS/MS results for spiperone shown above were also similar to the results obtained by Lee performing FAB/MS/MS and methane desorption CI/MS/MS with the triple quadrupole mass spectrometer.

### MALDI of Leucine Enkephalin

Leucine enkephalin (MW 555), a five amino acid peptide, is a good example of a compound in which a molecular analysis could not be performed with a thermal desorption method. When thermally desorbed from a solids probe, leucine enkephalin decomposes and any ions obtained, even with chemical ionization, are only fragments of the molecule. Leucine enkephalin is also a good compound to test the ability to perform matrix-assisted laser desorption ionization on the quadrupole ion trap mass spectrometer, because many other researchers have shown MALDI spectra of it in the literature using many different types of mass spectrometers. Figure 4-21 shows the MALDI mass spectrum of leucine enkephalin with a peak at  $m/z$  556 for the protonated molecule. The sample was 2  $\mu$ L of a 1 mg/mL solution of leucine enkephalin in distilled water. The matrix used was 2  $\mu$ L of 0.5 M DHB solution (0.1% TFA). The fine structure seen above the protonated leucine enkephalin peak is most likely a split carbon-13 peak. The cause of this split peak is not known. No fragment ion peaks were seen below  $m/z$  556 demonstrating very good MALDI results. No ions were seen above  $m/z$  558 exemplifying the simplicity of MALDI spectra.

In contrast to results shown in Figure 4-21, however, adduct ions were seen in some leucine enkephalin experiments as in a few of the spiperone spectra shown previously. These adduct ions are typically the product of sodium or potassium ions adding to the laser-desorbed neutral molecules.<sup>30</sup> Most often, the adduct peaks are much less intense than the protonated molecular peaks unless the sample is doped

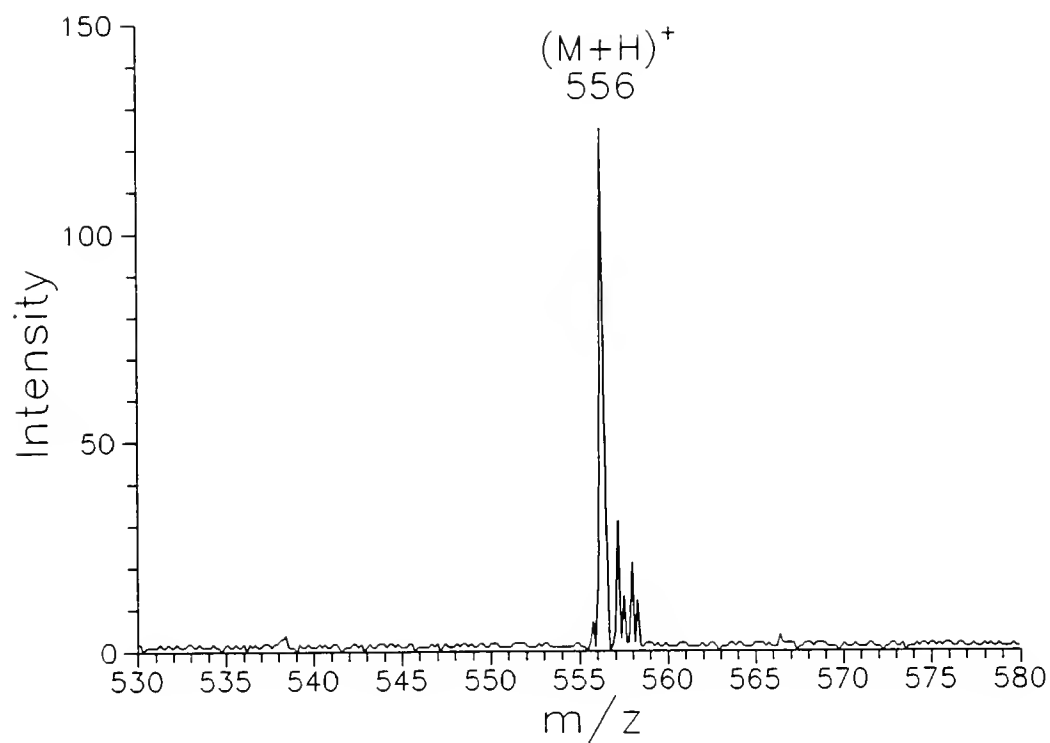


Figure 4-21. MALDI mass spectrum leucine enkephalin (MW 555).

with an alkali metal salt to promote the production of adduct ions. In fact, metal adducts have been used to enhance the ion production from polymer compounds.<sup>30</sup> In "pure" samples, such as the one used in Figure 4-21, inorganic salts should be at trace levels. Unfortunately, adduct peaks were found not only to occur sporadically in MALDI scans, but also to be greater in intensity than the protonated molecular ion. The MALDI experiment of a supposedly similarly pure sample of leucine enkephalin, combined with DHB matrix, gave the mass spectrum shown in Figure 4-22. In this mass spectrum, we not only see the protonated molecular peak at  $m/z$  556, but also molecular adduct peaks at  $m/z$  578 and 600. The ion at  $m/z$  578 is the sodium ion addition. The ion at  $m/z$  600 is formed by the addition of 2 sodium ions and the loss of a proton or  $[M-H+2Na]^+$ . Brodbelt *et al.* have also seen the adduct ions for leucine enkephalin when performing MALDI. The ramifications of these adduct ions are that they make the mass spectra more complex. This increase in complexity of the spectra is problem for mixture analysis. Performing tandem mass spectrometry on these adduct ions may, however, provide enough information to identify the ions produced.

Another interesting observation made from MALDI/ion trap analysis comes from the comparison of these results with those reported by Doroshenko *et al.*<sup>18</sup> In their MALDI/MS spectra of leucine enkephalin using a nicotinic acid matrix, the intensity and shape of the protonated leucine enkephalin peak showed variations due to the rf phase angle at which the ions were formed. In contrast to rf phase angle data shown in chapter 3 of this dissertation, however, the data they obtained were

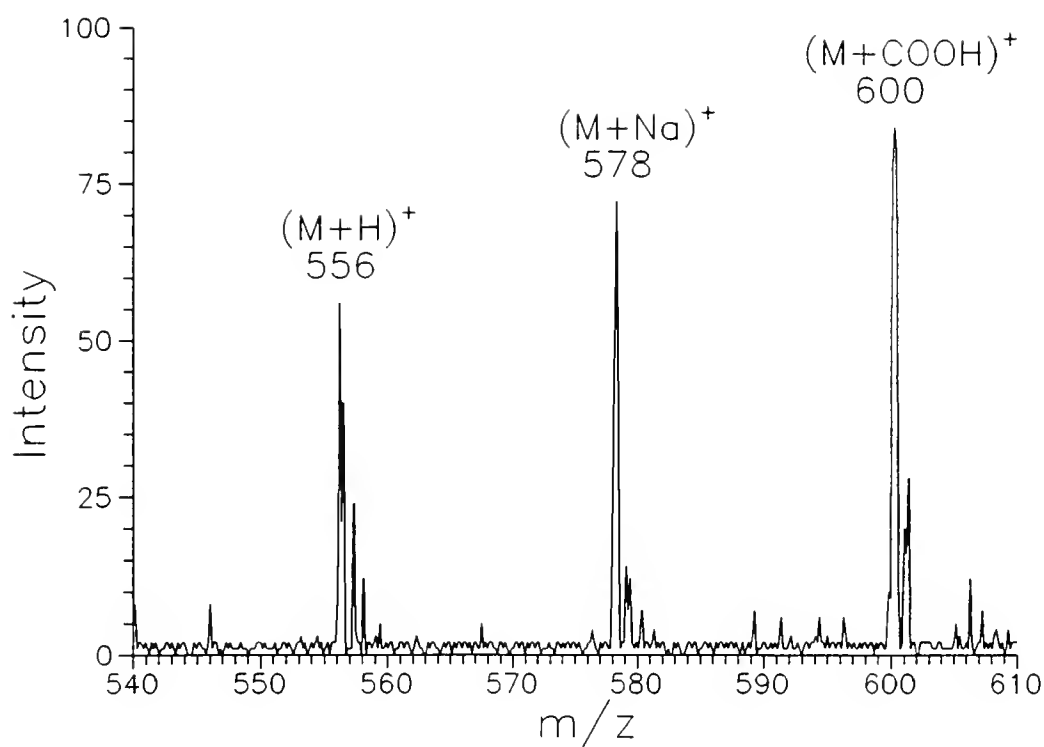


Figure 4-22. MALDI mass spectrum of leucine enkephalin showing the appearance of adduct ions.



only for rf phase angle settings of  $0^\circ$  and  $180^\circ$ . For these two rf phase angle, they showed ion peaks for protonated leucine enkephalin which were different in intensity and shape. The observation of the rf phase angle effect was not explained by Doroshenko *et al.*, except for the suggestion that the phase angle affected ion abundance in the trap which in turn increased or decreased space charging in the ion trap. However, space charging does not explain the appearance of two peaks in their mass spectra in place of a protonated leucine enkephalin peak at  $m/z$  556, as shown in the above spectra. They obtained peaks at  $m/z$  554 and 557. For the  $0^\circ$  rf phase angle, the largest peak was at  $m/z$  554. For the  $180^\circ$  rf phase angle, the largest peak was at  $m/z$  557. They also saw the same bimodal peak behavior for methionine enkephalinamide (MW 572), but did not provide any explanation or ion structures for the observed anomaly.

### Sipiperone in Matrigel

Matrigel basement membrane (Collaborative Biomedical Products) was used as a tissue model to evaluate the LDI/quadrupole ion trap method. Basement membranes are thin extracellular matrices underlying cells *in vivo*. Matrigel is a solubilized basement membrane preparation extracted from the Engelbreth-Holm-Swarm (EHS) mouse sarcoma, a tumor rich in extracellular matrix proteins. Its major component is laminin, followed by collagen type IV, heparan sulfate proteoglycans, entactin, and nidogen. It also contains TGF-beta, fibroblast growth

factor, tissue plasminogen activator, and other growth factors which occur naturally in the EHS tumor.

With larger amounts of Matrigel ( $>3\ \mu\text{L}$ ), the sample does not dry on the probe tip quickly. Therefore, the sample was placed in the probe lock under roughing-pump pressure (50 mtorr) to speed the drying process. When placed in the vacuum of the manifold chamber (1 mtorr), the wet sample crystallizes with an explosive evaporation process. This process was suggested by the protrusion of crystals from the sample surface by about half a millimeter. A drying period of at least five minutes in air was used so that Matrigel mixture samples would dry with smooth and flat sample surfaces on the probe tip.

#### LDI of Spiperone in Matrigel

LDI/MS of  $5\ \mu\text{L}$  of spiperone in Matrigel mixture was performed and a typical mass spectrum is shown in Figure 4-23. No UV matrix compounds or TFA were added and the low mass cutoff was 40 u during trapping and storage. The mass spectrum is a single microscan of  $5\ \mu\text{L}$  of 1 mg of spiperone in 1 mL of Matrigel in its liquid state. As seen in this spectrum, only trace peaks above the noise are seen for spiperone ions at  $m/z$  395 and  $m/z$  165. No other ions are recognizable. The largest peaks, at  $m/z$  65, 81, and 97 are unknown and may possibly be due to the Matrigel membrane.

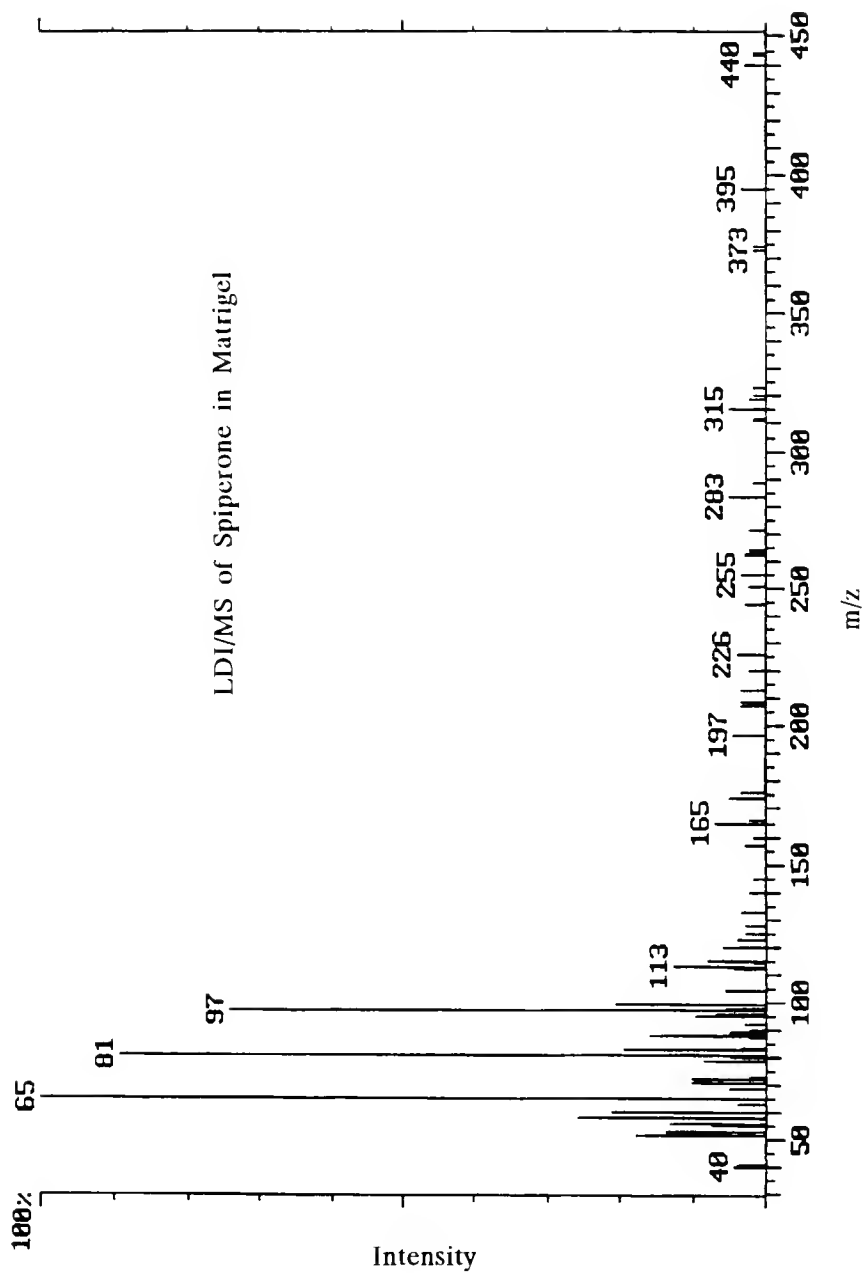


Figure 4-23. LDI mass spectrum of 5  $\mu$ L of spiperone in Matrigel mixture. No UV matrix compounds or TFA were added. The low mass cutoff is 40 u during trapping and storage. The mass spectrum is a single microscan.

### MALDI of Spiperone in Matrigel

In the MALDI/MS spectra of spiperone in Matrigel, very noisy mass spectra were observed initially due to the ion products of the Matrigel membrane. This problem should be expected, but no predominance of spiperone ions, in particular the protonated molecular ion, was seen in the mass spectra from the first few attempts. Even with ejection of the lower mass ions using higher low mass cutoffs, no change in the abundance of spiperone ions was seen. It is possible that the production of spiperone ions is suppressed by the Matrigel, or that the Matrigel neutrals were undergoing charge exchange with any spiperone ions produced by laser desorption. The spiperone-Matrigel mixture is somewhat heterogenous due to the gelatinous characteristics of the membrane tissue and the incomplete mixing of the analyte compound within the tissue. The addition of methanol to the mixture, however, seems to increase the overall solubility of the mixture, thus giving a smoother sample residue more like that of the pure spiperone sample.

New spiperone-Matrigel mixtures were prepared with careful mixing. Specifically, 1 mg of spiperone was mixed into 1 mL of Matrigel membrane immediately after the Matrigel melted from its frozen storage state before it reached room temperature and gelled. To help dissolve the spiperone, 0.1 mL of methanol was added to the mixture. The MALDI mass spectrum of this mixture is shown in Figure 4-24. The spectrum is an average of 20 scans. To obtain the mass spectrum shown, 2  $\mu$ L of the spiperone-Matrigel mixture was deposited on the probe tip and 4  $\mu$ L of a 1 mM sinapinic acid matrix solution added. As seen in the figure, there

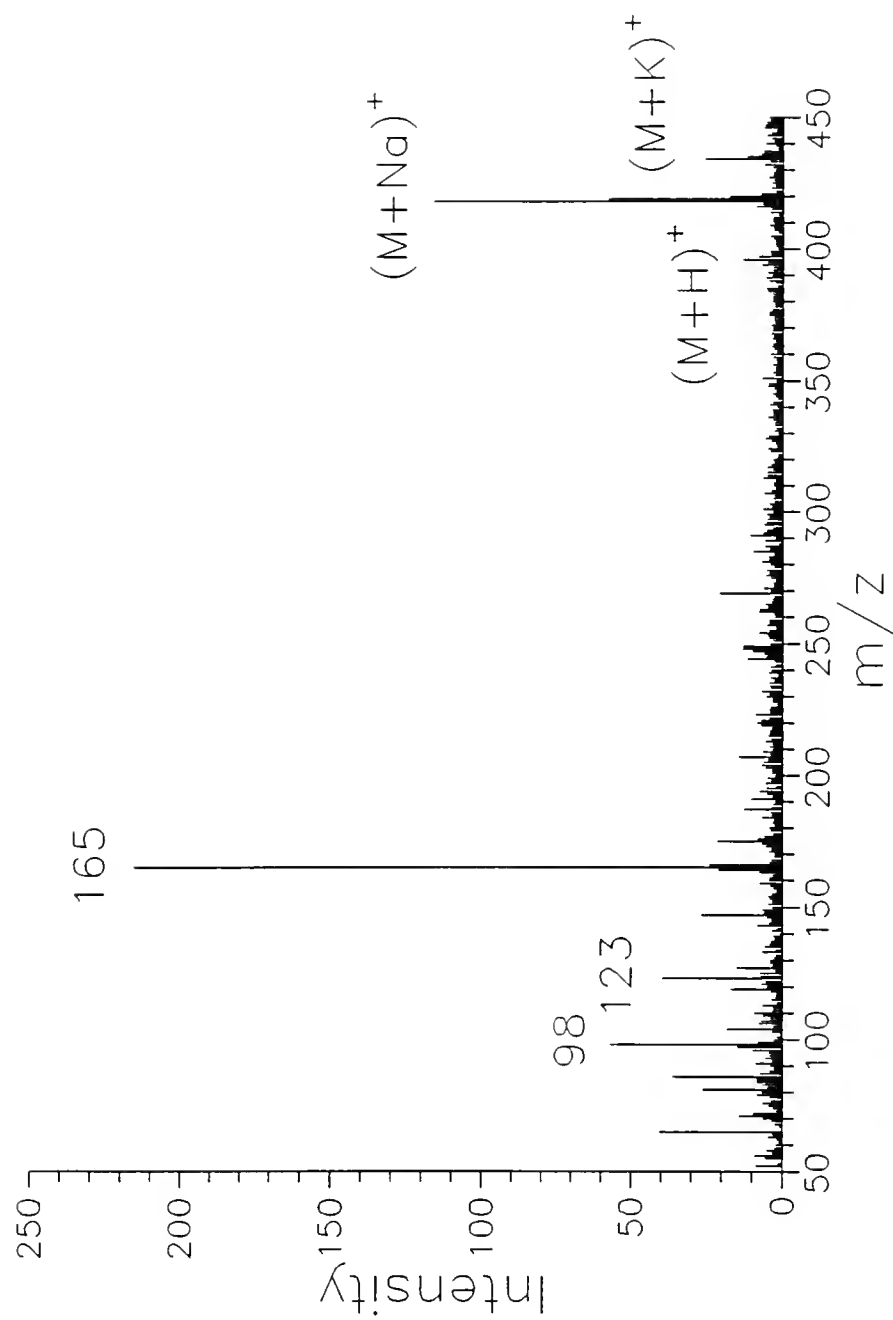


Figure 4-24. MALDI/MS of spiperone in Matrigel (average of 20 scans).

is little production of protonated spiperone; the sodium adduct peak is approximately ten times greater in abundance than the protonated molecular peak. The Matrigel membrane is most likely a large source of sodium to this ionization process. The relatively abundant spiperone fragment ions indicate that the MALDI process is not optimized. The presence of the Matrigel does not permit the isolation of spiperone by the matrix compound alone; instead, the spiperone molecules are surrounded by both matrix molecules and the Matrigel components. This situation is suggested by the spectrum in which both molecular ions and fragment ions of spiperone are seen. The irradiance could not be optimized by reducing it further to eliminate fragmentation because ions were not detected at lower settings. This observation suggests that the laser energy is not as efficiently absorbed as in the experiment using pure spiperone with the matrix compound.

As mentioned above, the sodium adduct at  $m/z$  418 is most probably due to the abundant Na salts in the homogenized natural mouse tissue. This sodium adduct ion could be mass selected for MS/MS instead of the protonated molecule; however, the quality of the daughter spectrum of the sodium adduct ion may not provide sufficient information for ion structure determination due to the possible production of mostly sodium ions from CID of the sodium adduct. Also, the intensity of the sodium adduct may be dependent on the sample.

The addition of Matrigel to the sample also affects the quality of the MS/MS spectra. As shown in Figure 4-25, the protonated spiperone ion is incompletely isolated. Smaller peaks appear throughout the mass range of the scan, presumably

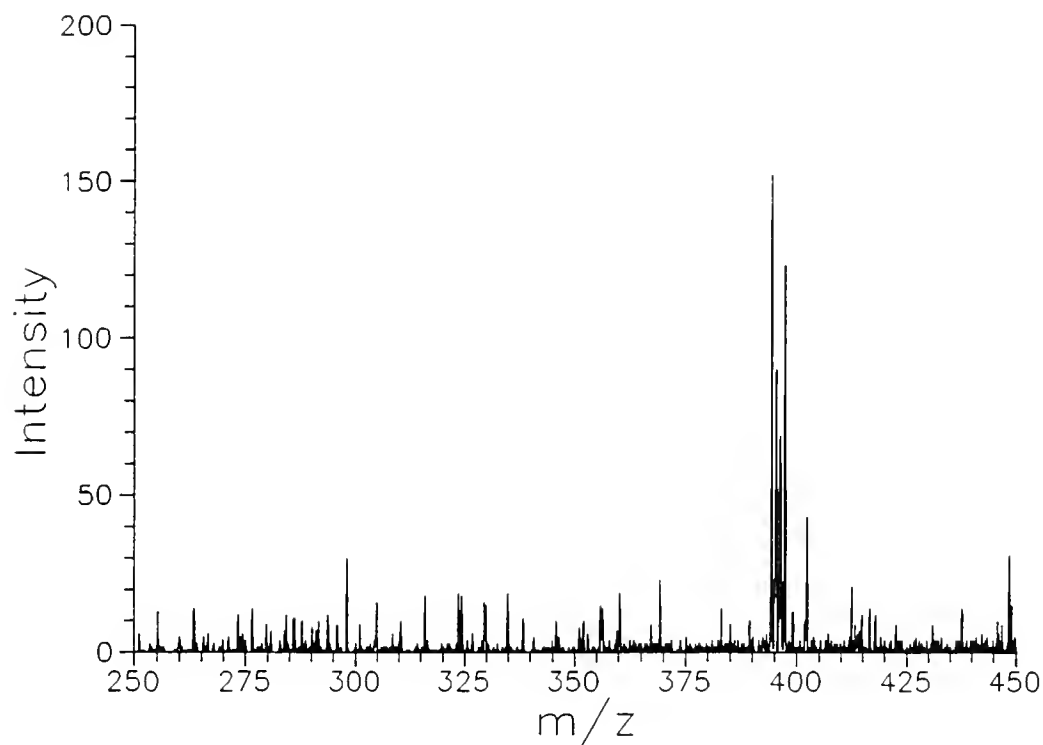


Figure 4-25. MALDI/MS of spiperone in Matrigel using a DHB matrix solution (0.1% TFA). Single ion isolation was attempted for  $m/z$  396. Low mass cutoff is 150 u.

due to ion-molecule reactions between the spiperone ions and late-desorbing neutral species from the sample surface. To obtain this mass spectrum, the  $(M+H)^+$  of spiperone at  $m/z$  396 was isolated using the 2-step isolation method as described previously and listed in Table 4-1. The low mass cutoff for trapping was increased up to 150 u in order to prevent trapping of lower mass ions, but no change was seen in the mass spectra. Increasing the period of the isolation steps until the delayed desorption of neutrals has ceased would remove these additional ions; however, the loss of molecular spiperone ions to these side reactions would still reduce the sensitivity of the method for the analyte. Further research focussed upon eliminating these effects, including the use of an external LDI source with injection of the ions (but not desorbed neutrals) into the trap for analysis, as discussed in the next chapter.

Glish *et al.* also observed extraneous ions in the mass scan after performing the isolation step.<sup>39</sup> No change in the mass spectrum was observed by adding longer storage times, but the appearance of other ions after performing single ion isolation suggested the continued desorption of ions or neutrals for a period after the laser desorption event according to their report. In performing LDI/MS/MS of trimethylphenylammonium chloride, Glish *et al.* observed desorption tens of milliseconds after the laser pulse. This observation was seen in the appearance of ions in the mass range 120 u to 136 u after a 10 ms delay prior to the final mass scan. The extra ions were not observed, however, when the resonant excitation voltage for CID was applied after the ion isolation step. It was believed that the



tickle voltage affected the trapping efficiency of the desorbed ions, but no further explanation was provided.

### Conclusions

In summary, LDI and MALDI were demonstrated in the quadrupole ion trap mass spectrometer for several samples including spiperone, spiperone in Matrigel membrane mixture, trimethylphenylammonium chloride, and several matrix compounds. The MS/MS capability of the ion trap was also demonstrated on laser-desorbed ions. It was shown to provide clean and informative spectra of compounds which gave complicated or noisy spectra from MALDI. Positive and negative ion spectra were obtained on the ion trap from LDI of sodium iodide. MALDI was evaluated for use with the ion trap mass spectrometer and for use in increasing the production of molecular spiperone ions. For pure spiperone samples, MALDI produced abundant protonated spiperone ions which were not seen in the non matrix enhanced samples. MALDI also increased the length of the ion signal overall in comparison to LDI.

Laser irradiance was found to be the most important parameter to control for obtaining good MALDI spectra of spiperone samples. The lowest sample amount used for detection of spiperone was 74 ng. The total sample used to obtain the MALDI mass spectra was 1.4 ng. MALDI was also performed on leucine enkephalin. The mass spectra showed the sporadic appearance of adduct ions from the addition of preformed alkali metal ions to the desorbed neutral molecules.

Laser desorption mass spectra were obtained from spiperone in Matrigel mixtures. For LDI, no molecular ion for spiperone was detected, but the fragment ion at  $m/z$  165 was seen. For MALDI, the protonated spiperone was detected but adduct ions were also seen in even greater abundance due to the sodium dissolved in the Matrigel membrane.

The results obtained for LDI and MALDI on the quadrupole ion trap are promising for this new approach, and current and future research will address increasing the sensitivity of the method. The results obtained using the internal ionization configuration, particularly the appearance of extraneous ions after the MS/MS isolation step and the reduced trapping efficiency of ions formed at the ring electrode surface, suggest the use of an external ionization laser desorption system. In the next chapter, the results from studies using an external laser desorption ionization system will be presented.

## CHAPTER 5

### LASER DESORPTION IONIZATION/QUADRUPOLE ION TRAP MASS SPECTROMETRY USING AN EXTERNAL SOURCE CONFIGURATION

This chapter describes the results obtained using an external laser desorption ionization source with injection of the ions into the quadrupole ion trap mass spectrometer. The purposes of using such a configuration are several. In order to perform laser microscopy, the focussing lens ideally should be placed close to the sample surface (about a centimeter) to obtain the necessary spatial resolution of 1  $\mu\text{m}$  and to permit visualization of the sample at adequate magnification. This spacing cannot be achieved with the internal source configuration. With the external source configuration, supplementary ionization, specifically chemical ionization, of laser-desorbed neutrals can be performed.<sup>1,28</sup> The reagent gas pressure within the ion trap cannot be increased high enough in the internal configuration (e.g., 1 torr of methane) yet maintain the required conditions for mass analysis. With the source region separated from the trap, the reagent gas pressure can be maintained at optimum levels, with the ion trap region can be differentially pumped to maintain a lower operating pressure. While Perchalski *et al.* used LD/CI to lengthen the ion pulse so that the triple quadrupole mass spectrometer could be scanned across the ion pulse,<sup>1</sup> this longer ion pulse is not necessary since the ion trap is a storage device and can trap all ions produced from the laser pulse regardless of the ion pulse

length. Rather, the purpose for performing chemical ionization on laser-desorbed neutrals with the ion trap is to achieve greater sensitivity. It is generally believed that under laser desorption conditions the efficiency of ionization is small; only about 1 out of 1000 molecules are desorbed from the sample surface as an ion. Therefore, if chemical ionization could be used to ionize the laser-desorbed neutrals which are in much greater amount, then the number of analyte ions produced should increase significantly, as should the sensitivity. Furthermore, chemical ionization will produce protonated analyte molecules, which should be more amenable to fragmentation by CID than are such adduct ions as  $[M+Na]^+$  often produced by MALDI. An external ion source would also eliminate the presence of late-desorbing neutrals during the MS/MS process, as was seen for the internal configuration in Figure 4-25.

Ions produced in an externally located source can be focussed in their trajectories into the ion trap for better trapping using the ion injection lenses. A disadvantage to this method, however, is ion transmission loss with the ion injection system which are not involved in the internal configuration method. However, with the internal method, the overall trapping efficiency was believed to be low due to the position of ion formation at the edge of the trap volume and high initial ion velocities. As with the internal configuration, selective trapping of ions can be performed with the external source configuration to remove matrix ions from the trap.

### Laser Beam/Ion Axis Placement

The positioning of the sample surface on axis with the ion injection system, as well on axis with the laser beam, is an important consideration for focussing capability and sensitivity. In our current configuration, the sample surface is at a  $45^\circ$  angle to both the ion axis and the laser beam. The ion axis and the laser beam axis are  $90^\circ$  to each other, as seen in Figure 5-1. In the LAMMA instruments which perform laser microscopy, the LAMMA 500 used a backside approach where the laser beam was on-axis with the ion path with a thin sample between them. In the LAMMA 1000, the laser beam axis was at a  $45^\circ$  angle to the sample surface and the ion path was perpendicular to the sample surface. In both instruments, the laser beam axis, as well as the focussing lenses used, were also the axis and lenses used for microscopic viewing of the sample by the operator for targeting of sampling sites. Of the various configurations, it is believed that the sample surface should be perpendicular to the ion axis because the angle of the ion plume from LDI is also perpendicular to the sample surface. Having the plume in line with the ion axis should provide the most efficient collection of ions from optimum transmission through the initial extraction lens and through the injection system.

For introduction of ions into the trap, injection can be performed through the ring electrode, the endcap electrode, or asymptotically between the ring and endcap electrodes. O and Schuessler demonstrated with simulation that injection through the endcap is more favorable than through the ring electrode.<sup>49</sup> They also determined that injection through the gaps between the electrodes is not feasible

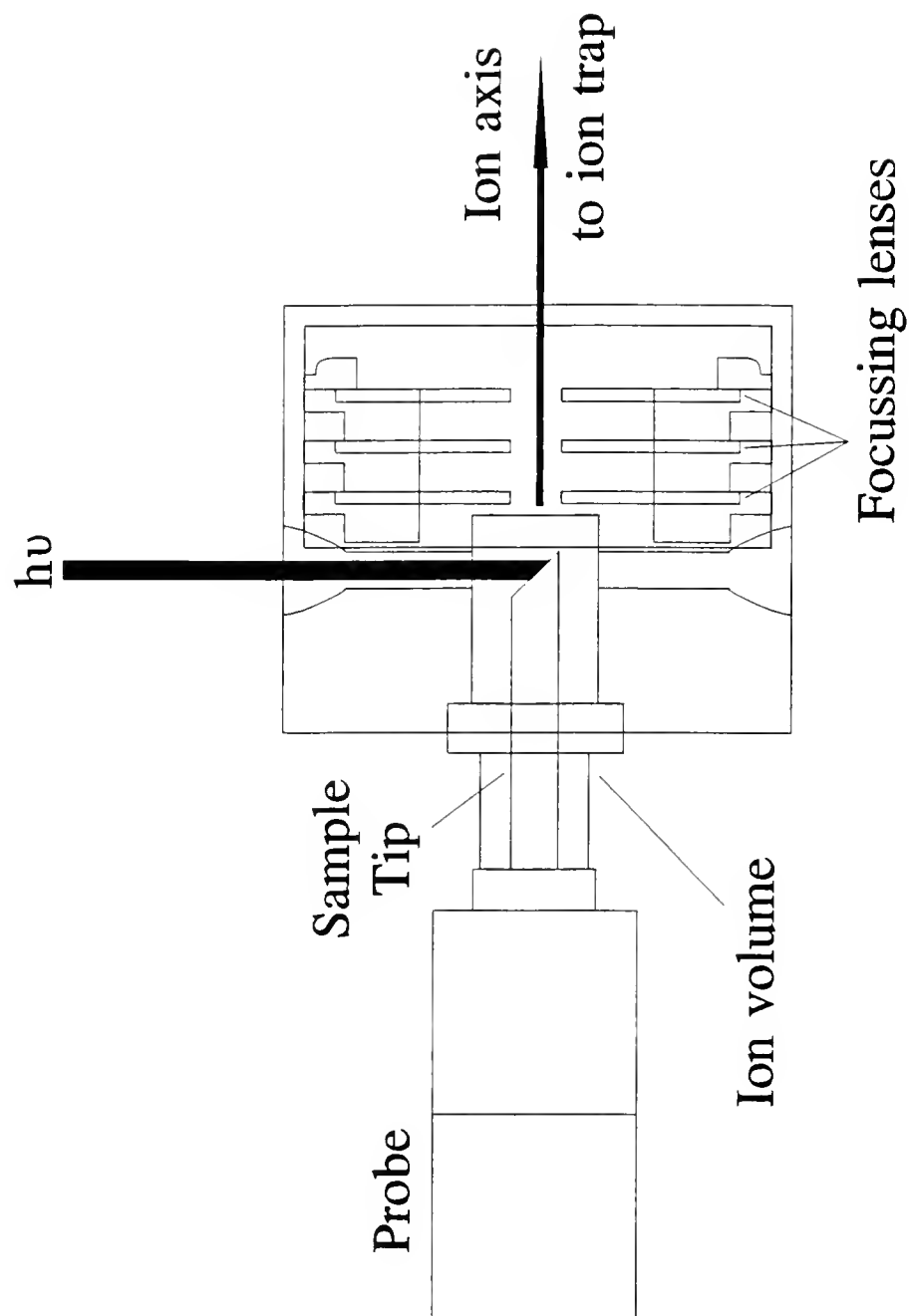


Figure 5-1. Drawing of laser and sample probe tip introduction to external source.

without collisions because ions require substantial kinetic energies to transverse the small gap without striking an electrode. These same studies also showed that trapping is most favorable for ions of low energy and large incidence angle. Because of the relatively high pressure of helium used in the trap, trapping injected ions by removing energy through collisions is possible for all configurations. Initial position and velocity of the ion, as well as the parameters of operation of the trap (e.g.,  $q_z$ ), determine whether the ion will remain within the field boundaries.

### Instrumental Description

To perform LDI externally to the trap, a modified Finnigan ITS40<sup>TM</sup> was used. This instrument is configured inside a cradle-type vacuum chamber to allow easy access to the ion trap assembly and ion injection system. As seen in Figure 5-2, the nitrogen laser is situated outside the vacuum manifold and the laser beam is diverted 90° through a quartz window similar to the internal configuration. The laser beam is passed through the focussing lens and neutral density filters which are usually placed between the aiming mirror and the vacuum window. Instead of entering the ion trap, the laser beam is directed into the gas chromatography (GC) port of a Finnigan 4500<sup>TM</sup> ion source. The 0.10 inch diameter port leads to the ion volume GC inlet hole. A solids probe type ion volume is used so that a LDI sample probe tip may be inserted, as shown in Figure 5-1. As described previously, the laser beam impinges the sample surface at a 45° angle. The ion axis is at a 90° angle to the laser beam.

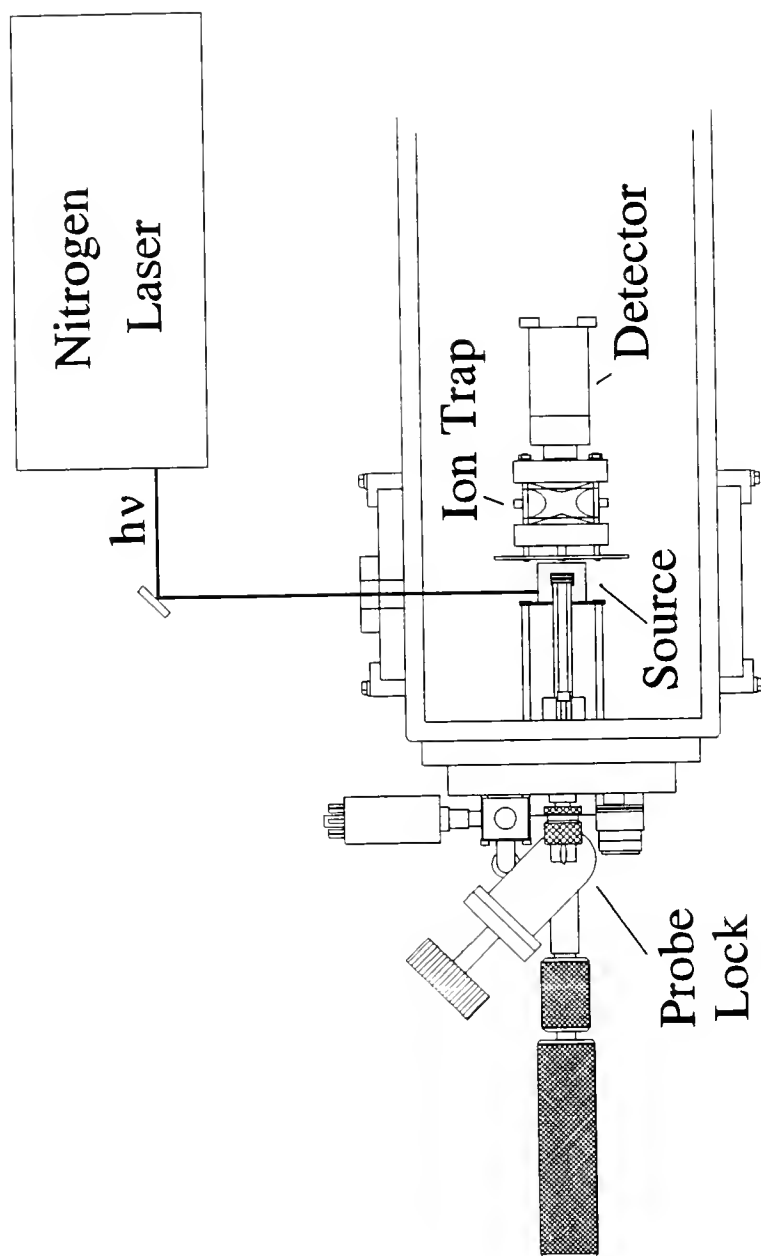


Figure 5-2. Schematic of external source configuration for laser desorption ionization/quadrupole ion trap mass spectrometer.



The ion injection system utilizes three focussing lenses, a tube lens, and a gate lens to pass the ions from the ion volume to the ion trap through the endcap electrode where the filament assembly would normally be located. The filament assembly of the ion source is left intact and is used for conventional mass calibration (e.g., EI of polyfluorotributylamine). The instrument operates using the standard ITS40 software, although customized software developed in our laboratory was also used for triggering and modified scan functions. Sample preparation and scan functions are the same as those described for the internal source configuration method and discussed in Chapter 2.

With the ITS40 instrument, several additions to the electronics were needed in order to properly time the laser pulse with the ion gate and to perform resonant excitation for  $MS^n$  studies. A block diagram of the function generators used and how they are connected is given in Figure 5-3. Only two triggers were available for use with the modified ITS40 software. The first trigger was utilized for both the ion gate and the laser pulse. The second trigger was utilized to activate an arbitrary waveform generator (Stanford Research Systems Model DS345) to provide the resonant excitation signal for CID. Unfortunately, when the first trigger was used for both the ion gate and the laser pulse, the nitrogen laser triggered before the ion gate opened. Ions produced by the laser pulse were deflected from the trap because the ion gate was still in a closed position (+60 V on the gate lens). To rectify this problem, a 1 ms time delay was introduced to the trigger signal sent to the laser using a function generator (Wavetek Model 275), as shown in Figure 5-3. Also, the

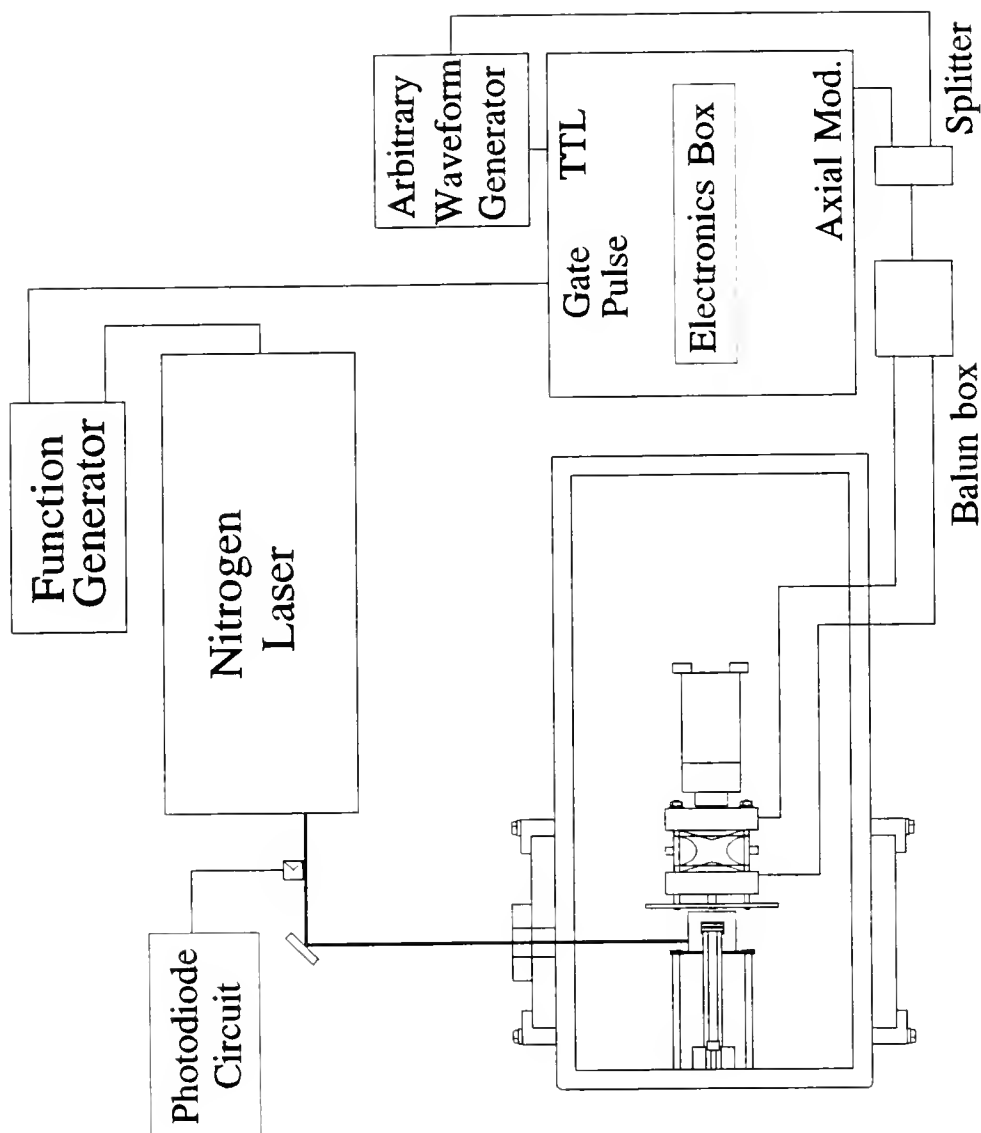


Figure 5-3. Schematic of laser desorption external ionization ion trap showing the configuration of components for delayed laser triggering and resonant excitation.

laser trigger was not synchronized with the rf phase angle as in the internal configuration because the ion injection period was much longer than the ion pulse for the internal configuration.

As mentioned, the second software-controlled trigger was utilized to pulse the arbitrary waveform generator to provide the predefined signal for resonant excitation in MS<sup>n</sup> experiments and for axial modulation in mass range extension experiments. As seen in Figure 5-3, the second trigger (TTL) is sent to the arbitrary waveform generator, the output of which is combined with the axial modulation signal (475 kHz) from the ITS40 electronics using a radiofrequency signal splitter. The combined signals are then passed through a balun box to produce two complimentary signals 180° out of phase. Each of these signals is then placed on a different endcap electrode. The two triggers, radiofrequency signals, ion gate, and laser pulse were compared on a digital storage oscilloscope (LeCroy 9400) for synchronization and accuracy. To detect the laser pulse, an amplified silicon photodiode was placed in the beam path, as shown in Figure 5-3.

### Laser Desorption Ionization

High abundances of ions were obtained from LDI of trimethylphenylammonium bromide samples. In fact, space charge conditions existed at higher helium buffer gas pressures ( $> 1 \times 10^{-5}$  torr ion gauge reading) from the trapping of too many ions. This space charge condition could be seen in the unresolved TMPA fragment ion peaks at  $m/z$  120 and 121. Obtaining resolved peaks

was the first goal when applying this external source. This goal was achieved by limiting the number of ions trapped during ion injection by reducing the buffer gas pressure, and by reducing the number of ions produced by reducing the laser energy transmission to the sample surface. With the helium buffer gas introduced directly into the ion trap volume, the buffer gas pressure was typically optimized to a value of  $8 \times 10^{-6}$  torr (ion gauge reading). During all experiments, the vacuum manifold was at room temperature. The laser energy transmission was reduced using two different methods. These methods include the defocussing of the laser beam and the placement of neutral density filters in the beam path between laser and the aiming mirror.

The ion injection lens voltages and the ion source voltages (all relative to the grounded ion trap endcap electrodes) were optimized for LDI. Optimum injection and source voltages were approximately equal to the optimum voltages obtained for EI. The ion gate open setting was -30 V and the closed setting was +60 V. Lens 1 (extraction lens) was set to -46 V, lens 2 to -10 V, and lens 3 to -10 V. The ion source offset voltage was set to +4.3 V. A conversion dynode was used and set to -2 kV. The electron multiplier was set to -1400 V. All voltages were optimized by observing the laser-desorbed ion signal response during mass analysis.

### Low Mass Cutoff

A study of the effect of low mass cutoff during injection and trapping of laser-desorbed TMPA ions was performed. The mass spectrum from LDI/MS of TMPA

using the external source is given in Figure 5-4 for a low mass cutoff setting of 10 u. The mass spectrum is an average of scans #5 through #20. In this spectrum, the base peak at  $m/z$  136 is the molecular ion. The next largest peak is at  $m/z$  121 for the methyl loss fragment ion. The ion peak at  $m/z$  197 is produced from a substitution of a hydrogen on the  $121^+$  phenyl group with another phenyl group to give  $(\text{CH}_3)_2\text{N}-\phi-\phi^+$ .

A plot of the TMPA ion intensities at  $m/z$  120, 121, and 136 versus low mass cutoff during trapping and storage gives the results shown in Figure 5-5. In this plot, we see a maximum for  $m/z$  136 molecular ion at a low mass cutoff of 15 u. The most abundant ion then becomes the  $m/z$  121 fragment which attains its maximum at a low mass cutoff of 25 u. This ion is then replaced by the  $m/z$  120 ion fragment which maximizes at a low mass cutoff of 40 u. All ions, therefore, are seen to increase with increasing low mass cutoff followed by a steady decrease in intensity. This process occurs with decreasing ion mass for increasing low mass cutoff. Initially, the result shown here is contrary to what is expected for ion injection experiments. Based on a pseudopotential well depth model,<sup>45</sup> the low mass cutoff at which the maximum ion intensity occurs should increase with increasing ion mass, opposite to what is seen in Figure 5-5. However, the results obtained in this experiment are easily understood considering that the ion at  $m/z$  121 is produced by the loss of a methyl group from  $136^+$  ion, while the ion at  $m/z$  120 is produced directly by the further loss of a hydrogen from the  $121^+$  ion ( $136^+ \rightarrow 121^+ \rightarrow 120^+$ ), as has been shown with  $\text{MS}^n$  analysis.<sup>40</sup> This fragmentation process is increased by the increasing amplitude of the

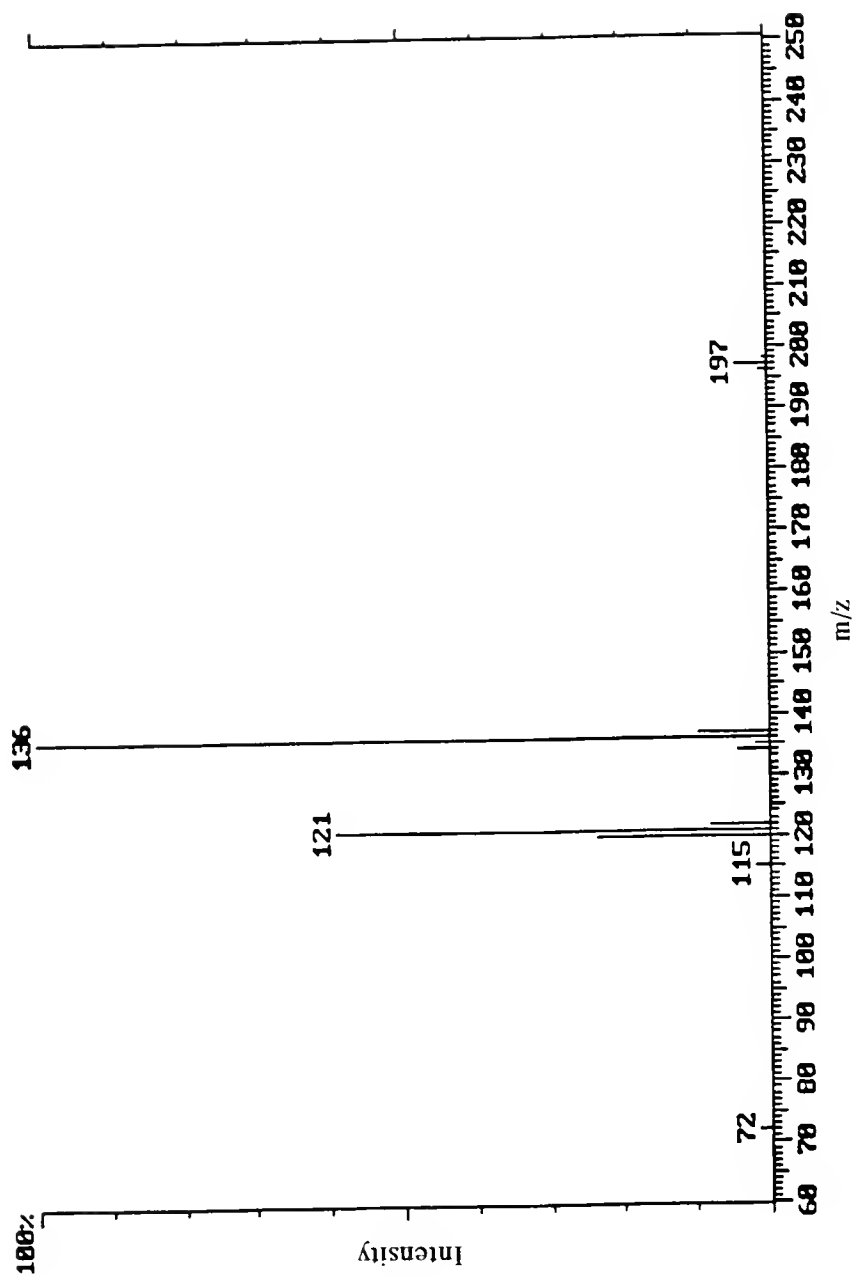


Figure 5-4. LDI/MS mass spectrum of trimethylphenylammonium bromide. Low mass cutoff is 10 u. Average of scans #5 thru #20.

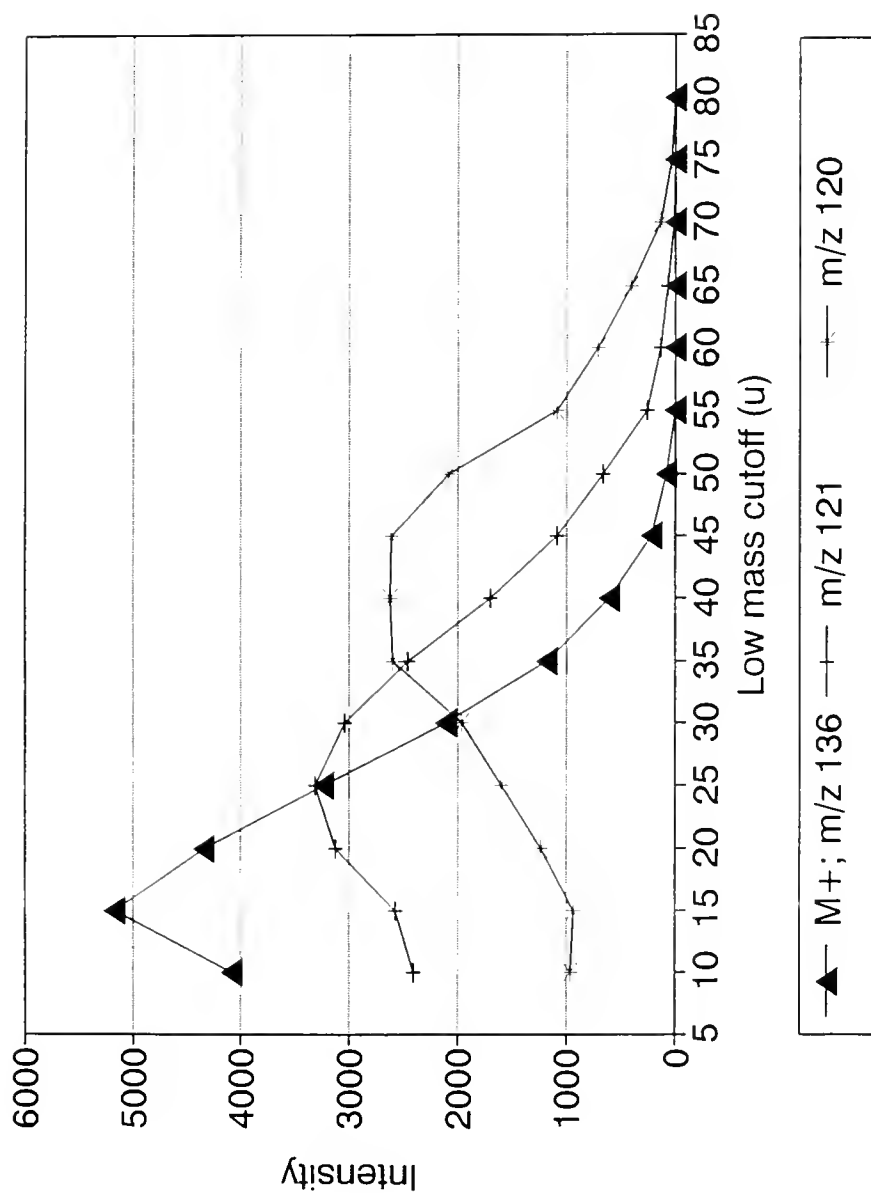


Figure 5-5. Plot of trimethylphenylammonium bromide ion intensities versus low mass cutoff for trapping and storage. Each data point is an average of the ion intensity from scan #5 thru #20.

rf trapping field with increasing low mass cutoff (similar to resonant excitation when used for collision-induced dissociation). This effect is shown by the plot of  $120^+/121^+$  intensity ratios versus low mass cutoff, as in Figure 5-6. The ion intensity ratio increases steadily with increasing low mass cutoff indicating that the greater the amplitude of the trapping field, the greater the amount of energy deposited into the injected ion and thus the greater the extent of fragmentation. Low mass cutoff during trapping, therefore, is an important consideration for determining the optimum trapping of externally produced laser-desorbed ions. The low mass cutoff should be optimized for most efficient trapping and least fragmentation of the analyte ion.

### Laser Irradiance

Using the external source, effect of laser irradiance on ion production from LDI of trimethylphenylammonium bromide was studied. As seen in Figure 5-7 for the TPA ions at  $m/z$  136, 121, and 120, increasing the percent transmission of the laser energy increases the number of ions produced. This result demonstrates that ion production from laser desorption is related to the amount of laser energy absorbed by the sample and is not exclusively controlled by the ion injection process.

### $MS^3$ of Trimethylphenylammonium Bromide

To evaluate the tandem mass spectrometry setup described earlier and displayed in Figure 5-3, LDI/MS/MS and  $MS^3$  was performed on TPA. In Figure



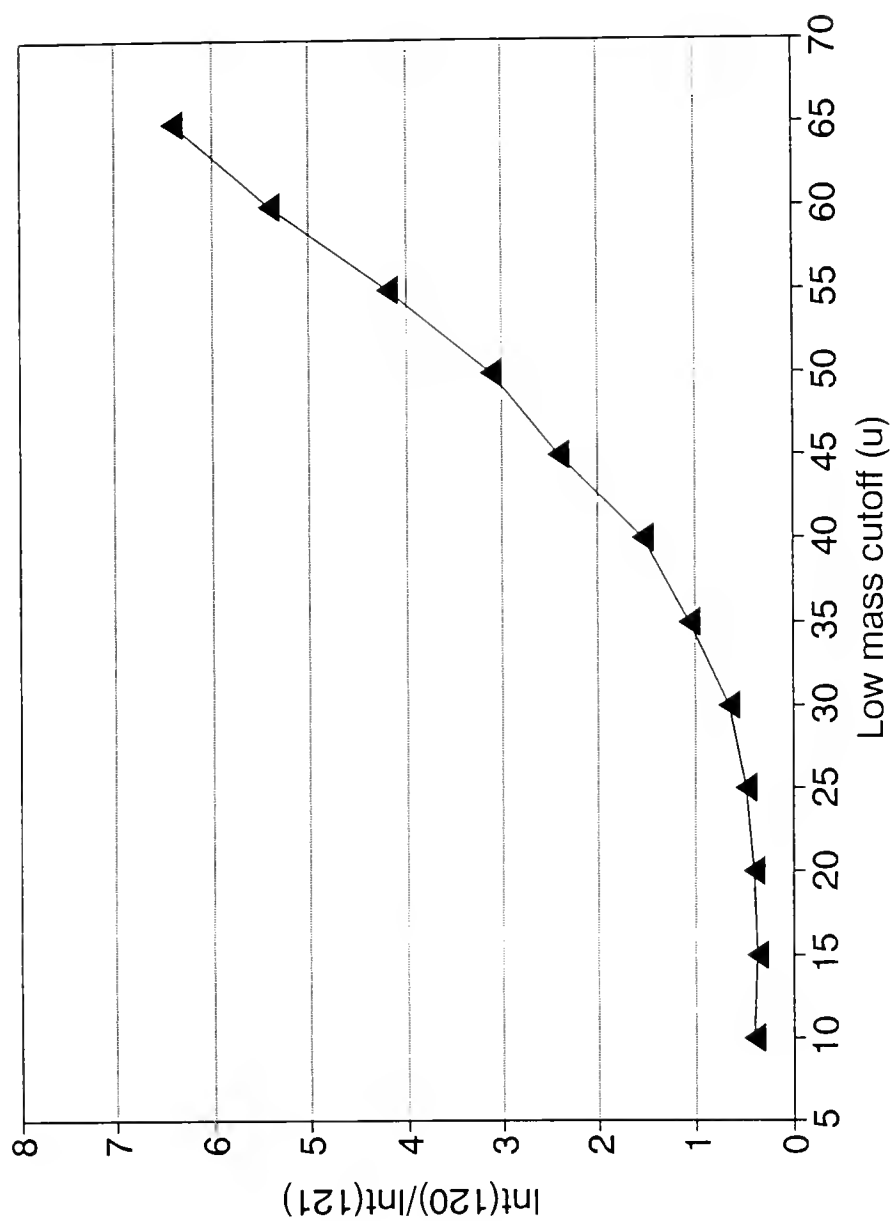


Figure 5-6. Plot of trimethylphenylammonium bromide  $120^+/121^+$  ion intensity ratio versus low mass cutoff for trapping and storage. Each data point is an average of the ion intensity from scan #5 thru #20.

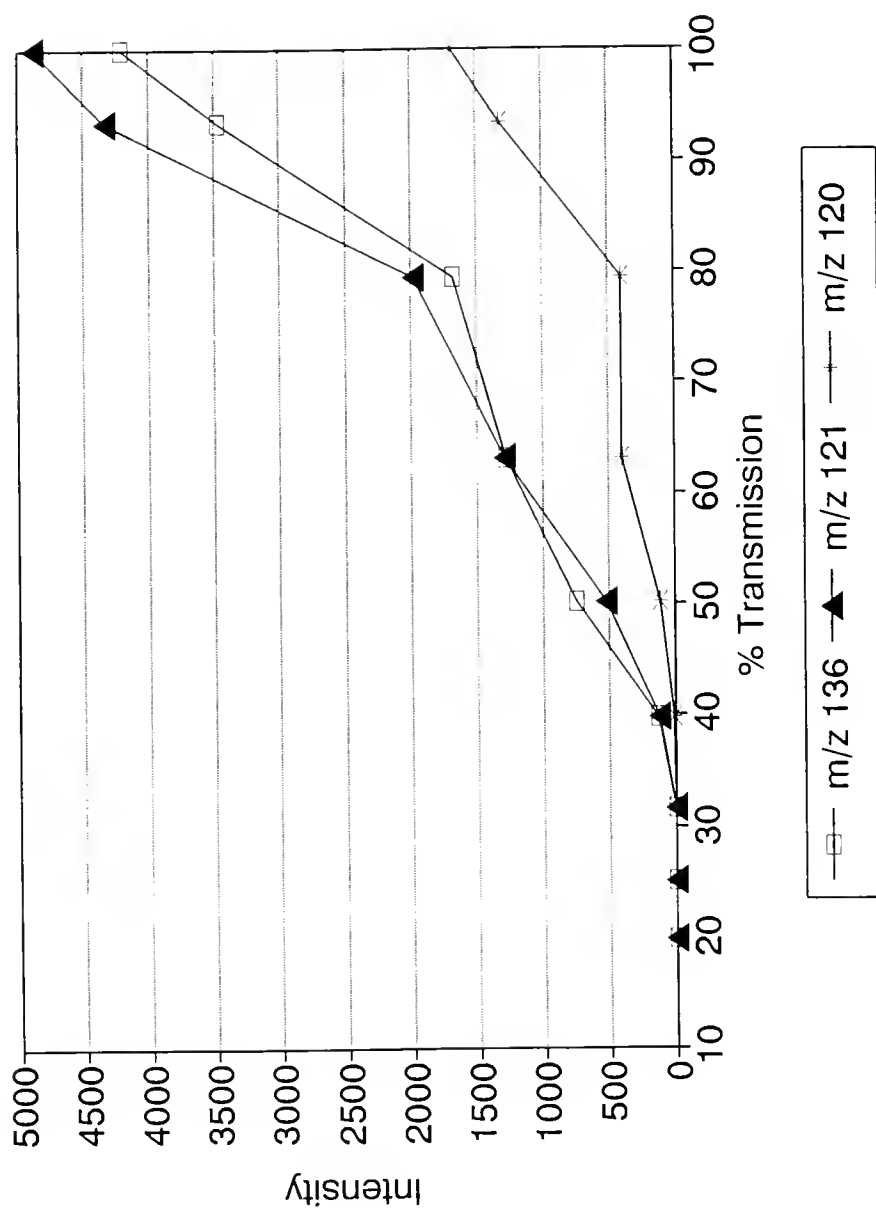


Figure 5-7. Plot of trimethylphenylammonium bromide ion intensities versus laser energy % transmission. Each data point is an average of the ion intensity from scan #5 thru #20.

5-8a, the mass spectrum from LDI/MS/MS of the TMPA molecular cation is given. The base peak in the daughter spectrum of  $m/z$  136 is at  $m/z$  121 with small peaks seen at  $m/z$  120 and 122. By performing LDI/MS<sup>3</sup>, which includes the isolation and fragmentation of the 121<sup>+</sup> ion, we obtain the granddaughter mass spectrum shown in Figure 5-8b. An ion that is missing from this mass spectrum is the 120<sup>+</sup> ion which should be a product from the fragmentation of the ion at  $m/z$  121. However, resonant excitation conditions may have been strong enough to excite or eject not only  $m/z$  121 but also any 120<sup>+</sup> ions produced, as suggested by the lack of peaks between  $m/z$  119 and 122.

#### Matrix-Assisted Laser Desorption Ionization

MALDI was performed inside the external source using the same sample preparation and laser optimization procedures as for the internal ionization method described in Chapter 4. Whereas the laser energy was reduced by 5 - 10% using neutral density filters to obtain the best MALDI spectra on the internal system, it was observed on the external instrument that good MALDI spectra were obtained with little or no reduction of laser transmission. Typically, the laser transmission was set to 80 - 100%. The restrictive geometry of the GC port of the ion source (an approximately 0.5 inch tunnel with a 0.1 inch diameter) reduces the amount of laser radiation reaching the sample surface by acting as an aperture. Proper alignment of the beam was not possible using visual inspection of the probe tip surface while the

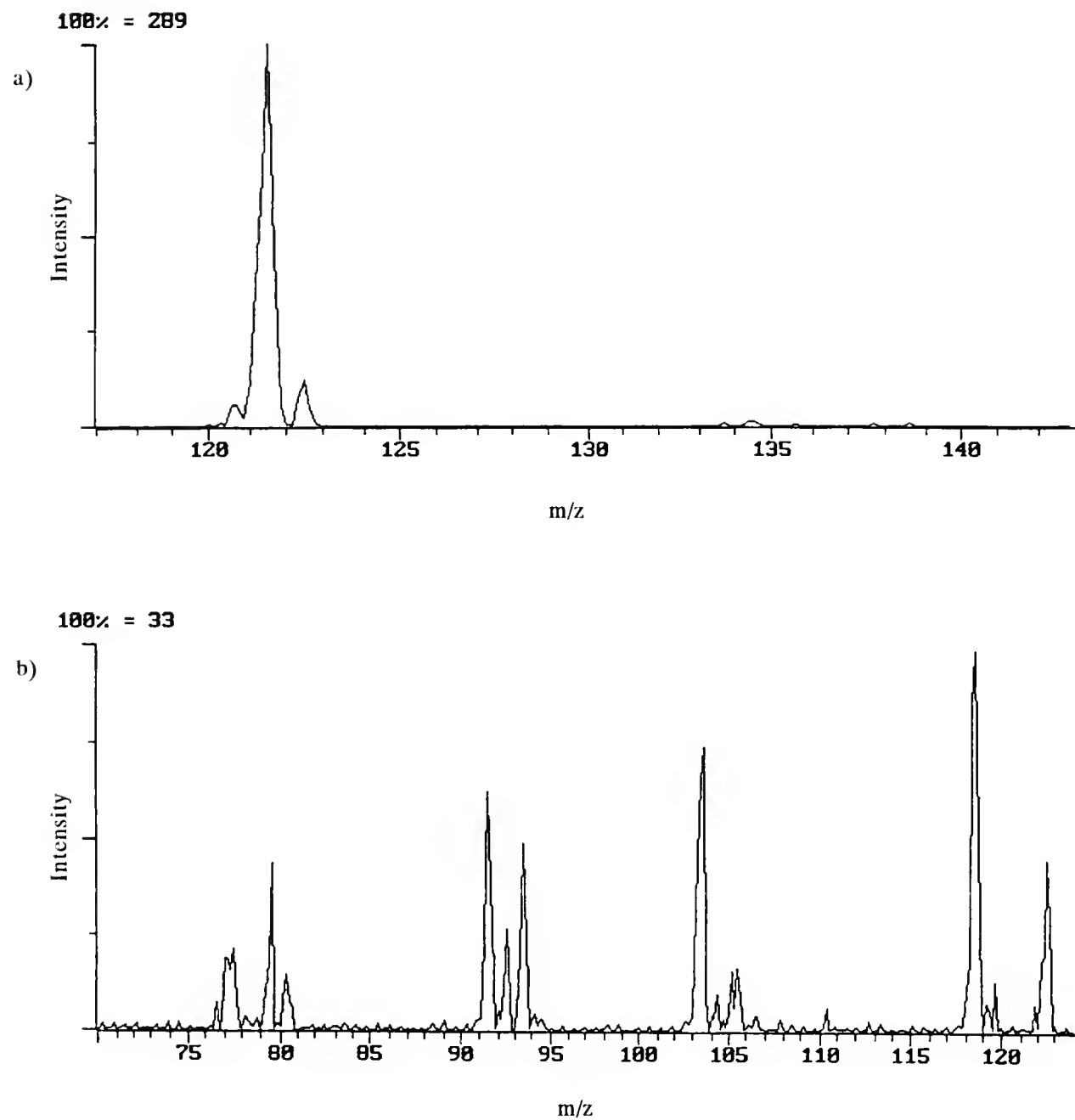


Figure 5-8. LDI mass spectra of trimethylphenylammonium bromide: a) MS/MS of molecular ion at m/z 136, b) MS/MS/MS of molecular ion (136<sup>+</sup> → 121<sup>+</sup> → fragments).

tip was in place. Therefore, the laser beam was finely aimed by observing the resultant ion signal detected with the ion trap mass spectrometer.

### MALDI of Spiperone

Matrix-assisted laser desorption ionization was performed on 1  $\mu\text{L}$  of a 47  $\mu\text{M}$  spiperone solution in methanol. This amount corresponds to a total spiperone loading of 18 ng on the probe tip surface. The sample was mixed on the probe tip surface with 1  $\mu\text{L}$  of a 520 mM 2,5-dihydroxybenzoic acid (DHB) matrix solution (0.1% TFA). The resultant mass spectrum, shown in Figure 5-9, includes a peak at  $m/z$  396 for protonated spiperone that is the largest in the mass range scanned (40 to 650 u). A peak at  $m/z$  397 is for the  $^{13}\text{C}$  ions. No higher mass ions were detected. In the lower mass range, no spiperone fragment ions were detected and only small peaks for the matrix ions were seen. With the external source, obtaining good MALDI spectra was found to be much easier than with the internal method. The external source method gave protonated spiperone signals that were much easier to obtain and optimize, and much longer lasting than for internal configuration.

The ion intensity of protonated spiperone from MALDI/MS versus scan is shown in Figure 5-10 for an equal sample loading as described above (18 ng). The signal obtained for protonated spiperone decays steadily over several laser pulses as expected, but overall the signal lifetime was observed to be longer and less sporadic for the external method than for the internal method. The measurement of zero intensity for protonated spiperone that occurs at scan #1 is an artifact of the

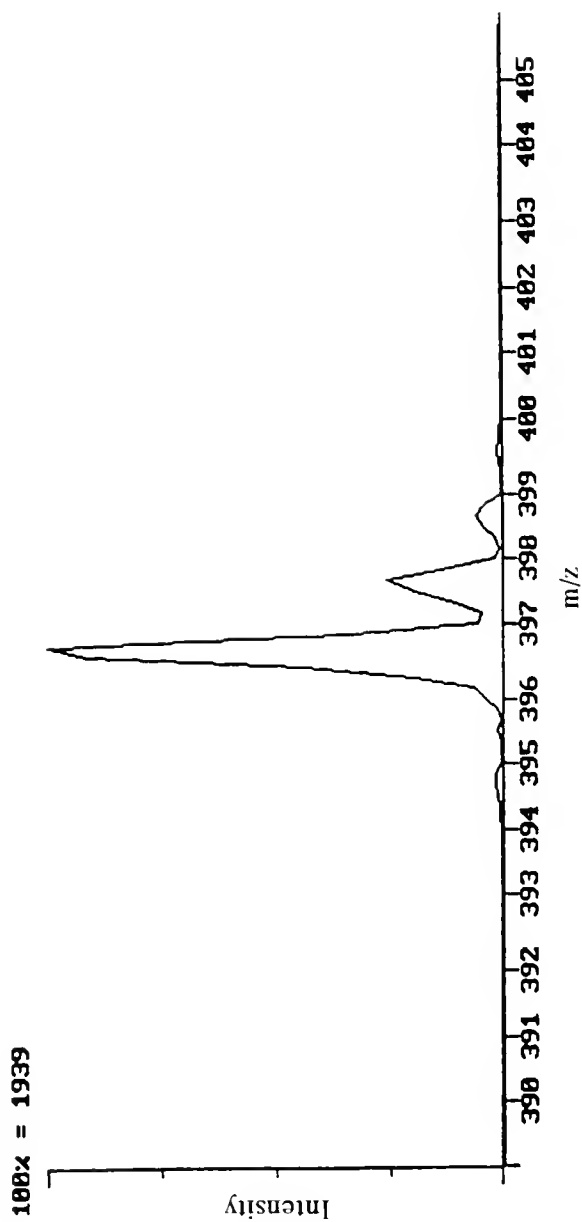


Figure 5-9. Matrix-assisted laser desorption ionization mass spectrum of spiperone using external configuration. Average of 10 microscans. 1  $\mu$ L of 47  $\mu$ M spiperone in methanol sample mixed with 1  $\mu$ L of 520 mM DHB matrix solution.

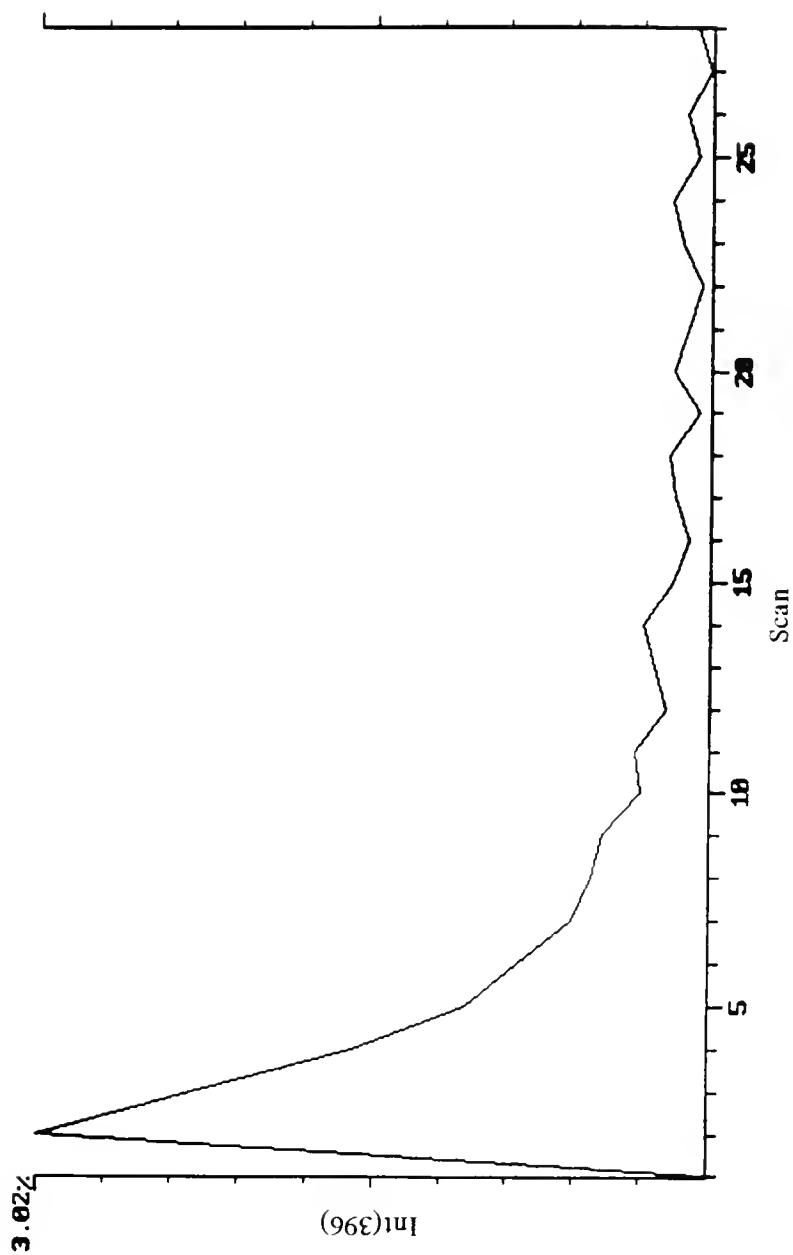


Figure 5-10. Ion intensity of protonated spiperone,  $m/z$  396, from MALDI/MS versus scan for external source configuration.

instrumentation software. If the same laser desorption and sample conditions could be maintained, the ion production should be equal whether the ions are produced in the trap itself or in the external ion source. Upon preliminary observations, however, the external source method demonstrates longer lasting, steadier signals and better potential for further development than the internal source method.

MS/MS results using the external source were similar to those obtained using the internal method. In Figure 5-11, the daughter spectrum of protonated spiperone is given for a sample loading of 18 ng. The resonant excitation frequency for CID is 113 kHz and the amplitude is 6 V (peak-to-peak). These parameters were optimized by varying them on the arbitrary function generator and observing the mass spectral results in real time. The daughter ion spectrum obtained by this MS/MS experiment, where the  $q_z$  value during CID was 0.3, is similar to those obtained with the internal ionization instrument. The same daughter ions of protonated spiperone,  $m/z$  165, 232, 262, and 292 are observed. In both instruments, the  $m/z$  165 daughter ion was the most abundant. The intensity ratios for the other daughter ions varied  $\pm 20\%$ .

#### MALDI of Spiperone in Matrigel

In the preliminary results from analysis of spiperone in Matrigel samples using the external source, little or no protonated spiperone was detected. The instrumental setup used a glass rod target placed in the GC port of the external source to assist in aiming the beam by spotting the laser fluorescence. This glass rod



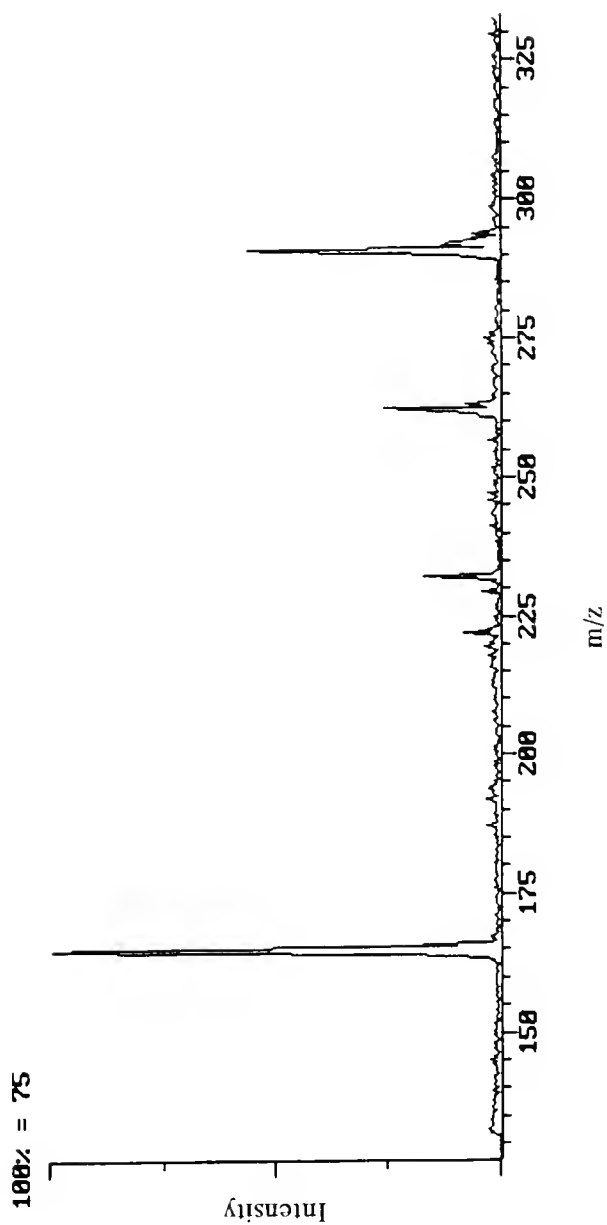


Figure 5-11. MALDI/MS/MS daughter spectrum of protonated spiperone,  $m/z$  396, using external source configuration. Average of 10 microscans. 1  $\mu\text{L}$  of 47  $\mu\text{M}$  spiperone in methanol sample mixed with 1  $\mu\text{L}$  of 520 mM DHB matrix solution. Resonant excitation frequency is 113 kHz and amplitude is 6 V (p-p).

was reducing and distorting the focussing of the laser so that the laser irradiance at the sampling spot was insufficient to produce any ions from the spiperone/Matrigel sample. As stated in Chapter 4, the Matrigel mixture requires larger laser irradiances than used for pure spiperone samples because the absorption of energy is not as efficient as in pure MALDI sample compositions. The glass target was removed, therefore, to increase the laser beam transmission and ions were obtained from the Matrigel samples.

In Figure 5-12, the MALDI/MS mass spectrum of spiperone in Matrigel membrane is given. To obtain this spectrum, 2  $\mu\text{L}$  of a 0.5 mg spiperone/mL of Matrigel membrane was mixed with 2  $\mu\text{L}$  of a 520 mM DHB matrix solution (0.1% TFA). Peaks at  $m/z$  396 and 418 were seen for protonated spiperone and the sodium adduct, respectively. The potassium adduct at  $m/z$  434 was not detected. In the low mass range, several peaks were observed, probably due to the Matrigel membrane. No ions were detected above  $m/z$  450.

Similar to the results from the pure spiperone sample, it was observed that the protonated spiperone signal for the spiperone in Matrigel sample has a longer lifetime than ever observed using the internal ionization method. A plot of spiperone ion intensity versus scan is given in Figure 5-13 for 2  $\mu\text{L}$  of the 0.5 mg spiperone/mL Matrigel membrane sample described earlier combined with 2  $\mu\text{L}$  of the 520 mM DHB matrix solution. While the signal pattern is similar to that shown for the pure spiperone sample, protonated spiperone signals of more than 3 or 4 scans were never obtained from a single sampling spot using the internal

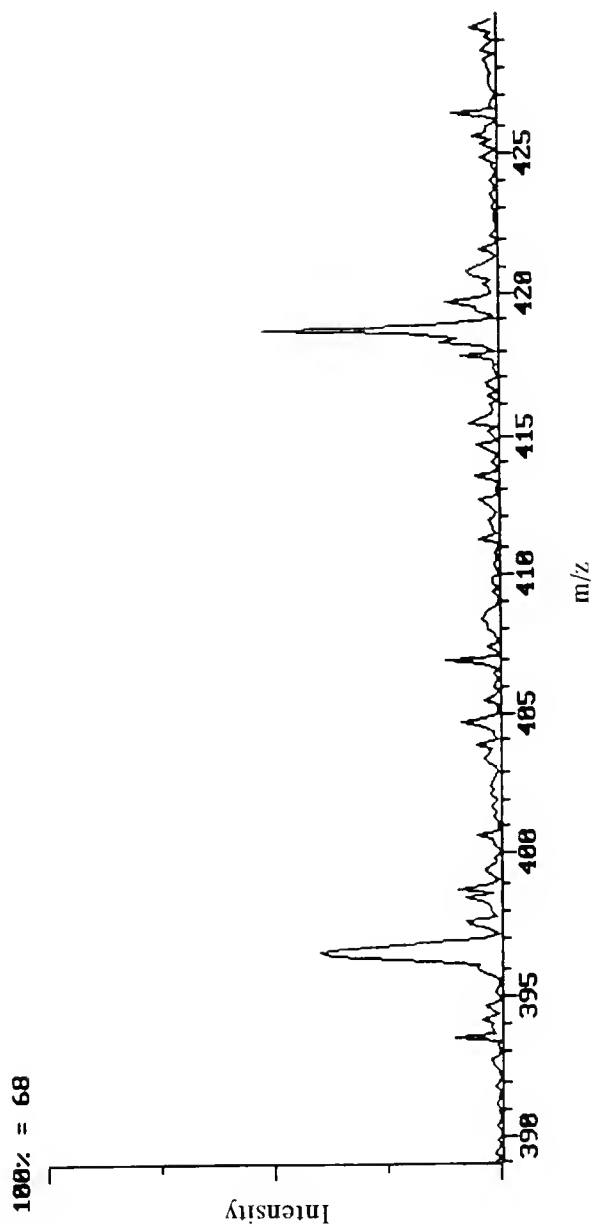


Figure 5-12. MALDI/MS mass spectrum of spiperone in Matrigel membrane. Average of 10 microscans. 2  $\mu$ L of 0.5 mg/mL of spiperone in Matrigel sample mixed with 2  $\mu$ L of 520 mM DHB matrix solution.

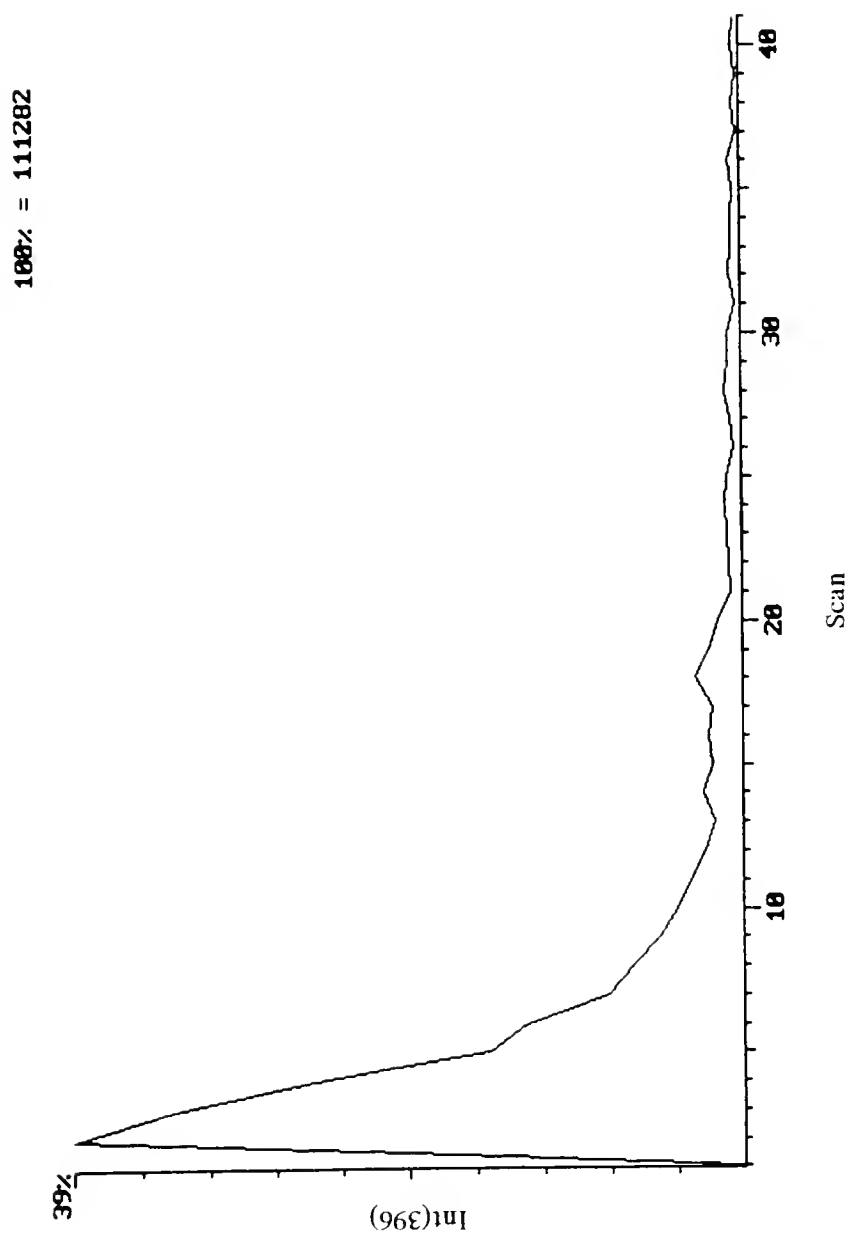


Figure 5-13. Ion intensity of protonated spiperone from MALDI/MS of spiperone in Matrigel membrane versus scan for external source configuration. 2  $\mu\text{L}$  of 0.5 mg/mL of spiperone in Matrigel sample mixed with 2  $\mu\text{L}$  of 520 mM DHB matrix solution.

configuration instrument. The spiperone signal for this experiment decays to approximately 10% of its highest intensity at scan #10. The improvement in signal lifetime (better overall sensitivity) with the external configuration, therefore, is similar for spiperone in Matrigel samples as observed for pure spiperone samples.

Due to the low ion signal of protonated spiperone from the Matrigel membrane, however, performing and optimizing MS/MS experiments on the  $m/z$  396 ion of spiperone in Matrigel was not possible. Improvement of the laser sampling method for the external method needs to be completed before MS/MS results can be achieved for the spiperone/Matrigel mixture as obtained for the pure spiperone and TMPA MS/MS experiments. This improvement includes increased laser beam transmission and focussing ability inside the external source, or complete removal of the current source to an open configuration similar to surface analysis methods.

MALDI/MS and MS/MS were also performed on leucine enkephalin and polyethylene glycols (average molecular weight from 600 u to 1500 u) with very good results in mass spectral quality and mass range extension. These results suggest the ability to perform MALDI and MS/MS using an external ion source has been fully achieved, and further studies should focus on the addition of laser microscopy.

### Conclusions

In conclusion, the preliminary experiments using the external laser desorption ionization source demonstrated promising results for further development of this method to add laser microscopy. LDI and MALDI were performed using the

external source with ion production and mass analysis similar to the internal configuration. It was observed that LDI of trimethylphenylammonium bromide provided very long lasting signals using the external source. The effect of low mass cutoff on the TMPA ion intensities was determined using these longer lasting signals. The results indicated a combination of trapping efficiency as well as fragmentation affecting the mass spectral results. Protonated spiperone signals were easily obtained from MALDI using the external source in much less time than required for optimization for the internal source. The combination of delayed laser triggering and addition of the arbitrary function generator provided the ability to perform MS/MS, as demonstrated for pure spiperone. The spiperone in Matrigel results demonstrated a need to improve the ion production of protonated spiperone with improvement to the laser transmission into the source region. Several suggestions for the implementation of an improved external laser desorption source, capable of performing microscopy, will be provided in the following chapter.

## CHAPTER 6 CONCLUSIONS

### Summary

In conclusion, the results obtained from laser desorption ionization on the quadrupole ion trap mass spectrometer have demonstrated highly selective analysis of solid samples. In order to improve the sensitivity of this method for the analysis of drug compounds in tissue, several studies were performed to better understand the trapping process for laser-desorbed ions. Trapping efficiency of laser-desorbed graphite ions was found to be dependent on the rf phase angle during the laser desorption event using the internal source configuration. Cyclical patterns were observed in the intensities of  $C_3^+$ ,  $C_4^+$ , and  $C_5^+$ . The low mass cutoff level was found to have similar effects on the intensities of  $^{56}Fe^+$ ,  $^{63}Cu^+$ , and  $^{65}Cu^+$  produced from LDI of probe tip surfaces. For equal  $q_z$  values, maximum ion intensities were detected for each of these ions that were twice as large as the ion intensities measure at a low mass cutoff level of 10 u. Also, minima observed in the ion intensity versus  $q_z$  value demonstrated the appearance of black holes in the ion trapping efficiency for ions formed at the ring electrode surface. Buffer gas pressure was determined to have the most significant effect on trapping efficiency.  $^{56}Fe^+$  intensity was found to increase rapidly from 0.005 mtorr to 5 mtorr of helium buffer gas. The copper

isotope ratio varied over the measured buffer gas range and deviated from the natural abundance ratio. For the rf phase angle results, the experimental data presented in this dissertation is the first data presented this phenomenon. The related results given by Doroshenko *et al.*<sup>18</sup> were not detailed enough to confirm the results given here and showed an effect of rf phase angle at only two points during the rf cycle. The rf amplitude and buffer gas pressure results were similar to other reported studies on the quadrupole ion trap. The rf amplitude data, however, much more detail for laser-desorbed ions produced at the ring electrode surface than previously reported.

These results suggest that to obtain the optimum trapping efficiency for lower molecular weight ions (<100 u) using the internal source configuration, the effects of rf phase angle and buffer gas pressure need to be considered for each sample. Even with the onset of space charge (which can subsequently be eliminated with selective ion ejection), the buffer gas pressure should be maintained at the highest possible operating pressure (e.g., before arcing or ion scattering) to trap the most ions using the internal source configuration. A low mass cutoff level should be used which takes into consideration not only optimum trapping efficiency, but also provides an informative mass range.

Laser desorption ionization and matrix-assisted laser desorption ionization were also demonstrated on the ion trap for analysis of several compounds. In particular, MALDI of the drug spiperone was developed to increase the production of the protonated molecule. The results from the MALDI development showed the



appearance of the molecular ion that was absent without the use of the UV-absorbing matrix. Laser irradiance was found to have the most significant effect for achieving good quality MALDI spectra with little fragmentation. MS/MS was performed on several compounds including protonated spiperone obtained from the MALDI method. The ability of the ion trap to perform tandem mass analysis provides a significant advantage in increased selectivity compared to the traditional single stages of time-of-flight mass spectrometry. MALDI also increased the duration of the ion signal overall in comparison to laser desorption ionization.

The MALDI mass spectra of spiperone and leucine enkephalin showed the sporadic appearance of adduct ions from addition reactions with alkali metal ions in the sample. For MALDI of spiperone in Matrigel mixtures, the protonated spiperone was detected, but adduct ions were seen in even greater abundance due to the higher concentration of sodium dissolved in the Matrigel membrane than in the pure spiperone samples. The MS/MS spectra of the Matrigel membrane samples showed chemical noise even after isolation of the ions of  $m/z$  396, presumably due to extraneous ions or neutrals desorbed off the probe tip surface into the ion trap volume for several milliseconds after the laser pulse. The occurrence of this chemical noise prompted the development of an external laser desorption configuration.

Preliminary experiments using the external laser desorption ionization source demonstrated an improvement in signal strength and lifetime compared to the internal configuration. Tandem mass spectrometry was performed on pure spiperone

samples, but the results for MS/MS of spiperone in Matrigel were poor due to the low ion abundances obtained for protonated spiperone. The methodology for interfacing the nitrogen laser with the external source system was determined and optimization of the method may improve the results for the Matrigel mixture. Suggestions for improvement of the external source method are given below.

### Suggestions for Future Studies

Future work should address increasing the sensitivity of the method by increasing analyte ion production from the sample as well as improving ion trapping efficiency. The external laser desorption source should be the focus of future developments to provide the many advantages this setup has over the internal configuration, as described in Chapter 5. For example, an external ion source will eliminate the presence of late-desorbing neutrals during the MS/MS process and permit optimum conditions for chemical ionization of laser-desorbed analyte neutrals. It will also allow the introduction of a sample stage and microfocussing apparatus for laser microscopy.

Methane CI of LD and MALD neutrals of spiperone should be evaluated for sensitivity and compared to laser ionization. The process of chemical ionization can first be optimized using conventional thermal desorption techniques and then applied to laser-desorbed neutrals. To increase the number of analyte ions produced by the LD/CI method, the laser can be pulsed two or more times during the ion production

step. The ion trap would consequently store the ions from each laser pulse and the collection from several pulses could increase overall sensitivity.

A pulsed rf trapping field could be used to increase the ion trapping efficiency. Ion injection can be performed with the rf field ramping from a low amplitude during initial introduction of the ions into the trap to a higher amplitude for the best storage conditions for these ions when located in the center of the trap. As shown by Eiden *et al.*, the period of rf ramping during injection would be microseconds (10-20  $\mu$ s) and only those ions transversing the trap during the voltage change would be trapped.<sup>59</sup>

Another method to improve ion trapping efficiency involves the use of a pulsed valve to temporarily introduce a buffer gas into the ion trap and increase the gas pressure from a millitorr to up to ten millitorr or greater. While buffer gas pressures higher than a millitorr typically decrease mass resolution and increase ion scattering losses, a temporary increase in pressure during trapping would enable the collisional cooling process to occur more rapidly and thus to trap more ions.

To perform laser microscopy, the use of an open source configuration is suggested with ion injection into the ion trap. The open source would consist of a sample stage, whether probe mounted or using probe deliverable samples, and a set of extraction lens situated within a centimeter of the sample surface. This method would allow greater access to the sample for introduction of the laser beam and viewing of the sample surface. Although the ion plume would now be exposed to the surrounding area, instead of an enclosed ion volume, the ion source area can be

physically separated from the ion trap analyzer region by a wall inside the vacuum chamber. The only disadvantage to this method is that it would not allow conventional chemical ionization to be performed since it would lack the enclosed volume for efficient pressurization with reagent gas, and more importantly lack a filament assembly. An advantage of maintaining the filament assembly on the source as used in the configuration presented in Chapter 5 is that it allows for mass calibration with the instrumental software. However, modified software in which ions of particular masses could be specified for calibration purposes would allow calibration to be performed using the laser desorption source. For example, the software could be adjusted to calibrate on the peaks obtained from MALDI of polyethylene glycol or cesium iodide clusters.

# APPENDIX A ELECTRONIC CIRCUIT CALIBRATION DATA FOR THE TRAPPING RADIOFREQUENCY PHASE ANGLE EXPERIMENT

The variable potentiometer calibration data (pot numbers) used for performing the rf phase angle experiment are given in Table A-1. These numbers were obtained by observing the temporal relation between the laser pulse to the rf drive potential on a digital storage oscilloscope, as described in Chapter 2.

Table A-1. Calibration data for rf phase  
synchronization experiment.

Pulse width	Pot number	rf phase angle
200	0.05	-11.4
250	0.49	7.8
300	0.90	27.0
350	1.32	46.3
400	1.74	65.5
450	2.19	84.7
500	2.60	103.9
550	3.01	123.1
600	3.39	142.4
650	3.79	161.6
700	4.11	180.8
750	4.43	200.0
800	4.71	219.2
850	4.96	238.5
900	5.22	257.7
950	5.45	276.9
1000	5.68	296.1

Table A-1. (Continued) Calibration data for rf phase synchronization experiment.

---

Pulse width	Pot number	rf phase angle
1050	5.89	315.3
1100	6.08	334.6
1150	6.26	353.8
1200	6.41	373.0
1250	6.55	392.2
1300	6.65	411.4
1350	6.81	430.6
1400	6.97	449.9
1450	7.09	469.1
1500	7.19	488.3
1550	7.28	507.5
1600	7.39	526.7

---

APPENDIX B  
FORTH KEY SEQUENCE PROGRAMS FOR COMPUTER ASSISTED  
RECORDING OF RADIOFREQUENCY PHASE ANGLE DATA AND  
RADIOFREQUENCY AMPLITUDE DATA

The first program, called PHASE.SCR, was used to collect data for the rf phase angle experiment. In this program, the computer waits several seconds while the rf circuit is being adjusted then acquire 10 scans and saves them on computer disk. This process is repeated for the number of data points being collected over a rf period.

Screen: 1

```
0 (
1
2
3
4   R IC-EXP-K                      \ run exp user program
5
6 [[                                \ go to forth
7   LOAD-SCAN-FUNCTION: LDMS-10    \ load scan function
8
9   1 INIT-DATAFILE RF126A          \ open data file as file #1
10
11
12
13
14 ]]
15
16
17
18
19
```

Screen: 2

```

0 (
1 (TURN ON NECESSARY ITEMS AND NORMALIZE SPECTRUM)
2 [[
3     MULTIPLIER-ON                \ turn on multiplier
4     RF-ON                        \ turn on rf
5     TICKLE-ON                    \ turn on tickle
6     TAKE-ONE-SCAN                \ take one scan
7     NORMALIZE-Y-AXIS             \ to normalize y-axis
8     TAKE-ONE-SCAN                \ take one scan
9     NORMALIZE-Y-AXIS             \ to normalize y-axis
10    TAKE-ONE-SCAN                \ take one scan
11    NORMALIZE-Y-AXIS             \ to normalize y-axis
12    ACQUIRE-MODE-ON             \ turn acquire mode on
13    1 SET-MICRO-ON                \ # microscans = 1
14
15 ]]
16
17
18
19

```

Screen: 3

```

0 (
1
2 [[
3
4     1 CHOOSE-FILE                \ choose file #1
5
6 ]]
7
8
9
10
11
12
13
14
15
16
17
18
19

```



Screen: 4

```

0 (
1
2 [[
3     29 0                                \ loop counter from 0 to 29
4 ]]                                       \ for each phase increment
5
6     <DO>                                \ start of loop
7
8 [[ NORMALIZE-Y-AXIS                    \ to normalize y-axis
9     10 SEC-WAIT                        \ wait 10 seconds
10     10 0 ]]                           \ loop counter from 0 to 10
11     <DO>                               \ for each data point
12 [[
13     1 SCAN-ACQUIRE                    \ take one scan
14 ]]
15     <LOOP>                             \ end of inner loop
16 <LOOP>                                \ end of outer loop
17
18
19

```

Screen: 5

```

0 (
1 [[
2
3 (CLOSE DATA FILE AND TURN ITEMS OFF, RETURN TO ITMS)
4
5     1 TINI-DATAFILE                    \ close data file and save
6     ACQUIRE-MODE-OFF                  \ turn acquire off
7     TICKLE-OFF                         \ turn tickle off
8     MULTIPLIER-OFF                     \ turn multiplier off
9     RF-OFF                             \ turn rf off
10 ]]
11     <ESC>
12
13
14
15
16
17
18
19

```

The second program, called RFLEVEL.SCR, was used to collect data for the rf amplitude experiment. The computer acquires a specified number of scans and then increments the start mass of several scan function tables. This process is repeated for the number of data points being collected over a rf amplitude range.

Screen: 1

```

0 (
1
2 R IC-EXP-K <CR> \ run ic-exp-k user program
3
4
5 [[ \ go to forth
6 LOAD-SCAN-FUNCTION: LDMS-50 \ load scan function
7
8 1 INIT-DATAFILE RF522A \ open data file as file #1
9
10
11 ]]
12
13
14
15
16
17
18
19
```

Screen: 2

```

0 (
1 (TURN ON NECESSARY ITEMS AND NORMALIZE SPECTRUM)
2 [[
3 MULTIPLIER-ON \ turn on multiplier
4 RF-ON \ turn on rf
5 TICKLE-ON \ turn on tickle
6 TAKE-ONE-SCAN \ take one scan
7 NORMALIZE-Y-AXIS \ to normalize y-axis
8 TAKE-ONE-SCAN \ take one scan
9 NORMALIZE-Y-AXIS \ to normalize y-axis
10 TAKE-ONE-SCAN \ take one scan
11 NORMALIZE-Y-AXIS \ to normalize y-axis
12 TAKE-ONE-SCAN \ take one scan
```

Screen: 2 (CONTINUED)

```

13  NORMALIZE-Y-AXIS          \ to normalize y-axis
14
15  ACQUIRE-MODE-ON          \ turn acquire mode on
16  ]]
17
18
19

```

Screen: 3

```

0  (
1  ( SET PARAMETERS FOR AN ACQUISITION )
2
3
4  [[
5      10 SET-MICRO-SCANS        \ set number of microscans
6      1 CHOOSE-FILE            \ choose file #1
7
8      DINTEGER R-MASS           \ define integer
9      400. D-> R-MASS          \ place value for starting mass
10
11  ]]
12
13
14
15
16
17
18
19

```

Screen: 4

```

0  (  RFLEVEL      LOOP PAGE )
1  (  VARY START MASS FROM 10 TO 65 IN INCREMENTS OF 1 )
2  [[  20 1      ]]          \ loop #1 from 1 to 20
3      <DO>                \ start of loop #1
4  [[      7 2      ]]          \ loop #2 from 1 to 7
5          <DO>                \ start of loop #2
6          <I>                \ place counter on stack
7  [[      SET-TABLE          \ choose table #
8
9          1 SET-PARAMETER    \ choose table parameter
10         R-MASS              \ copy integer to stack
11         SET-START-MASS     \ set start mass

```

Screen: 4 (CONTINUED)

```

12
13
14          <LOOP>                                \ end of loop #2
15 [[ 1 SCAN-ACQUIRE                             \ scan 1 time
16    200. D+> R-MASS ]]                          \ increment variable by 0.5 u
17    <LOOP>                                       \ end of loop #1
18
19

```

Screen: 5

```

0 (
1
2 [[
3 ( CLOSE DATA FILE AND TURN ITEMS OFF, RETURN TO ITMS)
4
5    1 TINI-DATAFILE                             \ close data file and save
6    ACQUIRE-MODE-OFF                          \ turn acquire off
7    TICKLE-OFF                                 \ turn tickle off
8    MULTIPLIER-OFF                            \ turn multiplier off
9    RF-OFF                                     \ turn rf off
10 ]]
11    <ESC>
12
13
14
15
16
17
18
19

```

## REFERENCES

1. Perchalski, R.J.; Yost, R.A.; Wilder, B.J. *Anal. Chem.* **1983**, *55*, 2002-2005.
2. Perchalski, R.J. Ph.D. thesis. "Characteristics and Application of a Laser Ionization/Evaporation Source for Tandem Mass Spectrometry," University of Florida, **1985**.
3. Johnson, J.V.; Yost, R.A.; Kelley, P.E.; Bradford, D.C. *Anal. Chem.* **1990**, *62*, 2162-2172.
4. March, R.E. *Int. J. Mass Spec. Ion Processes.* **1992**, *118/119*, 71-135.
5. Schey, K.; Cooks, R.G.; Grix, R.; Wöllnik, H. *Int. J. Mass Spec. Ion Processes.* **1987**, *77*, 49-61.
6. Cornish, T.J.; Cotter, R.J. *Anal. Chem.* **1993**, *65*, 1043-1047.
7. Kelland, D.; Wallach, E.R.; Cottee, F.H.; Williamson, F.A. *Anal. Chim. Acta.* **1987**, *195*, 89-96.
8. Cotter, R.J. *Anal. Chem.* **1984**, *56*, 485A-504A.
9. Vandeputte, D.; Van Grieken, R.E.; Jacob, W.A.; Savory, J.; Bertholf, R.L.; Wills, M.R. *Biomed. and Env. Mass Spec.* **1989**, *18*, 598-602.
10. McCrery, D.A.; Gross, M.L. *Anal. Chim. Acta.* **1985**, *178*, 91-103.
11. Buchanan, M.V.; Hettich, R.L. *Anal. Chem.* **1993**, *65*, 245A-259A.
12. Yost, R.A.; McClennen, W.; Snyder, P.A. *Proceedings from the 35th ASMS Conference on Mass Spectrometry and Allied Topics*, Denver, CO, May 24-29, **1987**, p. 789-790.
13. Van Berkel, G.J.; Glish, G.L.; McLuckey, S.A. *Anal. Chem.* **1990**, *62*, 1284-1295.
14. Kaiser, R.E.; Cooks, R.G.; Moss, J.; Hemberger, P.H. *Rap. Comm. Mass Spec.* **1989**, *3*, 50-53.

15. Kaiser, R.E.; Louris, J.N.; Amy, J.W.; Cooks, R.G. *Rap. Comm. Mass Spec.* **1989**, *3*, 225-229.
16. Schwartz, J.C.; Syka, J.E.P.; Jardine, I. *J. Am. Soc. Mass Spectrom.* **1991**, *2*, 198-204.
17. Goeringer, D.E.; Whitten, W.B.; Ramsey, J.M.; McLuckey, S.A.; Glish, G.L. *Anal. Chem.* **1992**, *64*, 1434-1439.
18. Doroshenko, V.M.; Cornish, T.J.; Cotter, R.J. *Rap. Comm. Mass Spec.* **1992**, *6*, 753-757.
19. Schwartz, J.C.; Bier, M.E. *Rap. Comm. Mass Spec.* **1993**, *7*, 27-32.
20. Todd, J.F.J.; Penman, A.D. *Int. J. Mass Spec. Ion Processes.* **1991**, *106*, 1-20.
21. Stafford, G.C.; Kelley, P.E.; Syka, J.E.P.; Reynolds, W.E.; Todd, J.F.J. *Int. J. Mass Spec. Ion Processes.* **1984**, *60*, 85-98.
22. Johnson, J.V.; Pedder, R.E.; Yost, R.A. *Int. J. Mass Spec. Ion Processes.* **1991**, *106*, 197-212.
23. Eckenrode, B.A.; Glish, G.L.; McLuckey, S.A. *Int. J. Mass Spec. Ion Processes.* **1990**, *99*, 151-167.
24. Hogan, J.D.; Beu, S.C.; Laude, Jr., D.A.; Majidi, V. *Anal. Chem.* **1991**, *63*, 1452-1457.
25. Louris, J.N.; Brodbelt, J.S.; Cooks, R.G. *Int. J. Mass Spec. Ion Processes.* **1987**, *75*, 345-352.
26. Wilk, Z.A.; Viswanadhan, S.K.; Sharkey, A.G.; Hercules, D.M. *Anal. Chem.* **1988**, *60*, 2338-2346.
27. van der Hart, W.J. *Mass Spec. Rev.* **1989**, *8*, 237-268.
28. Amster, I.J.; Land, D.P.; Hemminger, J.C.; McIver, Jr., R.T. *Anal. Chem.* **1989**, *61*, 184-186.
29. Cotter, R.J.; Tabet, J.-C. *Int. J. Mass Spec. Ion Processes.* **1983**, *53*, 151-166.
30. Hillenkamp, F.; Karas, M.; Beavis, R.C.; Chait, B.T. *Anal. Chem.* **1991**, *63*, 1193A-1203A.
31. Van der Peyl, G.J.Q.; Van der Zande, W.J.; Bederski, K.; Boerboom, A.J.H.; Kistemaker, P.G. *Int. J. Mass Spec. Ion Processes.* **1983**, *47*, 7-10.

32. Karas, M.; Bachmann, D.; Bahr, U.; Hillenkamp, F. *Int. J. Mass Spec. Ion Processes*. **1987**, 78, 53-68.
33. Karas, M.; Hillenkamp, F. *Proceedings of the 37th ASMS Conference on Mass Spectrometry and Allied Topics*, Miami Beach, FL, May 21-26, **1989**, p. 1168-1169.
34. Pan, Y.; Cotter, R.J. *Org. Mass Spec.* **1992**, 27, 3-8.
35. Beavis, R.C.; Chait, B.T. *Chem. Phys. Let.* **1991**, 181, 479-484.
36. Sundqvist, B.U.R. *Int. J. Mass Spec. Ion Processes*. **1992**, 118/119, 265-287.
37. Todd, P.J.; Short, R.T.; Grimm, C.C.; Holland, W.M.; Markey, S.P. *Anal. Chem.* **1992**, 64, 1871-1878.
38. Heller, D.N.; Lys, I.; Cotter, R.J.; Uy, O.M. *Anal. Chem.* **1989**, 61, 1083-1086.
39. Glish, G.L.; Goeringer, D.E.; Asano, K.G.; McLuckey, S.A. *Int. J. Mass Spec. Ion Processes*. **1989**, 94, 15-24.
40. Goeringer, D.E.; Glish, G.L.; McLuckey, S.A. *Anal. Chem.* **1991**, 63, 1186-1192.
41. Gill, C.G.; Blades, M.W. *J. Atom. Spec.* In press.
42. Basic, C. Ph.D. thesis. "Probing Trapped Ion Energies in a Quadrupole Ion Trap Mass Spectrometer," University of Florida, **1992**.
43. March, R.E.; Hughes, R.J. *Quadrupole Storage Mass Spectrometry*. Vol. 102 of *Chemical Analysis*, J.D. Winefordner (Ed.), Wiley-Interscience Publication, New York, **1989**.
44. March, R.E.; Londry, F.A.; Alfred, R.L. *Org. Mass Spectrom.* **1992**, 27, 1151-1152.
45. Louris, J.N.; Amy, J.W.; Ridley, T.Y.; Cooks, R.G. *Int. J. Mass Spec. Ion Processes*. **1989**, 88, 97-111.
46. Pedder, R.E.; Yost, R.A.; Weber-Grabau, M. *Proceedings of the 37th ASMS Conference on Mass Spectrometry and Allied Topics*, Miami Beach, FL, May 21-26, **1989**, p. 468-469.
47. Kishore, M.N.; Ghosh, P.K. *Int. J. Mass Spec. Ion Phys.* **1979**, 29, 345-350.

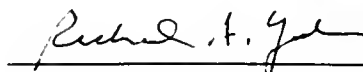
48. Ghosh, P.K.; Arora, A.S.; Narayan, L. *Int. J. Mass Spec. Ion Phys.* **1977**, *23*, 237-240.
49. O, C.-S.; Schuessler, H.A. *J. Appl. Phys.* **1981**, *52*, 1157-1166.
50. Pedder, R.E.; Johnson, J.V.; Yost, R.A. *Proceedings of the 40th ASMS Conference on Mass Spectrometry and Allied Topics*, Washington, DC, May 31-June 5, **1992**, p. 1761-1762.
51. Wang, Y.; Franzen, J. *Int. J. Mass Spec. Ion Processes.* **1992**, *112*, 167-178.
52. Wang, Y.; Franzen, J.; Wanczek, K.P. *Int. J. Mass Spec. Ion Processes.* **1993**, *124*, 125-144.
53. Guidugli, F.; Traldi, P. *Rap. Comm. Mass Spec.* **1991**, *5*, 343-348.
54. Morand, K.L.; Lammert, S.A.; Cooks, R.G. *Rap. Comm. Mass Spec.* **1991**, *5*, 491.
55. Eades, D.M.; Yost, R.A. *Rap. Comm. Mass Spec.* **1992**, *6*, 573-578.
56. Pedder, R.E.; Johnson, J.V.; Yost, R.A. *Proceedings of the 41st ASMS Conference on Mass Spectrometry and Allied Topics*, San Francisco, CA, May 30-June 4, **1993**.
57. Chambers, D.M.; Goeringer, D.E.; McLuckey, S.A.; Glish, G.L. *Anal. Chem.* **1993**, *65*, 14-20.
58. Berberich, D.W. Ph.D. thesis. "Fundamental Studies of Chemical Ionization and Charge Exchange Ionization for Quadrupole Ion Trap Mass Spectrometry," University of Florida, **1989**.
59. Eiden, G.C.; Cisper, M.E.; Alexander, M.L.; Hemberger, P.H.; Nogar, N.S. *J. Am. Soc. Mass Spectrom.* **1993**, *4*, 706-709.



## BIOGRAPHICAL SKETCH

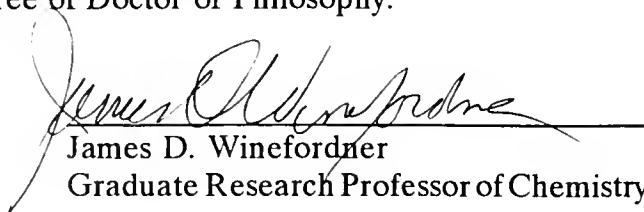
Rafael Roberto Vargas was born in Miami Beach, Florida on May 24, 1966. Raised in Miami, he is the son of Rafael A. Vargas, who is originally from San Jose, Costa Rica, and Coral Siberon, who is originally from Ponce, Puerto Rico. After graduating from Southwest Miami Senior High School in 1984, Rafael attended the University of Miami on the Henry King Stanford Scholarship and the Florida Honors Scholarship. He performed undergraduate research in electrochemistry under the direction of Dr. Angel Kaifer while majoring in chemistry and minoring in biology. In 1988, he earned a Bachelor of Science degree and graduated from the honors program. At the University of Florida, Rafael learned the eclectic nature of the analytical chemist from his distinguished research supervisor, Professor Richard A. Yost. While in Gainesville, he also participated in the University of Florida's Horse Teaching Program as a volunteer groom to learn equitation. After graduation, Rafael plans to take a postdoctoral position.

I certify that I have read this study and that in my opinion it conforms to acceptable standards of scholarly presentation and is fully adequate, in scope and quality, as a dissertation for the degree of Doctor of Philosophy.



Richard A. Yost, Chair  
Professor of Chemistry

I certify that I have read this study and that in my opinion it conforms to acceptable standards of scholarly presentation and is fully adequate, in scope and quality, as a dissertation for the degree of Doctor of Philosophy.



James D. Winefordner  
Graduate Research Professor of Chemistry

I certify that I have read this study and that in my opinion it conforms to acceptable standards of scholarly presentation and is fully adequate, in scope and quality, as a dissertation for the degree of Doctor of Philosophy.



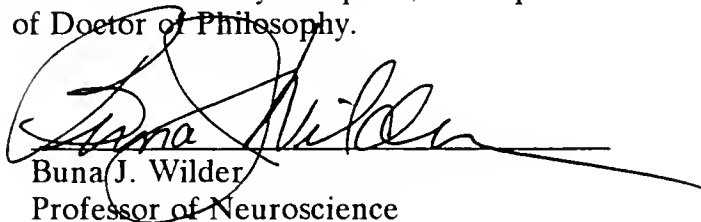
Vaneica Y. Young  
Associate Professor of Chemistry

I certify that I have read this study and that in my opinion it conforms to acceptable standards of scholarly presentation and is fully adequate, in scope and quality, as a dissertation for the degree of Doctor of Philosophy.



John R. Eyler  
Professor of Chemistry

I certify that I have read this study and that in my opinion it conforms to acceptable standards of scholarly presentation and is fully adequate, in scope and quality, as a dissertation for the degree of Doctor of Philosophy.



Buna J. Wilder  
Professor of Neuroscience

This dissertation was submitted to the Graduate Faculty of the Department of Chemistry in the College of Liberal Arts and Sciences and to the Graduate School and was accepted as partial fulfillment of the requirements for the degree of Doctor of Philosophy.

December 1993

---

Dean, Graduate School

UNIVERSITY OF FLORIDA



3 1262 08557 0876